Gas-Surface Interaction Models in Hypersonic Flows

Carlos Manuel da Cunha Teixeira

Thesis to obtain the Master of Science Degree in

Aerospace Engineering

Supervisors: Prof. Mário António Prazeres Lino da Silva
Dr. Bruno Eduardo Lopez

Examination Committee

Chairperson: Prof. Filipe Szolnoky Ramos Pinto Cunha
Supervisor: Dr. Bruno Eduardo Lopez
Member of the Committee: Prof. Vasco António Dinis Leitão Guerra

December 2015

Acknowledgments

Firstly I recommend to the novice two great books to serve as foundations to the field. Anderson [1] has a very good, down-to-earth pedagogical approach that stimulates the student. Vicenti and Kruger [2] prime for their succinct and yet highly detailed explanations.

I thank IPFN for having welcomed me in the past months and presenting me with unique and interesting opportunities. I thank Prof. Mário Lino for having introduced me to this fascinating field of high-temperature gas-dynamics, for his enthusiasm towards the subject and for his flexibility and support as supervisor. I thank him further for the financial support provided.

I congratulate Dr. Bruno Lopez for his elaborate work on SPARK. I acknowledge the imposing task of being the sole developer of the code. I thank him for his devote tutoring and insightful inputs.

I thank my colleagues João Vargas, Daniel and Carolina for the enjoyable breaks from work. They helped me relax from the strains of the thesis and face my tasks with renewed energy.

Lastly I thank my parents for the support in all forms on this past years, and always keeping sure I had everything I needed, and my sister for her interest in my achievements.

Resumo

Esta tese consiste na introdução do fenómeno de catalicidade no SPARK.

O SPARK é um código de aerotermodinâmica que resolve numericamente as equações de Navier-Stokes reactivas. Ele é usado para simular o escoamento de reentrada atmosférica de naves espaciais. O SPARK foi desenvolvido e é mantido pelo IPFN.

Até então o SPARK negligenciava reacções heterogéneas (reacções fluido/parede) através das quais 2 átomos, mediados pela superfície, recombinam, libertando energia para o veículo, apesar desta função estar disponível em grande parte de códigos semelhantes. A catalicidade tem um efeito na composição química do escoamento, e um forte impacto no fluxo de calor para a nave. Foi introduzido um modelo de catalicidade que modela o fenómeno de forma macroscópica. Neste modelo a recombinação na parede de espécies químicas dissociadas é caracterizado por um único parâmetro que é constante ou que dependente da temperatura (da parede). Para tal foi necessário modificar as equações de balanço de massa e energia na fronteira entre o escoamento e a parede. Os resultados de várias simulações foram comparados com outros códigos numéricos e dados experimentais.

Para além disso, iniciou-se a implementação de um modelo mais avançado, denominado FRSC, que permite prever fenómenos de ablação e pirólise. Foi elaborada a formulação inicial que descreve com grande detalhe reacções químicas heterogéneas no caso de não haver escoamento. Esta formulação serve de base para a implementação final num escoamento governado pelas equações de Navier-Stokes reactivas.

Palavras-chave: TPS, catalicidade, SPARK, escoamento hipersónico, aerotermodinâmica

Abstract

This thesis consists on the implementation of catalycity in SPARK.

SPARK is an aerothermodynamics code that solves the reacting Navier-Stokes equations. It is used to simulate re-entry flows of space vehicles. SPARK is developed and maintained at IPFN.

Until then SPARK neglected heterogeneous reactions (fluid/solid interaction) through which 2 atoms, mediated by the surface, recombine, releasing energy into the vehicle. However, this capability is standard in similar codes. Catalyticy has an effect on the composition of the flow and plays a pivotal role on the heat flux into the space-ship. A model that describes catalycity macroscopically has been introduced. In this model the recombination at the wall of two dissociated species is characterized by a single parameter that can be either constant of temperature dependent. That required a suitable improvement of the mass and energy balance equations between the fluid flow and the wall. The results from various simulations were compared with other numerical codes and experimental data.

Furthermore, the first stage of the implementation of a more advanced model, termed FRSC, that takes into account ablation and pyrolysis phenomenon has been achieved. This initial formulation describes microscopically, and in great detail, the heterogeneous chemical reactions on the particular case of no gas flow; and serves as the foundation for the final implementation of the FRSC on a flow governed by the full reacting Navier-Stokes equations.

Keywords: TPS, catalycity, SPARK, hypersonic flow, aerothermodynamics

Contents

List of Tables

List of Figures

.

Nomenclature

Greek symbols

$[\tau]$	Viscous stress tensor, N m^{-2}
χ_i	Mole fraction of species i on a bulk environment.
ϵ	Emissivity of the surface.
γ	Catalytic recombination coefficient, also known as reaction efficiency. When accompanied with an index γ_i is concerns a particular catalytic reaction for which species i is the reactant, dimensionless
ν	Fundamental vibrational frequency of a molecule.
ν_{gr}	Stoichiometric coefficient that runs only over gas species: $\sum_i \left(\nu_{ir}^{''} - \nu_{ir}^{'}\right)$
$\nu_{ir}^{'}$, $\nu_{ir}^{''}$	Stoichiometric coefficients of species i on reactant and product sides of a chemical equation r, respectively.
Φ_s	Active site density, mol m^{-2}.
$\Phi_{ns,i}$	Concentration of gas species i on surface phase ns. The index ns may be omitted if only one surface phase exists, mol m^{-2}.
ρ	Density, kg m^{-3}.
σ	Stefan-Boltzmann constant.

Roman symbols

c_i	Mass fraction of species i.
$c_{i,\mathrm{w}}$	Mass fraction of species i at the wall.
C_i	Concentration of species i, i.e., number of moles of species i per unit volume of mixture, mol m^{-3}.
R_i	Specific gas constant of species i, J kg^{-1} K^{-1}.
R_u	Universal gas constant, J mol^{-1} K^{-1}.
R	Specific gas constant of a mixture, J kg^{-1} K^{-1}.

X_i	Generalized concentration of species i. Has a different symbol and units if it concerns a gas, surface of bulk species.
Δn	Distance from the internal cell to the wall.
$\dot{\omega}_{ir}$	Production rate of species i due to reaction r. Due to convenience the units are $\mathrm{kg\,m^{-2}\,s^{-1}}$ for the SRE model and $\mathrm{mol\,m^{-2}\,s^{-1}}$ for the FRSC model.
$\dot{\omega}_i$	Production rate of species i due to all reactions. Due to convenience the units are $\mathrm{kg\,m^{-2}\,s^{-1}}$ for the SRE model and $\mathrm{mol\,m^{-2}\,s^{-1}}$ for the FRSC model.
$\vec{u}$	Mean flow velocity, $\mathrm{m\,s^{-1}}$
C_p	Specific heat at constant pressure, $\mathrm{J\,kg^{-1}\,K^{-1}}$
C_v	Specific heat at constant volume, $\mathrm{J\,kg^{-1}\,K^{-1}}$
D	Diffusion coefficient, $\mathrm{m^2\,s^{-1}}$.
E	Total energy, J
G_i^0	Gibbs energy of species i, $\mathrm{J\,mol^{-1}}$.
h	Specific enthalpy $\mathrm{kJ\,kg^{-1}}$ or Plack's constant
H_i^0	Enthalpy of species i, $\mathrm{J\,mol^{-1}}$.
k	Thermal conductivity, $\mathrm{J\,s^{-1}\,m^{-1}\,K^{-1}}$
k_{fr}, k_{br}	Forward and backward reaction rates for reaction r, units vary.
$M^{\downarrow}$	Impinging mass flux, $\mathrm{kg\,m^{-2}\,s^{-1}}$.
N_s	Number of species.
p	Pressure, Pa.
S_i^0	Entropy of species i, $\mathrm{J\,mol^{-1}\,K^{-1}}$.
T	Temperature, K

Subscripts

∞	Free-stream value.
g	Gas species.
i	Species index. When in a different font i represents an internal cell, namely the first internal cell after the ghost cells.
j	Species index, although the most common subscript for the species index is i.
r	Index of a reaction.

s	Surface species
g	Evaluated at the ghost cell. On the FRSC model it may also mean gas species.
ref	Reference condition.
w	Evaluated at the wall.

Glossary

CFD	Computational Fluid Dynamics is a branch of fluid mechanics that uses numerical methods and algorithms to solve problems that involve fluid flows.
DPLR	Data Parallel Line Relaxation is a CFD code employed by NASA Ames Research Center for re-entry flow calculations. It is a structured, finite volume code that solves the reacting Navier-Stokes equations.
ER	The Eley-Rideal mechanism describes the surface reaction between a reactant molecule from a gas phase and one that is absorbed on the surface.
FRSC	Finite Rate Surface Chemistry is a state-of-art formulation to deal with catalycity. In contrast with the SRE method, it takes into account the microscopic processes through which surface reactions occur.
IPFN	Instituto de Plasmas e Fusão Nuclear is a research unit of Instituto Superior Técnico from the University of Lisbon.
LAURA	Langley Aerothermodynamic Upwind Relaxation Algorithm is a structured, finite volume CFD code that solves the reacting Navier-Stokes equations.
LH	The Langmuir–Hinshelwood mechanism describes the surface reaction between two adsorbed species that undergo a bimolecular reaction.

LeMANS	(Le) Michigan Aerothermodynamics Navier-Stokes is a CFD code developed at the University of Michigan. It is an unstructured, finite volume code that solves the reacting Navier-Stokes equations.
NV	Navier-Stokes, as in Navier-Stokes equations, is a set of equations that governs fluid flow.
ODE	Ordinary Differential Equation.
SEB	The Surface Energy Balance constitutes a boundary condition that assumes that the wall is in radiative equilibrium. There is no conduction loss through the wall, and the incoming energy is balanced by the emissivity of the wall.
SPARK	Software Package for Aerothermodynamics, Radiation and Kinetics is a multiphysics code developed and maintained at IPFN. It is structured, finite-volume code that solves the reacting Navier-Stokes equations.
SRE	Specified Reaction Efficiency is formulation used by CFD codes to deal with catalycity in which a surface efficiency, or surface recombination coefficient, often denoted γ, is specified as a constant or as a function of temperature. The value determines the ratio of consumption of a given atomic species that impinges on the wall.
TPS	A Thermal Protection System is a barrier to protect a space vehicle from the intense heat flux experienced during atmospheric re-entry.
V&V	Verification and Validation is a set of processes to assess the credibility and reliability of computer simulations.

Chapter 1

Introduction

1.1 Topic Overview

Space vehicles enter a planetary (Earth or other planet) atmosphere at near orbital (V_∞ = 7.9 $\frac{\text{km}}{\text{s}}$ for Earth) and super-orbital speeds, relative to the atmosphere [3]. In this hypersonic flow regime a strong shock-wave is formed upstream of the spacecraft, wherein the flow slows down to subsonic speeds. The total energy associated with such high velocities ($\approx \frac{1}{2}mV^2$) is partially converted into internal energy of the gas giving rise to various physical processes like dissociation, ionization occurring between the shock and the vehicle. As a first approximation if we assume that all this energy is absorbed by the vehicle [4], few materials could withstand this level without disintegrating:

$$Q = \frac{1}{2}mV^2 \Leftrightarrow \frac{Q}{m} = \frac{V^2}{2}$$
$$\text{Earth re-entry } V_\infty \approx 7.9\,\frac{\text{km}}{\text{s}} : \frac{Q}{m} = 31\,401\,\frac{\text{kJ}}{\text{kg}} \tag{1.1}$$

Where Q is the total (kinetic) energy, m is the mass of the spaceship and V its velocity. Table 1.1 shows that only parts made of graphite would resist and that there is 3.5 × the energy needed to vaporize Titanium.

Material	Energy to Vaporize [kJ/kg]	Melting Temperature [K]
Tungsten	4350	3611
Titanium	8990	2056
Beryllium Oxide	31168	1611
Graphite	66756	3778

Table 1.1: Energy necessary to vaporize some typical materials, adapted from [4]

Moreover, if we make a quick estimate for the stagnation temperature on the nose of the vehicle [4] with the help of the steady one-dimensional heat equation [5, pp. 51-52]:

$$h_\infty + \frac{V_\infty^2}{2} = h_0 + \underbrace{\frac{V_0^2}{2}}_{=0(\text{Stagnation})} \Leftrightarrow$$

$$C_p T_\infty + \frac{V_\infty^2}{2} = C_p T_o \Leftrightarrow$$

$$\text{Using the approximation } T_0 \gg T_\infty : T_0 = \frac{V_\infty^2}{2C_p}$$

$$\text{Earth re-entry } V_\infty \approx 7.9 \, \frac{\text{km}}{\text{s}} : T_0 = 31\,245\,\text{K}$$

Where h is the enthalpy, C_p is the specific heat constant taken to be $1.005 \, \frac{\text{kJ}}{\text{kg K}}$, T is the temperature, and the subscripts $_0$ and $_\infty$ refer to stagnation and free-stream respectively.

Again, from table 1.1, this temperature value is more than most materials can endure. Admittedly this is a crude analysis, and not all the energy is absorbed by the vehicle. However these concise calculations help evidencing why heat loading is both a key parameter and a challenge for the design of entry spacecraft. Effectively, the surface of such vehicles must be equipped with a Thermal Protection System (TPS) designed to sustain heat loads of this magnitude withtout endangering the underlying structure [6]. Depending heating on the heating levels, there are two TPS classes that can be employed: Reusable TPS and ablative TPS [7]. The corresponding range of applicability is illustrated on figure 1.1.

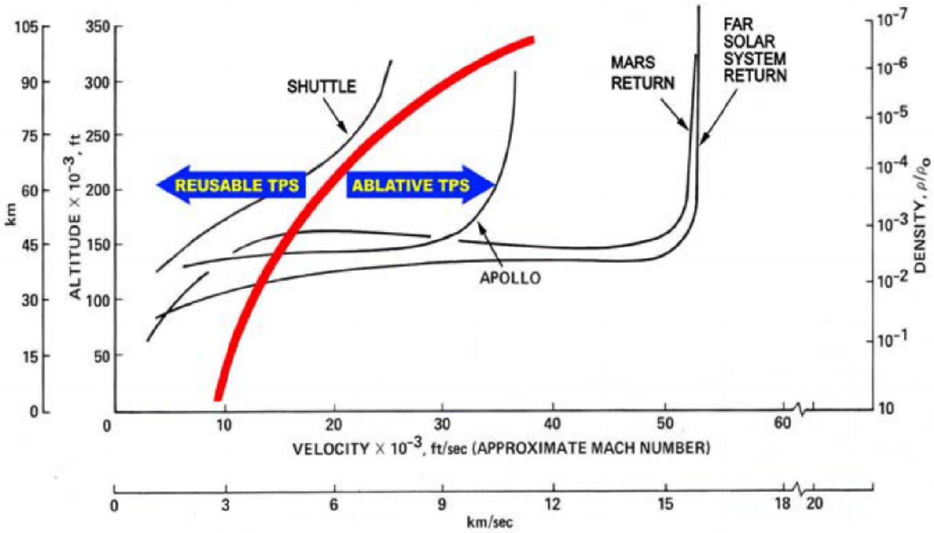

Figure 1.1: Suitability of reusable and ablative TPS for different mission types, reproduced from [8]. Concerns flight regimes in the particular case of Earth's atmosphere.

- **Reusable TPS**

  Reusable TPS are characterized by not promoting property changes or mass loss of the TPS materials. In other words, they retain structural integrity and their physical properties up to a critical point. Catalytic reactions occur at the surface but do not involve the surface materials. Such reactions consist on the recombination of the incoming dissociated environment gas. As recombination increases the heat carried to the vehicle, it is desirable to have a surface with low catalycity . Also,

the surface may irradiate some energy, as a function of its black-body temperature, and therefore net radiation is an important mechanism of heat transfer. The surface coating should have a high emissivity to carry as much heat away as possible [7].
The Space Shuttle program was the responsible for a great emphasis on reusable TPS research (at the cost of ceasing ablative TPS) [8], and hence is the source of much of the experimental data and theoretical models known [9, 10].
A disadvantage of reusable TPS is that they are systems limited for operation in relatively mild aerothermal re-entry conditions.

- **Ablative TPS**
  Ablative TPS can handle higher heating rates by allowing material property changes and also sacrificing TPS material/mass. There are two ways through which this mass loss occurs:

  - **Pyrolyzing/charring ablating TPS**
    Pyrolysis is the decomposition of the internal solid material and occurs when the material is exposed to high temperatures. It produces gaseous products that end up being injected in the boundary-layer due to the gas pressure inside the pyrolysis zone [6]. As the pyrolysis gases ascend to the boundary layer, they absorb some of the energy from the solid material. On the surface itself, a char layer is formed that recedes due to chemical or mechanical action.
    These TPS are composites of polymer resins with some other reinforcement material (generally carbon, glass or organic polymers) [11].

  - **Non-pyrolyzing/non-charring ablating TPS**
    In contrast, non-charring materials don't undergo in-depth decomposition. Instead, the exposed surface chemically reacts with the gas environment resulting in sublimation and vaporization (endothermic) and oxidation and nitration (exothermic). The corresponding reaction products are diffused into the boundary-layer promoting its cooling and reducing the heat flux into the wall. This phenomenon is referred as ”blowing”. Such mechanisms yield a specific surface consumption rate and have a great impact on the net energy to the surface [7].
    In contrast with charring ablative TPS, noncharring ablative TPS are usually made of carbon or silica. They are denser and structurally stronger than charring ablators, and can also withstand higher shearing stresses [12].

Furthermore, and as can be seen on figure 1.2, radiation is also a relevant energy transfer mechanism for ablative TPS. Again it is desirable to have a high emittance surface to promote re-radiation [13], specially when the temperatures are higher.
In short, ablative TPS burn away in a controlled manner so as to dissipative heat. The physical and chemical processes involved are, when compared with reusable TPS, more varied and much more complex.

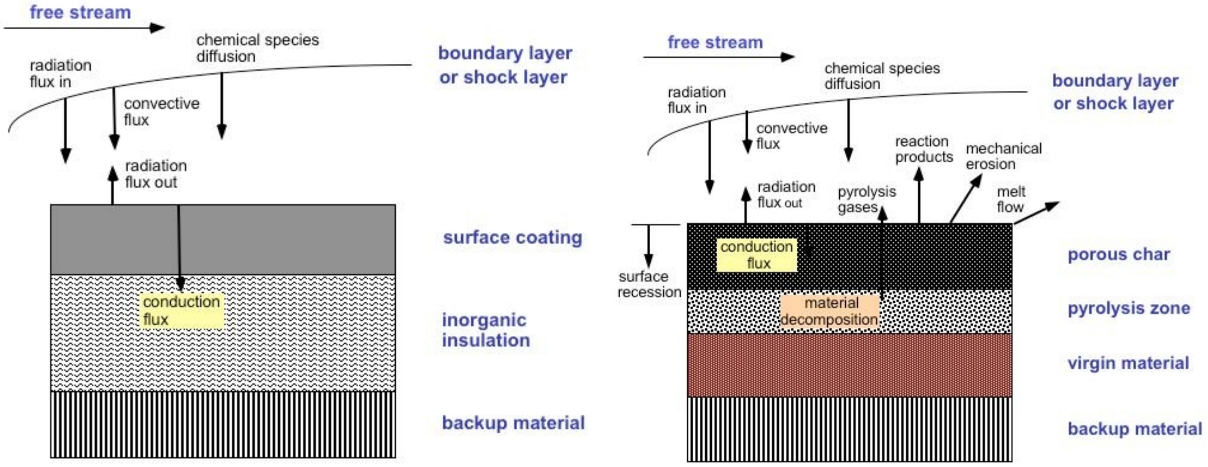

(a) Reusable TPS (b) Ablative - charring and non-charring - TPS

Figure 1.2: Energy accommodation of TPS materials [7].

1.2 Ground Testing and CFD Modeling for re-entry problems

Because experimental data is very rare, owing to prohibitive costs of on-board experiments (atmospheric re-entry), this field depends greatly on ground testing and CFD. Ground tests are widely used but present certain limitations in simulating turbulent flow, high shear, high pressure gradients and combined convective and radiative heating [8]. The types of existing ground testing facilities are arc jets, inductively coupled plasma facilities, energy laser facilities, shock tubes and arc heaters. The first two are the most common [11]. However, none of these single facilities is able to replicate all actual re-entry flight conditions simultaneously, which is why ground testing is usually delegated to development and selection of TPS materials and validation of the CFD simulations on a segmented way [14]. That is, each facility is used for validation within the specific test conditions it is able to reproduce.

Aero-thermodynamics is a multidisciplinary topic. CFD in non-equilibrium flow is thus particularly complex. There have been many improvements on the past decades, namely in the numerical solvers and the non-equilibrium thermodynamic models. Despite this, the improvements that directly concern TPS design have been, until recently, overlooked. In fact, most codes model surface conditions with a constant temperature or a constant heat flux, and neglect mass transfer altogether. This is incompatible with the complex chemical and physical interactions between the surface and the gas occurring on ablative TPS. Even on reusable TPS, a fixed temperature or constant heat flux along the entire surface is too simplistic.

More recently, a few codes have implemented the modelling of fluid/surface interaction, i.e., the appropriate coupling of the homogeneous flow with the vehicle's surface behaviour. The most known and complete are LeMANS from the University of Michigan [15], DPLR from the NASA Ames research center [16, 17] and the 2008 LAURA update from NASA Langley [18]. They represent the current state-of-the-art, specially in TPS modelling, and are capable of dealing with non-charring ablation as well as charring ablation.

Most of the remaining codes can just be expected to model reusable TPS. Because the heating rates are not high, the CFD implementation just needs to take into account certain catalytic reactions at the surface, namely recombination reactions, and not the surface participating reactions like sublimation, characteristic of ablation. For air environments, normally the recombination of O and N is modelled:

$$\begin{aligned} \mathrm{N} + \mathrm{N} &\longrightarrow \mathrm{N_2} \\ \mathrm{O} + \mathrm{O} &\longrightarrow \mathrm{O_2} \\ \mathrm{N} + \mathrm{O} &\longrightarrow \mathrm{NO} \end{aligned} \tag{1.2}$$

These reactions need to be taken into account on both the energy and mass balance boundary conditions. To model recombination effects, it is customary to define a parameter γ that macroscopically expresses the ratio between the number of incoming atoms from the dissociated gas, and the number of those atoms that recombine through 1.2. The more recombination exists, the higher the heat transfer to the vehicle as determined by the energy balance equation. Often some CFD codes just assume a worst case scenario that results in the highest possible heat transfer, in order to avoid the modelling just described. On the other hand, more sophisticated codes discard this macroscopic approach and take into account the microscopic pathways through which these reactions occur.

Obviously there is a certain division on the capabilities of the various CFD programs that follow the demands of each TPS classes previously discussed. In other words, certain codes can just model reusable TPS while others can fully model ablative TPS [19].

1.3 Objectives

This works aims at improving the capabilities of the SPARK code.

SPARK - **S**oftware **P**ackage for **A**erothermodynamics, **R**adiation and **K**inetics - is a multiphysics code capable of hypersonic re-entry simulations. It has been developed and is maintained at IPFN - Instituto Superior Técnico, by Bruno Lopez. SPARK is a 2-dimensional, structured, finite-volume, reactive Navier-Stokes equations solver, that takes into account finite-rate chemistry and vibrational non-equilibrium effects. It is written in Fortran 03/08 language via oriented object programming.

Before the present work, SPARK was unable to deal with the most basic form of catalycity. The first objective consisted in implementing in SPARK a versatile capability of catalycity that was at the level of reusable TPS. Versatility means a code that adapts, without further changes, to different simulations; that is, a code that is not hard-coded.

The general approach followed is not much different from the one many other codes have implemented in the past. This is because the model (in the analytical sense) that describes reusable TPS is fairly straightforward and is more or less closed to any improvements. The differences are therefore on the numerical implementation itself that depend to a large extent on computational scheme each code uses to discretize and solve the Navier-Stokes equations. Furthermore, for clarity, this model shall be referred to as the SRE - Specified Reaction Efficiency - model, or simply the ”constant γ” model. On the literature there is no universal naming convention for it.

The second objective consisted in a preliminary formulation of the Finite-Rate Surface Chemistry (FRSC) model. The FRSC model serves 2 purposes. On one hand it is able to model catalytic reactions more rigorously than the SRE model. It is more rigorous because the SRE model is phenomenological while the FRSC follows the physics of the surface reactions. On the other hand the FRSC approach is able to completely model surface altering reactions (e.g., sublimation) that lead to surface consumption and are the basis for non-charring ablation. The FRSC model was developed by MacLean et al. [17, 20] for the DPLR code of NASA Ames, but has also been implemented in LeMANS by Alkandry et al. [21] and used by Abhilasha Anna [11]. There is a vast gap - from both a theoretical and CFD implementation point of view - between the SRE and FRSC models. As such, the objective regarding the FRSC model consisted in developing a code external to SPARK that permits to verify surface reactions decoupled from the flow field. This stand alone code is a preliminary step before a full implementation of the FRSC onto SPARK.

1.4 Thesis Outline

The natural way to divide this thesis is between the SRE and FRSC model because they are very distinct and were developed independently. The thesis presents both topics separately, meaning that there is a theoretical introduction, implementation and results section for each one individually and in different parts of this document. The bulk of the work of this thesis was devoted to the SRE model, and thus it makes up most of this report, namely chapters 2, 3 and 4. In contrast, everything related with the FRSC model is presented in chapter 5. It is important to note that there are a lot of similarities between an SRE implementation and a FRSC implementation on a CFD code but for the limited functionalities of the FRSC developed in this thesis, the FRSC model is independent on the SRE model.

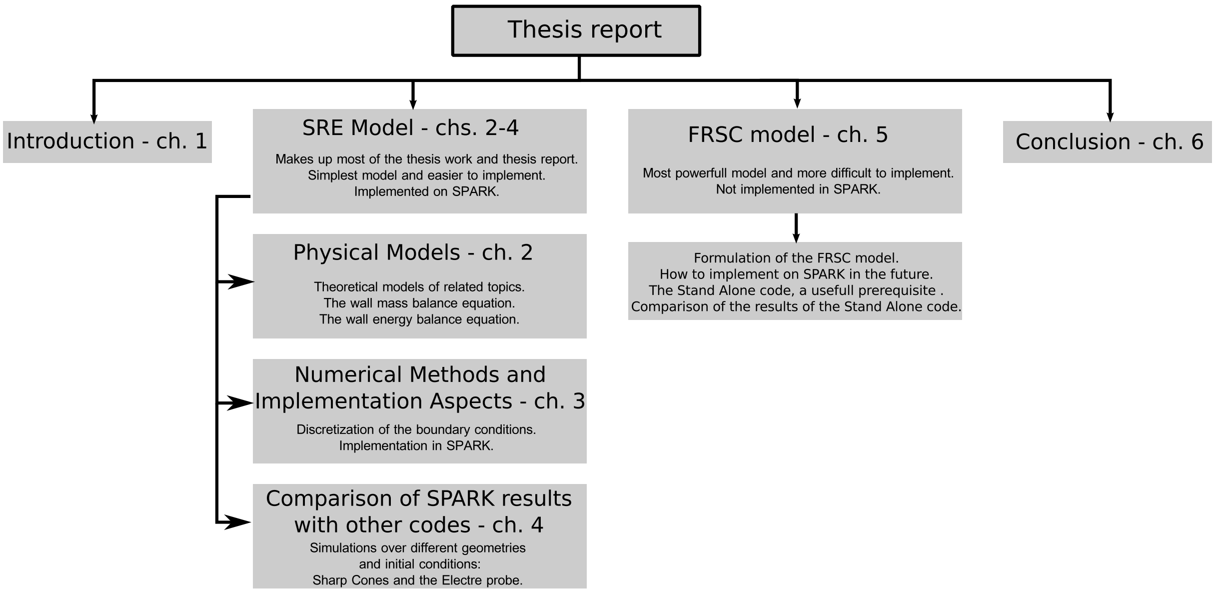

Figure 1.3: RoadMap for the thesis report.

The second chapter begins with an overall account of the relevant aspects of re-entry simulations. Then it describes the approaches commonly used to model catalycity, followed by a detailed discussion of the role of the mass and energy balances.

On the third chapter the techniques used by SPARK to deal with boundary conditions are introduced. This is followed by the numerical discretization of the analytical boundary conditions derived on chapter 2 and their implementation on SPARK.

The fourth chapter presents various CFD simulations using SPARK and the results are compared with experimental data and other numerical codes. The goal here is to judge whether the objectives were met, that is, if catalycity was correctly implemented in SPARK. When discrepancies are found between the results, informed discussions often requiring topics introduced on the background chapter, ensue.

Lastly, chapter five is entirely devoted to the FRSC model. On its sections, the original formulation on surface chemistry is presented, followed by a rationale on how to fully implement the model in SPARK in the near future and ending with a comparison of the results with MacLean et al. [17, 20].

Chapter 2

Physical Models

Adding new catalytic features to SPARK can not be done disregarding the rest of SPARK itself. In other words, the catalytic module cannot be developed in a black-box approach, in which the implementation would receive input data from the main code, process it, and return output. Because catalycity depends on the flow-field it is intertwined with other phenomenon particular to aerothermodynamics, such as high-temperature thermodynamic properties, non-equilibrium effects, and transport properties. Adding to this, catalycity directly effects the flow field (particularly the flow field near the wall) which becomes evident during the post-processing of the results. For this reasons it is necessary to study certain aspects of aerothermodynamics as a background for the correct implementation of catalycity and also the correct interpretation and post-processing of the results. This aspects are discussed on the following sections. Other theoretical considerations are delegated to the appendices.

This chapter describes the underlying physical models along with the governing equations that have been used in this work. As stated in the introduction, the current work has been performed using the Spark code which includes a large set of physical models related to thermodynamics, transport properties, chemical kinetics and energy exchange processes. Although a detailed description of all these models is out of the scope of this work, these models are strongly coupled to the gas-surface models which have been implemented within this master thesis. Therefore, the various physical models involved in the gas-surface processes are briefly presented here for completeness. This chapter starts by presenting the set of governing equations in section 2.1 for a multi-species, multi-temperature gas. Then, the thermodynamic relations used to described the state of a gas in high temperature conditions are given in section 2.2. The modelling of thermo-chemical non-equilibrium processes is presented in section 2.4. The last section, section 2.5, addresses the modelling of gas-surface interactions, and represent to main contribution of the current work.

2.1 Governing Equations

Re-entry flows are governed by the complete chemically reacting Navier-Stokes (NS) equations, equations (2.1 - 2.4). Their solution is the variation of the aerodynamic properties with space and time, i.e $T = T(x, y, z, t), \quad \rho = \rho(x, y, z, t), \quad \vec{u} = \vec{u}(x, y, z, t)$ etc. [22].
The set includes the continuity equation that ensures conservation of mass and the momentum equation that ensures Newton's Second Law; these two are unchanged from the case of a nonreacting gas as they only take into account mechanical considerations [1, p. 712]. The set also includes the species continuity equations for the conservation of the individual species and which take into account the production and destruction of species through $\dot{w}_i$. The energy equation is the last one and secures energy is neither created or destroyed. In addition, when thermal nonequilibirium is present more equations are added.

- Continuity:

$$\frac{\partial \rho}{\partial t} + \vec{\nabla} \cdot (\rho \vec{u}) = 0 \tag{2.1}$$

- Species Continuity (one equation for each species i):

$$\frac{\partial (\rho c_i)}{\partial t} + \vec{\nabla} \cdot (\rho c_i \vec{u}) = \vec{\nabla} \cdot \vec{J_i} + \dot{w}_i \tag{2.2}$$

- Momentum:

$$\frac{\partial (\rho \vec{u})}{\partial t} + \vec{\nabla} \cdot (\rho \vec{u} \otimes \vec{u}) = \vec{\nabla} \cdot [\tau] - \vec{\nabla} p \tag{2.3}$$

- Total Energy:

$$\frac{\partial (\rho E)}{\partial t} + \vec{\nabla} \cdot (\rho E \vec{u}) = \vec{\nabla} \cdot \left(\vec{q_C} + \sum_i \vec{J_i} h_i + \vec{u} \cdot [\tau] - p\vec{u} \right) \tag{2.4}$$

Where:

$$\vec{J_i} = \rho D_i \vec{\nabla} c_i \tag{2.5}$$

$$\vec{q_C} = k \vec{\nabla} T \tag{2.6}$$

2.2 Thermodynamic Relations

Aerothermodynamics requires a microscopic description of the gas. The gas is assumed to be made of a large number of molecules and atoms. These molecules have four modes of energy which are illustrated on figure 2.1. The total energy of a molecule is the sum of the energies of the 4 modes, namely translation, rotational, vibrational and electronic energies:

$$\varepsilon = \varepsilon_{trans} + \varepsilon_{rot} + \varepsilon_{vib} + \varepsilon_{el} + \varepsilon_0 \tag{2.7}$$

Due to conventions [2, p. 129] ε_0, representing the zero point energy, which is equal to the energy of the molecule at absolute zero [1, p. 507] has to be added. This means that ε_{trans}, ε_{rot}, ε_{vib} and ε_{el} are energies above the zero-point energy at T = 0 K. A Boltzmann distribution is assumed, which means the thermodynamic properties are computed assuming statistical thermodynamics. Assuming a Boltzmann distribution is common practice in all the CFD codes in existence. This is mainly because of the computational cost of not assuming a Boltzmann distributions, i.e the State-to-State approaches, is currently too high to be practically considered other than in simplified time relaxation or steady-state models.

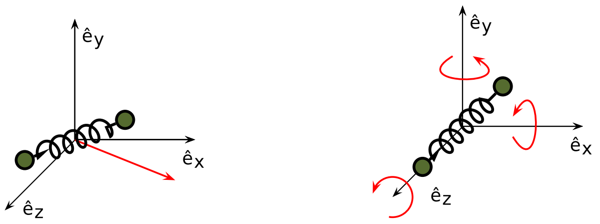

(a) Translational energy ε_{trans} (a) Rotational energy ε_{rot}

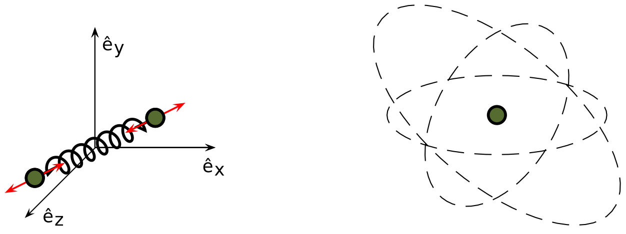

(a) Vibrational energy ε_{vib} (a) Electronic energy ε_{el}

Figure 2.1: Modes of molecular energy. Reproduced from [23].

Accordingly, from statistical thermodynamics, the internal energy per unit mass of a pure chemical species i is:

$$\begin{cases} e_{trans} = \dfrac{3}{2} R_i T \\ e_{rot} = R_i T \\ e_{vib} = \dfrac{h\nu/kT}{e^{h\nu/kT} - 1} R_i T \\ e_{el} = e_{el} \end{cases} \tag{2.8}$$

$$e_i = \frac{3}{2}R_iT + R_iT + \frac{h\nu/kT}{e^{h\nu/kT} - 1}R_iT + e_{el} + (\Delta h_f)_i^0 \tag{2.9}$$

Where R_i is the specific gas constant and ν is the vibrational frequency of the molecule.

The previous is for a single chemical gas species. The first 4 energies are measured above the zero-point energy while e_i is the absolute energy. $(\Delta h_f)_i^0$ is heat of formation of species i per unit mass, and embodies an effective zero point energy [1, pp. 245, 557].

For a mixture of such gases, the internal energy per unit mass of mixture is:

$$e = \sum_i c_i e_i \tag{2.10}$$

Where e includes the zero-point energy through e_i, and c_i is the mass fraction of species i.

The specific enthalpy for a single gas species and for a mixture is given by equations (2.11) and (2.12) respectively:

$$h_i \equiv \left(e + \frac{p}{\rho}\right)_i = e_i + R_iT \tag{2.11}$$

$$h = \sum_i c_i h_i \tag{2.12}$$

Furthermore, the specific heat at constant volume, C_v, and the specific heat at constant pressure, C_p, are defined as:

$$C_v \equiv \left(\frac{\partial e}{\partial T}\right)_v \qquad \text{and} \qquad C_p \equiv \left(\frac{\partial h}{\partial T}\right)_p \tag{2.13}$$

Introducing (2.10) and (2.12) into expressions (2.13):

$$\begin{cases} C_v = \sum_i \left(c_i \frac{\partial e_i}{\partial T} + e_i \frac{\partial c_i}{\partial T}\right) \\ C_p = \sum_i \left(c_i \frac{\partial h_i}{\partial T} + h_i \frac{\partial c_i}{\partial T}\right) \end{cases} \tag{2.14}$$

For CFD applications, the thermodynamic properties previously discussed - namely energy, enthalpy and specific heats - need to be obtained for use during the calculations. Using the aforementioned expressions for their computation at running time is the most obvious approach. This means expressions (2.9 - 2.14) are explicitly evaluated as the code runs. However, due to convenience, two other approaches have been frequently used by CFD codes to access the properties when the mixture is air. There are several tables with the thermodynamic properties of an air mixture and/or of the species present in it (e.g., N_2, O_2 etc.) [24]. These tables can be incorporated on the CFD code which interpolates between its discrete entries when necessary or, in alternative, the data of these tables can be correlated through polynomial expressions, and these used directly by the code.

2.3 Transport Properties

There are 3 transport coefficients to account for dissipative effects: Viscosity, thermal conductivity and the diffusion coefficient. For catalycity only the diffusion coefficient D_i is relevant.

There are various models to compute the diffusion coefficient, which vary in terms of ”exactness” and computational expensiveness. For all the simulations performed under the current work in SPARK, only the most simple approach for D_i was used. It consists in assuming a constant Lewis number Le, and evaluating the expression:

$$D_i = \frac{Le\,k}{\rho C_p} \tag{2.15}$$

Where C_p is the total specific heat at constant pressure and k is the thermal conductivity.

The model (2.15) is not derived from any physical considerations but for Le values ranging between 1 and 1.4, it gives good estimates for the diffusion coefficient. It is thus a straightforward, computational inexpensive approximation that has a practical advantage over more advanced models in which $D_i = f(c_i, p, T)$ and that are more expensive.

The Lewis number on the SPARK simulations was changed according to the value used in the results being emulated. By default SPARK uses Le = 1.2.

2.4 Nonequilibrium Processes

Let us imagine the flow of an element of fluid through a continuously changing steady state field. When equilibrium is assumed, this fluid element is supposed to instantaneously adapt, as it moves through the flow, to the local p and T. However, this is never the case because this adaptation occurs through molecular collisions, that take time and are thus not instantaneous [1, 2]. The question then arises of when is thermodynamic equilibrium a valid approximation to describe this fluid element. If the characteristic time of the collisional processes τ_c to achieve equilibrium is of the same order as the characteristic time of the gas flow τ_f ($\sim \frac{l}{V_\infty}$ where l is a characteristic length) then equilibrium is not at all suitable and nonequilibirum must be taken into account [2, p. 197]. If, on the contrary, the characteristic time for collisions is negligible when compared with the characteristic flow time as on described in (2.16), thermodynamic equilibrium is a very practical and applicable approximation.

$$\begin{aligned} \text{Nonequilibrium :}&\tau_f \sim \tau_c \\ \text{Equilibrium :}&\tau_f \gg \tau_c \end{aligned} \tag{2.16}$$

For the case of a re-entry vehicle, a bow shock wave will be formed ahead of the vehicle [1, 3]. Generally, across this shock wave, the p and T change in such a abrupt manner, that the fluid element will not be able to keep up[1]. Thus, a certain amount of time will be needed, after the shock, for the molecular collisions to enforce equilibrium conditions. For that reason, chemical reactions are needed to describe

---

[1] This actually depends on the density and velocity of re-entry [1, p. 647]

this flow.

The general chemical equation for the homogeneous reaction r is:

$$\sum_{i=1} \nu_{ir}^{'} X_i \rightleftharpoons \sum_{i=1} \nu_{ir}^{''} X_i \tag{2.17}$$

Where ν are stoichiometric coefficients.

It is an observable fact that the rate of formation of the various species i involved in an elementary reaction r can be expressed by:

$$\left(\frac{d\left[X_i\right]}{dt}\right)_r = \left(\nu_{ir}^{''} - \nu_{ir}^{'}\right) \left\{ k_{f,r} \prod_{i=1} X_i^{\nu_{ir}^{'}} - k_{b,r} \prod_{i=1} X_i^{\nu_{ir}^{''}} \right\} \quad \left[\frac{\mathsf{mol}}{\mathsf{m^3\,s}}\right] \tag{2.18}$$

Where $k_{f,r}$ and $k_{b,r}$ are the forward and backward reaction rates respectively, and depend only on temperature.

Remembering the discussion at the beginning of the chapter, it is now appropriate to emphasize certain aspects of this topic that are specially important further down the thesis and which are generally know as the "kinetic scheme". There are 2 considerations. On one hand, 1) the number of reactions one uses to describe a specific flow is not universally fixed and may depend to some extent on the judgement of the researcher. In a gas flow we have to ascertain the species present, then nonequilibium is outlined by all the reactions possible between those species. Despite this, only a subset of those species and reactions might be sufficient for gas-dynamic calculations. Obviously, the outcome of choosing a wrong subset is an incorrect result, but various sub-sets might correctly model the nonequilibrium. Taking the example of air, below 8000 K the only species expected to exist in significant amounts are N_2, O_2, N, O and NO [2, p. 230]. The reactions taken to be sufficient are r = 1 - 6 below, but reaction 7 is often added in which case species NO^+ and e^- should be added to the subset of relevant species.

$$\begin{aligned} r = 1 &: \mathrm{O_2 + M \rightleftharpoons 2\,O + M} \\ r = 3 &: \mathrm{NO + M \rightleftharpoons N + O + M} \\ r = 5 &: \mathrm{N_2 + O \rightleftharpoons NO + N} \\ r = 7 &: \mathrm{N + O \rightleftharpoons NO^+ + e^-} \end{aligned}$$

$$\begin{aligned} r = 2 &: \mathrm{N_2 + M \rightleftharpoons 2\,N + M} \\ r = 4 &: \mathrm{NO + O \rightleftharpoons O_2 + N} \\ r = 6 &: \mathrm{N_2 + O_2 \rightleftharpoons 2\,NO} \end{aligned}$$

Where M is any of the other species.

On the other hand, 2) the chemical rates $k_{f,r}$ and $k_{b,r}$ are generally measured by experiments whose results are correlated in an expression called the Arrhenius equation:

$$k = AT^{-n} e^{-\Theta_R / kT} \tag{2.19}$$

Where A, n and Θ_R are fitted from experiments.

Because this rates are difficult to measure experimentally there is always some uncertainty on the data available [1, 2]. Besides, the rate data is constantly being updated by new models and experiments, such that the rates $k_{f,r}$ and $k_{b,r}$, for a specific elementary reaction, change over the years.

2.5 Gas-Surface Interactions

2.5.1 Species Mass Balance

When a reactive gas is considered, a boundary condition must by specified to model the species mass fractions at the wall. These models are often referred as *wall catalycity*. Several different approaches can be used to describe wall catalycity:

Non-catalytic model: In this model the surface behaves as being indifferent to the gas flow. The impinging atoms on the vehicle wall do not recombine. No diffusion occurs. Note this was the only BC model implemented in SPARK at the start of this master thesis.

Fully catalytic model: This model assumes all the incoming atoms recombine into molecules releasing heat into the surface thus providing an upper bound for the heat flux into the vehicle.

Partially catalytic model: This model assumes that only a fraction of the incoming atoms recombines at the wall. The first two models are therefore particular cases. This was the model implemented on SPARK. On this thesis it is referred as the Specified Reaction Efficiency (SRE) model.

Super catalytic model: This model imposes the composition at the wall to be equal to the free-stream composition.

The equilibrium wall model: This model assumes that the wall composition is the equilibrium composition at the wall pressure and temperature.

Finite-rate model: This model accounts for the actual chemical processes occurring on the surface. It is a very advanced model based on the actual microscopic steps involved in a surface reaction. On this thesis it is referred as the FRSC model.

Note that the fully catalytic model is physically consistent in the sense that it represents the overall efficiency of all microscopic reactions concerning a particular species i. On the other hand, the super-catalytic and the equilibrium wall models have no physical significance because there is no mechanism to impose, for example, the wall and free-stream compositions to be equal. They are used in some CFD codes because for Earth re-entry they provide results similar to the fully-catalytic model and because they are easier to implement.

Species boundary condition

All the expressions which define boundary conditions follow from one or several physical principles. On a catalytic wall these principles are the mass balance of species i at the energy conservation at the wall. We know, by Fick's Law of diffusion, that when in a given mixture there is a gradient of mass fraction of a given species i , there will be a mass motion of this species in the direction opposite of the gradient. For a gas with more than two species, the flux $\mathbf{j}_i$ of this particles is approximately given by equation (2.20) where the minus sign requires the flux to be opposite to the gradient.

$$\mathbf{j}_i = -\rho D_i \nabla c_i \tag{2.20}$$

Where D_i is the diffusion coefficient of species i and ρ is the density of the mixture.

Given the direction n, normal to the surface on figure 2.2, the mass flux into the wall is given by (2.21). If the slope at the wall is positive, as in curve (2), there is a positive flux of species from the fluid to the wall. On the other hand, in curve (1) the slope is negative and the wall is diffusing species i into the flow.

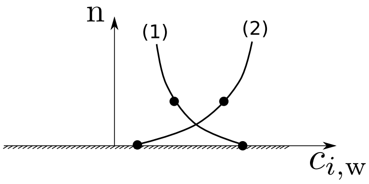

Figure 2.2: Mass fraction profile of species i normal to the wall.

$$(j_i)_{\text{w, into the wall}} = \left(\rho D_i \frac{\partial c_i}{\partial n}\right)_{\mathrm{w}} \tag{2.21}$$

We are now in a position to derive the boundary condition. Referring to illustration 2.3, if we imagine a control volume that envelops the flow/surface interface, in steady state, the net rate of diffusion of species i to the surface must be balanced to the rate at which species i is being destroyed due to catalycity.

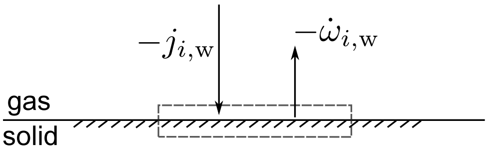

Figure 2.3: Mass wall balance of species i at the wall.

It is important to address a misnomer supported by some authors [25, 26]. The physical principle at play here is not the mass conservation of species i which does not occur since each species is literally being destroyed or created but rather a steady-state mass balance. There is however a mass (or number) conservation of chemical elements independent of their molecular configuration (i.e. 2 O atoms in a O_2 molecule). This physical principle is used further down the implementation.

For this purpose, let $\dot{\omega}_{i,\mathrm{w}}$ be the production of species i (mass of species i per second per unit area). Henceforth, at the wall, the rate at which species i diffuses into the wall must be balanced by the surface amount of its destruction, which given the definition above, is $(-\dot{\omega}_{i,\mathrm{w}})$:

$$\begin{aligned} (j_i)_{\text{w, into the wall}} &= (-\dot{\omega}_{i,\mathrm{w}}) \Leftrightarrow \\ -\left(\rho D_i \frac{\partial c_i}{\partial n}\right)_{\mathrm{w}} &= (\dot{\omega}_{i,\mathrm{w}}) \end{aligned} \tag{2.22}$$

Modelling the Source Terms $\dot{\omega}_{i,\mathrm{w}}$

The specified reaction efficiency (SRE) model follows when one looks at the flow near a wall from a macroscopic point of view. That is, we realize that near a wall there are some atoms impinging on it. Thus, it is natural to assume from that amount of atoms only a portion will recombine into molecules, while the other part will be reflected. Such mechanism is illustrated in figure 2.4. The fraction of incident atoms impinging on the surface that recombine is referred as recombination coefficient of reaction efficiency and defined as γ :

$$\gamma_i \equiv \frac{|M_i|}{|M_i^{\downarrow}|} \tag{2.23}$$

Where $|M_i^{\downarrow}|$ is the mass flux of atoms towards the surface, and $|M_i|$ is the mass flux of actual recombining atoms.
As there can't be more atoms recombining that those arriving at the surface, it is physically inconsistent to have $\gamma_i > 1$. The limiting case $\gamma_i = 1$, translates to say that all the incoming atoms recombine. On the other extreme, when $\gamma_i = 0$ all the atoms are reflected. The later is designated as the non catalytic case and former as the fully catalytic. For values in between, the wall is named partially catalytic as already referred.

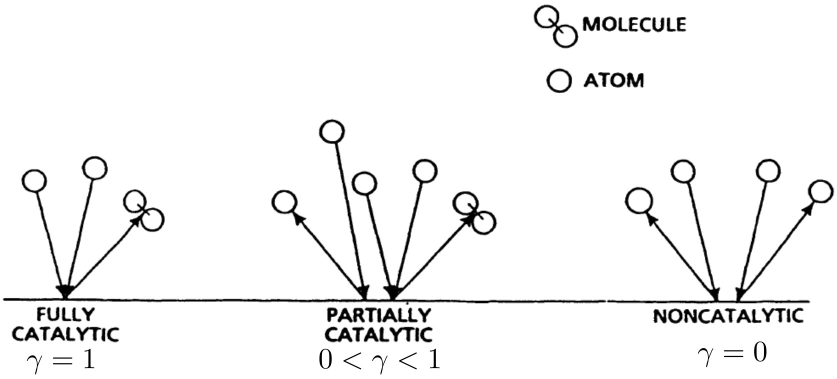

Figure 2.4: Specified reaction efficiency (SRE) recombination Model. Adapted from [27].

What is ultimately desired is an expression modelling the production term $\dot{\omega}_{i,\mathrm{w}}$, which should have units of mass of species i per second per unit area. Notice that the production term is in fact $|M_i|$ both from its description and units. Hence we need $|M_i^{\downarrow}|$ so that $\dot{\omega}_{i,\mathrm{w}}$ = $\gamma_i|M_i^{\downarrow}|$. In turns out that the expression for the mass flux of atoms impinging on the surface, $|M_i^{\downarrow}|$, follows from kinetic theory [28]. More specifically it is the result of the integration of the mass fluxes over the distribution functions. Such derivation is outside the scope of this thesis and is explained by Scott [29]. One form of the final result states:

$$M_i^{\downarrow} = c_{i,\mathrm{w}}\rho_{\mathrm{w}}\sqrt{\frac{R_i T_{\mathrm{w}}}{2\pi}}, \quad [\mathrm{kg\,m^{-2}\,s^{-1}}] \tag{2.24}$$

Catalycity in SPARK was implemented for air environments for which there are 3 reactions of interest [19]:

$$\begin{aligned} \mathrm{N} + \mathrm{N} &\longrightarrow \mathrm{N}_2 \\ \mathrm{O} + \mathrm{O} &\longrightarrow \mathrm{O}_2 \\ \mathrm{N} + \mathrm{O} &\longrightarrow \mathrm{NO} \end{aligned} \tag{2.25}$$

Amongst these, recombination of nitrogen oxide is less important than the other two [19, 30] and was thus ignored. Given the definition for γ and also (2.24) and (2.25) the production terms for incoming atoms are:

$$\begin{aligned} \dot{\omega}_{\mathrm{N,w}} &= -\gamma_{\mathrm{N}} c_{\mathrm{N,w}} \rho_{\mathrm{w}} \sqrt{\frac{R_{\mathrm{N}} T_{\mathrm{w}}}{2\pi}} \quad \left[\mathrm{kg\,m^{-2}\,s^{-1}}\right] \\ \dot{\omega}_{\mathrm{O,w}} &= -\gamma_{\mathrm{O}} c_{\mathrm{O,w}} \rho_{\mathrm{w}} \sqrt{\frac{R_{\mathrm{O}} T_{\mathrm{w}}}{2\pi}} \quad \left[\mathrm{kg\,m^{-2}\,s^{-1}}\right] \end{aligned} \tag{2.26}$$

Where the minus sign was inserted for agreement with the previous definition of $\dot{\omega}_{i,\mathrm{w}}$, positive for production.

The production terms for the products N_2 and O_2 follow from (2.26) and the principle of element conservation [28, pp. 3-4]. The net number of atoms produced regardless of their molecular arrangement must equal 0. For the 2 reactions considered this states, in terms of mass:

$$\begin{aligned} \dot{\omega}_{\mathrm{N_2,w}} + \dot{\omega}_{\mathrm{N,w}} = 0 \Leftrightarrow \dot{\omega}_{\mathrm{N_2,w}} &= \gamma_{\mathrm{N}} c_{\mathrm{N,w}} \rho_{\mathrm{w}} \sqrt{\frac{R_{\mathrm{N}} T_{\mathrm{w}}}{2\pi}} \\ \dot{\omega}_{\mathrm{O_2,w}} + \dot{\omega}_{\mathrm{O,w}} = 0 \Leftrightarrow \dot{\omega}_{\mathrm{O_2,w}} &= \gamma_{\mathrm{O}} c_{\mathrm{O,w}} \rho_{\mathrm{w}} \sqrt{\frac{R_{\mathrm{O}} T_{\mathrm{w}}}{2\pi}} \end{aligned} \tag{2.27}$$

The above expressions have not been hard-coded into SPARK. Instead SPARK has been incorporated with a versatile stratagem to compute the production rates $\dot{\omega}_{i,\mathrm{w}}$ of reactants and products involved in a reaction. The stratagem was influenced by [31] and is versatile because it allows for extension to other environments (e.g., CO_2 in Mars) and reactions with little effort:

$$\dot{\omega}_{i,\mathrm{w}} = M_i^{\downarrow} \gamma_i \sum_r \nu(i,r) - \sum_j \sum_r \gamma_j M_j^{\downarrow} \mu(j,i,r) \tag{2.28}$$

Where $\nu(i,r) = 1$ if species i is destroyed during reaction r and 0 otherwise; and $\mu(j,i,r) = 1$ if when species j is destroyed during reaction r it produces i and 0 otherwise.

Nonetheless, for the air environment considered, SPARK indeed defaults to expressions (2.26) and (2.27). The productions terms for all other species, including NO, are $\dot{\omega}_{i,\mathrm{w}} = 0$.

The recombination coefficient, γ

The recombination coefficient represents an overall efficiency and is not based on a single chemical process like the rates for the homogeneous reactions; hence for the same reaction on the same surface there can be different values for γ depending on the temperature, pressure and gas composition. That is the price for modelling catalycity from such a macroscopic point of view.

There are two approaches for the reaction efficiency γ: either it is given as a constant or temperature dependent $\gamma = \gamma(T)$.

It is often the approach of several authors to use constant values for the recombination coefficient without any associated model (e.g., $\gamma = 0,\ 0.01,\ 0.5,\ 1$). Such capability has been implemented assuming the same coefficient for the recombination of N_2 and O_2, $\gamma_{\mathrm{O}} = \gamma_{\mathrm{N}}$, as is the standard procedure in the literature, namely on [30] and [32], later used for code verification.

On the other hand, temperature dependent reaction efficiencies are obtained from experiments. There are several models in existence. The most used on the literature are from Kolodzieg and Stewart [33], Zoby et al. [10] and Scott [9] . All have been incorporated into SPARK and are reported on (2.29) and figure 2.5:

$$\text{Scott}\begin{cases}\gamma_{\mathrm{N}} = 0.0714e^{\frac{-2219}{T_{\mathsf{w}}}} & 950 < T_{\mathsf{w}} < 1670[K] \\ \gamma_{\mathrm{O}} = 16.0e^{\frac{-2219}{T_{\mathsf{w}}}} & 1400 < T_{\mathsf{w}} < 1650[K]\end{cases} \Bigg| \ \text{Zoby}\begin{cases}\gamma_{\mathrm{N}} = 0.0714e^{\frac{-2219}{T_{\mathsf{w}}}} & 950 < T_{\mathsf{w}} < 1670[K] \\ \gamma_{\mathrm{O}} = 0.00941e^{\frac{-658.9}{T_{\mathsf{w}}}} & 800 < T_{\mathsf{w}} < 1400[K]\end{cases}$$

$$\text{Stewart}\left\{\begin{array}{ll}\gamma_{\mathrm{N}} = 6.1E-2e^{\frac{-2480}{T_{\mathsf{w}}}} & 1410 < T_{\mathsf{w}} < 1640[K] \\ \gamma_{\mathrm{N}} = 6.1E-4e^{\frac{5090}{T_{\mathsf{w}}}} & 1640 < T_{\mathsf{w}} < 1905[K] \\ \hline \gamma_{\mathrm{O}} = 40e^{\frac{-11440}{T_{\mathsf{w}}}} & 1435 < T_{\mathsf{w}} < 1580[K] \\ \gamma_{\mathrm{O}} = 39E-9e^{\frac{21410}{T_{\mathsf{w}}}} & 1580 < T_{\mathsf{w}} < 1845[K]\end{array}\right. \tag{2.29}$$

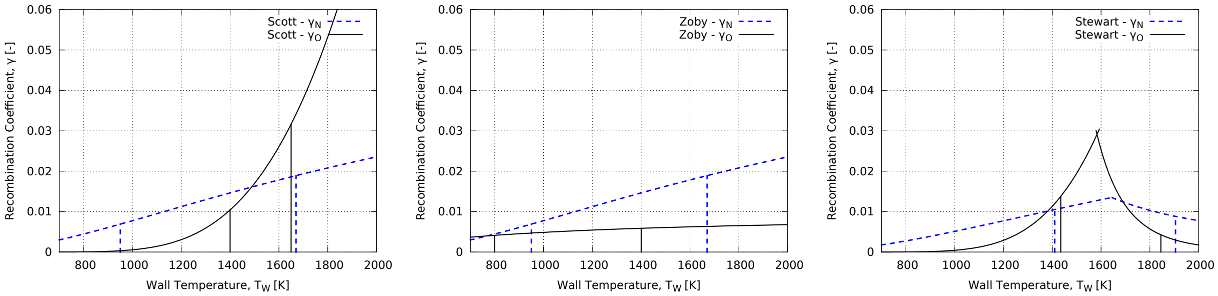

(a) Scott Model (b) Zoby et al. Model (c) Stewart et al. Model

Figure 2.5: Most used models for the recombination coefficient or reaction efficiency γ.

Given the various models available for the recombination coefficient, it is relevant to ask under what conditions to use one over another. The answer is not straightforward since the recombination coefficient is highly dependent on external properties of the flow. All the 3 models were developed to predict the heating rates for the Space-Shuttle which consists of high temperature reusable surface insulation (HRSI) coated with reaction-cured borosilicate glass (RCG) with a high silica content. Since the coating of the Space-Shuttle seeks to inhibit recombination, the coefficients of all models over their validity ranges are very low as seen on figure 2.5.

On the other hand, SPARK extrapolates for wall temperatures outside the ranges of validity of each given model as is common practice on other CFD codes. The recombination coefficient for O on Scott's model has no upper bound with increasing wall temperature as shown by equation (2.29). For this and similar cases SPARK imposes $\gamma_{\text{max}} = 1$, that is, it overrules the model to guarantee no physical inconsistent extrapolations are made.

Using any of the models with a isothermal wall boundary condition T_{w} = cte is equivalent to setting a constant value of γ since the recombination coefficient depends only on T_{w} which is constant over the entire surface. On the other hand, when the wall temperature is allowed to vary over the surface through the SEB boundary condition, there will have a different γ value on each wall cell depending on the local temperature. In this latter case, the situation could not be reproduced using a constant value for recombination coefficient γ.

2.5.2 Surface Energy Balance

Like mass fractions, temperature is also a dependent variable and thus requires appropriate boundary conditions. It is often assumed that the vehicle surface can maintain a constant temperature T_{w}, but rare are the situations this is a valid assumption. In alternative the temperature is allowed to vary along the surface but is dictated by an energy balance at the wall. As illustrated on figure 2.6, energy arrives at the surface via different mechanisms. Convection, q_{conv} originates from temperature gradients, and it may involve one or two terms, depending on the number of temperatures used in the simulation. Due to the gradients of mass of each species, diffusion contributes with as many terms as the N_s different species in the gas. The term $\dot{q}_{\text{rad-out}}$ accounts for the re-radiation by the surface assuming a constant emissivity ϵ. In SPARK the value was hard-coded to $\epsilon = 0.85$ to conform with the literature [30] whose results are latter used for code verification. Energy is also carried away to the solid interior in the form of conduction $\dot{q}_{\text{cond}}$. This term and the radiation received from the gas are harder to model and often dropped out. At (2.31) the surface is then said to be at radiative equilibrium. This was the approach implemented in SPARK which can, in alternative, use a constant wall temperature T_{w}.

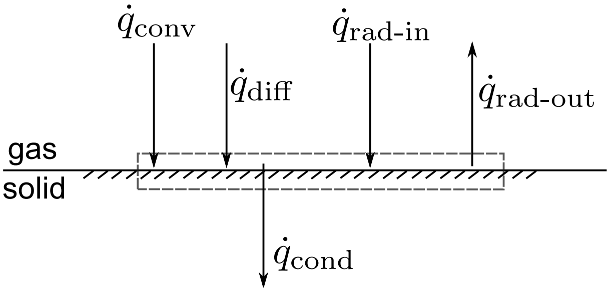

Figure 2.6: Wall energy balance. Heat fluxes over the catalytic surface.

$$\underbrace{\left(k\frac{\partial T}{\partial n}\right)_{\text{w}}}_{\dot{q}_{\text{conv}}} + \underbrace{\left(\sum_{i=1}^{N_s} h_i \rho D_i \frac{\partial c_i}{\partial n}\right)_{\text{w}}}_{\dot{q}_{\text{diff}}} + \cancel{\dot{q}_{\text{rad-in}}} = \underbrace{\epsilon\sigma T_{\text{w}}^4}_{\dot{q}_{\text{rad-out}}} + \cancel{\dot{q}_{\text{cond}}} \tag{2.30}$$

$$\left(k\frac{\partial T}{\partial n}\right)_{\text{w}} + \left(\sum_{i=1}^{N_s} h_i \rho D_i \frac{\partial c_i}{\partial n}\right)_{\text{w}} = \epsilon\sigma T_{\text{w}}^4 \tag{2.31}$$

The term $\dot{q}_{\text{cond}}$, dropped out for the surface at radiative equilibrium can be modelled correctly only if conduction is numerically solved inside the solid or by semi-analytical correlations [6]. Moreover, further terms must be account for in the case of ablation and surface recession [17, 6].

Chapter 3

Numerical Method and Implementation Aspects

This chapter describes the actual implementation of the Specified Reaction Efficiency (SRE) model in the SPARK code.

Catalycity is typically implemented as boundary conditions which enforce additional physical laws on the boundary of the computational domain. A general description of the way boundary conditions are handled in SPARK is given in sections 3.1 and 3.2. Then, the implementation of the species mass balance is addressed in section 3.3 while the details of the surface energy balance boundary condition are presented in section 3.4.

3.1 Redesign of the Boundary Condition Structure

As there are no analytical solutions to the system, the Navier-Stokes (NS) equations are discretized in space and time and solved numerically. This step is the essence of CFD, but will be deferred to appendix A as to keep this discussion concise. One aspect worth accounting presently is boundary conditions.

The governing equations are solved for a specific region in space. The boundary of this region exerts a set of additional constraints, the boundary conditions, which together with the NS determine a specific problem, as illustrated on figure 3.1.

Before the current work had been developed, SPARK had to set boundary conditions (BC) for all the dependent variables. However the way this was achieved made it hard for the new catalytic BC to be implemented. Previously SPARK did not need to recognize the existence of a wall. With the advent of catalycity, which is a surface phenomenon, the entire way SPARK implements boundary conditions had to be changed.

Since SPARK can solve several types of governing equations (perfect gas, multi-species, multi-temperature), the implementation of the BC structure should reflect this modularity. In other words, due to the versatility in which the SPARK code is written, the new boundary condition (BC) structure should perform with simulations with any combination of gas species and temperatures.

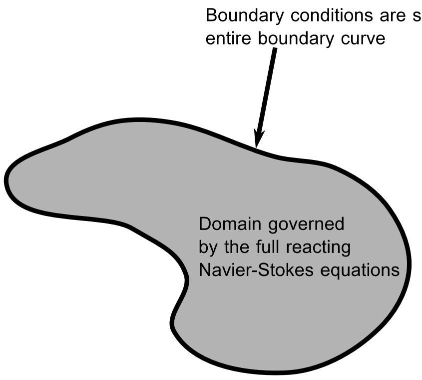

Figure 3.1: The domain governed by the Navier-Stokes equations and its boundary where boundary conditions must be specified.

The new implementation makes use of modern Fortran language using object-oriented programming (OOP) techniques:

SPARK uses block structured meshes. This means that the computational domain, i.e., the mesh, can be split in several blocks, each block being composed of four faces. Then, each face can be composed of several patches to account for different types of BC. The concept of a *wall* is introduced on this patch by virtue of allowing the patch to have a structure named STATE that saves all the flow variables of the patch. In other words the patch, which is defined on a boundary, has now the capability to store and operate with variables that characterize the boundary. The rationale is exemplified on figure 3.2 where

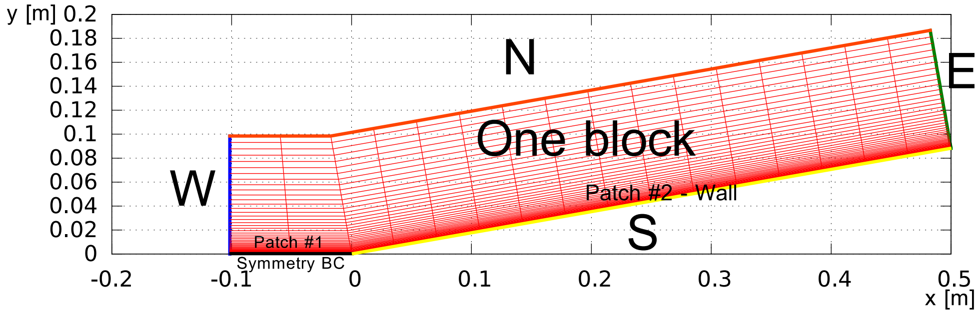

Figure 3.2: Actual mesh used on this thesis for a SPARK simulation over a sharp cone. The inflow comes from the W face. The mesh has only one block.

N, S, E, W are the four faces of the block, and face S has two patches, the second patch corresponding to an actual wall. Therefore this patch is provided with a structure named STATE which stores flow variables like mass fraction c_i of each species i, the various temperatures present in the model T, T_v , etc., the density ρ and all the other flow variables. This variables are distinguished with the subscript w, for example $c_{i,\mathrm{w}}$ or T_w . This wall variables are then used on the implementation of catalytic boundary conditions, as will become apparent on the next section.

3.2 Ghost Cell Concept

Enforcing boundary conditions (BC) on a CFD code can be done in a number of ways. In the case of SPARK and other codes [26], the computational domain is extended beyond the region governed by the

NS equations with two ghost cells as exemplified on figure 3.3. Then, at each iteration, the information (i.e the flow variables ρ, T, p, etc) at this ghost cells is imposed as to conform with the boundary conditions. While the ultimate objective is to update the ghost cells, this is done by first applying a given boundary condition at the wall, obtaining as a consequence new wall variables, and only then is the ghost cell value imposed. As an example, we can imagine a specified temperature flux into the wall in figure 3.3:

$$\left(\frac{\partial T}{\partial y}\right)_{\text{wall}} = q_{\text{specified}} \tag{3.1}$$

Discretizing the derivative at the wall:

$$\frac{T_{i,j} - T_{\text{w}}}{\Delta n} = q_{\text{specified}} \Leftrightarrow \tag{3.2}$$

$$\Leftrightarrow T_{\text{w}} = T_{i,j} - q_{\text{specified}} \Delta n \tag{3.3}$$

Where i and j are the indexes of the cells on the figure and Δn is the distance between the first cell and the wall.

Then the temperature at the ghost cell is set by a linear extrapolation of the value at the wall and the first internal cell:

$$T_{i,j-1} = 2T_{\text{w}} - T_{i,j} \tag{3.4}$$

$$\text{In this case: } T_{i,j-1} = T_{i,j} - 2\Delta n q_{\text{specified}} \tag{3.5}$$

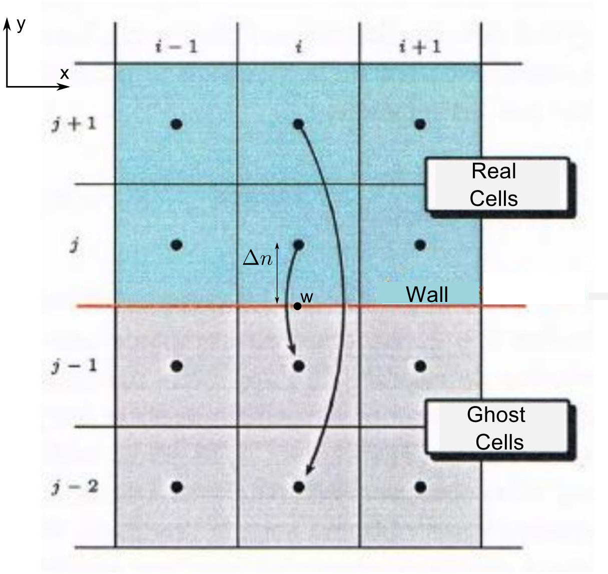

Figure 3.3: The extension of the domain with 2 rows of ghost cells. i and j are indexes. Adapted from [23].

The advantage of this approach to deal with the boundary conditions is that the cells near the outer bounds of the domain, i.e., the first cells after a boundary, can be discretized exactly like the remaining internal/real cells. For example, the discretization of the internal cell $(i,\ j+2)$ (not shown on figure 3.3), depends on the surrounding cells including cells $(i,\ j+1)$ and $(i,\ j)$. On the same grounds, the discretization of a cell near the boundary, say cell $(i,\ j)$, can be made just as easily by the existence of the ghost cells. If these did not exist, the discretization of that cell would require a different approach, that would result in a different mindset for the discretization of the internal real cells and the border real cells.

3.3 Implementation of the species mass balance

Expression (2.22) is the analytical boundary condition resulting from the wall mass balance.

$$-\left(\rho D_i \frac{\partial c_i}{\partial n}\right)_{\mathrm{w}} = (\dot{\omega}_{i,\mathrm{w}}) \tag{2.22 revisited}$$

For the numerical implementation, we proceed with a 1^{st} order approximation of the gradient as given by:

$$\left(\frac{\partial c_i}{\partial n}\right)_{\mathrm{w}} = \frac{(c_i)_{\mathrm{i}} - (c_i)_{\mathrm{w}}}{\Delta n} \tag{3.6}$$

where $(c_i)_{\mathrm{i}}$ and $(c_i)_{\mathrm{w}}$ are the mass fractions at the internal cell closest to the wall and the wall respectively, and Δn is the distance between the cell and the wall as figure 3.4 illustrates.

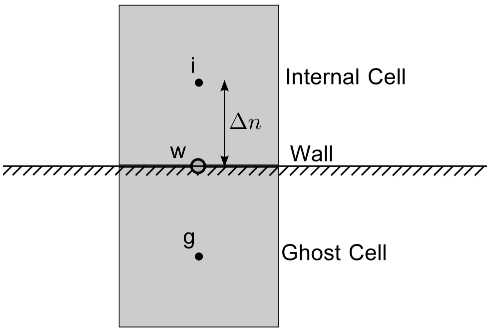

Figure 3.4: Finite volume cells at the Wall.

Inserting (3.6) into (2.22), and noting that (2.22) is valid for every instant in time:

$$c_{i,\mathrm{w}}^{n} = c_{i,\mathrm{i}}^{n} + \dot{\omega}_{i,\mathrm{w}}^{n} \cdot \left(\frac{\Delta n}{\rho_{\mathrm{w}} D_{i,\mathrm{w}}}\right)^{n} \tag{3.7}$$

where the superscript n indicates a discretized time instant.

The unknown of the above equation is the wall mass fraction of i, $c_{i,\mathrm{w}}$. Following from the discussion on ghost cells the final objective is to update the value at the ghost cell. Thus once the value at the wall is known, the ghost cell value is linearly extrapolated according with:

$$c_{i,\mathrm{g}} = 2c_{i,\mathrm{w}} - c_{i,\mathrm{i}}. \tag{3.8}$$

This being said, the derivation will continue with $c_{i,\mathrm{w}}$ as the unknown.
Due to the numerical implementation of the overall CFD code, when the mass fractions at the wall are computed, there is already the information on the mass fractions of the internal cell, $c^n_{i,\mathrm{i}}$, at the same instant of time n. However, to calculate $c^n_{i,\mathrm{w}}$, the 2^{nd} term of the r.h.s of equation (3.7) is also needed. The difficulty then arises that the production term $\dot{\omega}^n_{i,\mathrm{w}}$, in general depends not only on the mass fraction of $c^n_{i,\mathrm{w}}$ but also on other species mass fractions $c^n_{k,\mathrm{w}}$, as equation (3.9) exposes.

$$\begin{aligned} &\dot{\omega}^n_{i,\mathrm{w}} = f(c^n_{k,\mathrm{w}});\ k = 1, ..., N_s; \text{ where } N_s \text{ is the number of species.} \Leftrightarrow \\ &\dot{\omega}^n_{i,\mathrm{w}} = f(c^n_{1,\mathrm{w}},\ c^n_{2,\mathrm{w}}, ...,\ c^n_{i,\mathrm{w}}, ...,\ c^n_{N_s,\mathrm{w}}) \end{aligned} \tag{3.9}$$

Equation (3.9) prevents equation (3.7) from being evaluated explicitly. For example, if we were to evaluate $c^n_{1,\mathrm{w}}$ using (3.7), we might need $c^n_{3,\mathrm{w}}$ to calculate $\dot{\omega}^n_{1,\mathrm{w}}$. However, $c^n_{3,\mathrm{w}}$ is also an unknown. The stalemate can be solved by 2 main approaches:

1. **Explicit**

   It consists in calculating $c^n_{i,\mathrm{w}}$ using for the calculation of $\dot{\omega}^n_{i,\mathrm{w}}$ the values of the mass fractions from the previous iteration, $c^{n-1}_{i,\mathrm{w}}$, which area available and are not unknowns. If for instance there are 3 species and $\dot{\omega}^n_{1,\mathrm{w}} = f(c^n_{1,\mathrm{w}},\ c^n_{2,\mathrm{w}}, c^n_{3,\mathrm{w}})$, then to compute $c^n_{1,\mathrm{w}}$ the function f is explicitly evaluated with the variables from the previous CFD iteration, $\dot{\omega}^n_{1,\mathrm{w}} = f(c^{n-1}_{1,\mathrm{w}},\ c^{n-1}_{2,\mathrm{w}}, c^{n-1}_{3,\mathrm{w}})$. This was not the solution chosen, as it may originate stability issues.

2. **Implicit**

   This more robust approach requires the Taylor series expansion of the production terms $\dot{\omega}^n_{i,\mathrm{w}}$ relative to the wall mass fractions of all species at time level n, $c^n_{k,\mathrm{w}}$. The implementation takes into account the intertwined dependencies between all the unknowns. All the unknowns are solved simultaneously in a linear system.

Hence, following the implicit approach, the production terms $\dot{\omega}^n_{i,\mathrm{w}}$ are discretized with a Taylor expansion of 1^{st} order on the wall mass fractions around the previous time interval $n-1$. Because the function has several variables, namely N_s variables:

$$\dot{\omega}^n_{i,\mathrm{w}} = \dot{\omega}^{n-1}_{i,\mathrm{w}} + \sum_{j=1}^{N_\mathrm{S}} \left(\frac{\partial \dot{\omega}_{i,\mathrm{w}}}{\partial c_{j,\mathrm{w}}} \right)^{n-1} \cdot \left(c^n_{i,\mathrm{w}} - c^{n-1}_{i,\mathrm{w}} \right) \tag{3.10}$$

Where the derivatives of the mass source terms with respect to the species mass fractions $\partial \dot{\omega}_{i,\mathrm{w}} / \partial c_{j,\mathrm{w}}$ need to be computed analytically what requires the expressions for $\dot{\omega}_{i,\mathrm{w}}$. Inserting (3.10) in (3.7) leads to:

$$c^n_{i,\text{w}} = c^n_{i,\text{i}} + \left[\dot{\omega}^{n-1}_{i,\text{w}} + \sum_{j=1}^{N_\text{S}} \left(\frac{\partial \dot{\omega}_{i,\text{w}}}{\partial c_{j,\text{w}}}\right)^{n-1} \left(c^n_{j,\text{w}} - c^{n-1}_{j,\text{w}}\right)\right] \cdot \left(\frac{\Delta n}{\rho_\text{w} D_{i,\text{w}}}\right)^n$$

Moving the unknowns, namely the wall mass fractions $c^n_{j,\text{w}}$, to the left-hand-side, this equation can, after some algebraic manipulation be arranged as:

$$\sum_{j=1}^{N_\text{S}} \left[\delta_{ij} - \alpha_i^{n-1} \left(\frac{\partial \dot{\omega}_{i,\text{w}}}{\partial c_{j,\text{w}}}\right)^{n-1}\right] c^n_{j,\text{w}} = c^n_{i,\text{i}} + \left[\dot{\omega}^{n-1}_{i,\text{w}} - \sum_{j=1}^{N_\text{S}} c^{n-1}_{j,\text{w}} \cdot \left(\frac{\partial \dot{\omega}_{i,\text{w}}}{\partial c_{j,\text{w}}}\right)^{n-1}\right] (\alpha_i)^{n-1} \tag{3.11}$$

where the term

$$\alpha_i^{n-1} = \left(\frac{\Delta n}{\rho_\text{w} D_{i,\text{w}}}\right)^{n-1}$$

has been introduced purely for convenience in the derivation and δ_{ij} is the Kronecker delta function. As expected, the implicitation of the boundary condition led to a system of algebraic equations, which can be recognized in equation (3.11) by giving all the possible values for i, which will originate N_s equations. This equations can be recognized as a linear system of the form:

$$A \cdot X = b \tag{3.12}$$

with

$$\begin{aligned}
A_{ij} &= \delta_{ij} - \alpha_i^{n-1} \left(\frac{\partial \dot{\omega}_{i,\text{w}}}{\partial c_{j,\text{w}}}\right)^{n-1} \\
b &= c^n_{i,\text{i}} + \left[\dot{\omega}^{n-1}_{i,\text{w}} - \sum_{j=1}^{N_\text{S}} c^{n-1}_{i,\text{w}} \cdot \left(\frac{\partial \dot{\omega}_{i,\text{w}}}{\partial c_{j,\text{w}}}\right)^{n-1}\right] (\alpha_i)^{n-1} \\
X &= c^n_{j,\text{w}}
\end{aligned}$$

In summary, on a given iteration n, we want to compute the wall mass fractions of all the N_s species. The information available at that time is all the unknowns at the previous time $n-1$, as well as the variables (including the mass fractions) on all internal cells, $c_{i,\text{i}}$. For a 3 species gas, this systems of equations corresponds to:

$$
\begin{bmatrix}
1+\alpha_1\left(\dfrac{\partial\dot{\omega}_{1,\mathrm{w}}}{\partial c_{1,\mathrm{w}}}\right) & \alpha_1\left(\dfrac{\partial\dot{\omega}_{1,\mathrm{w}}}{\partial c_{2,\mathrm{w}}}\right) & \alpha_1\left(\dfrac{\partial\dot{\omega}_{1,\mathrm{w}}}{\partial c_{3,\mathrm{w}}}\right) \\[2ex]
\alpha_2\left(\dfrac{\partial\dot{\omega}_{2,\mathrm{w}}}{\partial c_{1,\mathrm{w}}}\right) & 1+\alpha_2\left(\dfrac{\partial\dot{\omega}_{2,\mathrm{w}}}{\partial c_{2,\mathrm{w}}}\right) & \alpha_2\left(\dfrac{\partial\dot{\omega}_{2,\mathrm{w}}}{\partial c_{3,\mathrm{w}}}\right) \\[2ex]
\alpha_3\left(\dfrac{\partial\dot{\omega}_{3,\mathrm{w}}}{\partial c_{1,\mathrm{w}}}\right) & \alpha_3\left(\dfrac{\partial\dot{\omega}_{3,\mathrm{w}}}{\partial c_{2,\mathrm{w}}}\right) & 1+\alpha_3\left(\dfrac{\partial\dot{\omega}_{3,\mathrm{w}}}{\partial c_{3,\mathrm{w}}}\right)
\end{bmatrix}
\cdot
\begin{bmatrix}
c_{1,\mathrm{w}}^{n} \\[2ex] c_{2,\mathrm{w}}^{n} \\[2ex] c_{3,\mathrm{w}}^{n}
\end{bmatrix}
=
\begin{bmatrix}
c_{1,\mathrm{i}}-\alpha_1\left(\dot{\omega}_{1,\mathrm{w}}-\displaystyle\sum_{j=1}^{N_\mathrm{S}} c_{j,\mathrm{w}}^{n-1}\dfrac{\partial\dot{\omega}_{1,\mathrm{w}}}{\partial c_{j,\mathrm{w}}}\right) \\[2ex]
c_{2,\mathrm{i}}-\alpha_2\left(\dot{\omega}_{2,\mathrm{w}}-\displaystyle\sum_{j=1}^{N_\mathrm{S}} c_{j,\mathrm{w}}^{n-1}\dfrac{\partial\dot{\omega}_{2,\mathrm{w}}}{\partial c_{j,\mathrm{w}}}\right) \\[2ex]
c_{3,\mathrm{i}}-\alpha_3\left(\dot{\omega}_{3,\mathrm{w}}-\displaystyle\sum_{j=1}^{N_\mathrm{S}} c_{j,\mathrm{w}}^{n-1}\dfrac{\partial\dot{\omega}_{3,\mathrm{w}}}{\partial c_{j,\mathrm{w}}}\right)
\end{bmatrix}
$$

3.4 Implementation of the surface energy balance

On equation (3.9), it was assumed that the production terms $\dot{\omega}_{i,\mathrm{w}}$ depend only on the mass fractions. As seen previously they in fact also depend on temperature as emphasized on (3.13). For an isothermal wall case, this dependence does not need to be taken into account on the implicitation since T_w is prescribed along the entire surface and at all time instants.

$$\dot{\omega}_{i,\mathrm{w}}^{n} = f(c_{k,\mathrm{w}}^{n},\ T_\mathrm{w}^{n});\ k = 1, ..., N_s; \tag{3.13}$$

$$\left(k\frac{\partial T}{\partial n}\right)_\mathrm{w} + \left(\sum_{i=1}^{N_s} h_i \rho D_i \frac{\partial c_i}{\partial n}\right)_\mathrm{w} = \epsilon\sigma T_\mathrm{w}^4 \tag{2.31 revisited}$$

For the surface energy balance (SEB) the temperature at the wall T_w is evaluated via (2.31) but the diffusion terms require the derivative of the mass fractions at the wall to be already known. Since the production terms depend on T_w and they are needed to find the mass fractions at the wall this gives rise to another impasse. The most elegant solution would be to incorporate T_w on the Taylor expansion of the productions terms $\dot{\omega}_{i,\mathrm{w}}$, discretize the surface energy balance (SEB) equation (2.31) and the mass balance equation and solved them simultaneously. The outcome would be a full implicit implementation in SPARK.

Instead for the cases in which the wall temperature is not provided, SPARK deals with this coupling explicitly. The algorithm implement is exposed on figure 3.5.

After a particular CFD iteration n all the variables in all the cells are known. In particular the temperature T_i^n and the mass fraction of each species $c_{i,\mathrm{w}}^n$ are known at the first internal cell i. Also available are the wall values of this quantities from the previous iteration $n-1$: T_w^{n-1} and $c_{i,\mathrm{w}}^{n-1}$. The first step is to compute the new mass fractions at the wall $c_{i,\mathrm{w}}^n$ by solving (3.12) previously discussed; for that it is initially assumed the temperature at the wall to be T_w^{n-1}.

$$[A]\cdot\{c_{i,\mathrm{w}}^{n}\} = \{b\} \tag{3.12 revisited}$$

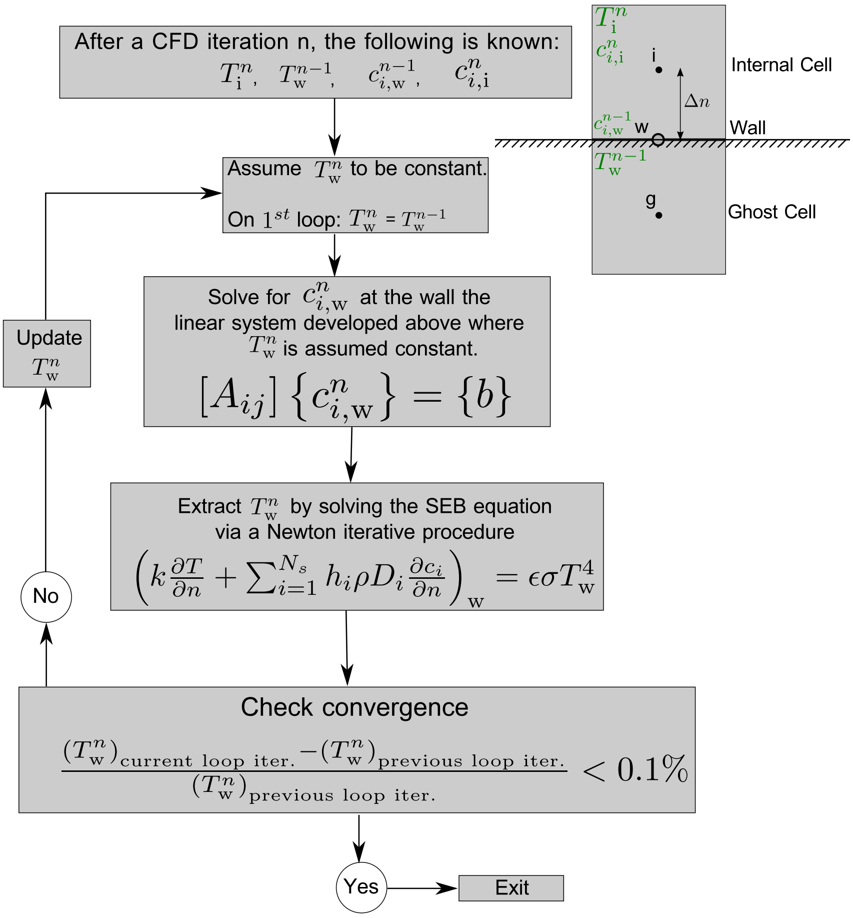

Figure 3.5: Algorithm of the explicit approach implemented on SPARK to deal with surfaces in radiative equilibrium, where T_{w} is not known a priori.

After the previous step, all mass fractions at the wall of all species at time level n are provisionally known. The second step consists in extracting a new T_{w}^{n} by solving the surface energy balance (2.31). Because the equation is non-linear, it requires a Newton iterative procedure. This temperature is then compared with the temperature initially used to solving for the mass fractions $c_{i,\mathrm{w}}^{n}$. If the results didn't converge, the new T_{w}^{n} is fed back to the linear system and the loop continues until the convergence criterion is met.

Chapter 4

Results for the Specified Reaction Efficiency (SRE) model

After incorporating catalycity in SPARK, it is crucial to assess the credibility of the implementation. That is the purpose of this chapter and to this end, SPARK is compared with experimental results and other computational simulations involving Specified Reaction Efficiency (SRE) catalycity from several different sources involving flows over different bodies and different free stream conditions. The last section tries to assess if catalycity has been correctly implemented.

The benchmark simulations and reference results chosen are illustrated on the road map of figure 4.1 below.

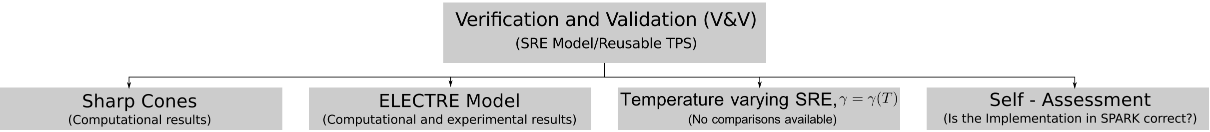

Figure 4.1: RoadMap for the chapter.

4.1 Sharp Cones

This first set of test cases from Miller et al., 1994 [30] consists in computational studies of hypersonic laminar flows over sharp cones. Their objective was to study the flow effects on walls with finite catalycity. The test cases reproduced are illustrated on the road map of figure 4.2. As seen on figure 4.3, a sharp cone is uniquely defined by its length and the aperture angle. All the cones are 0.5 m in length and have either $10°$ or $20°$ semi-aperture angles. Furthermore, the boundary conditions, either isothermal wall or SEB, with various catalytic efficiencies γ, are numerically explored.

The upstream and initial conditions for all the simulations are indicated on table 4.1. Furthermore, flows over cones at zero degree angle of attack are axisymmetrical, which means the variation of properties around its perimeter at each constant station are zero; this in turn allows the computational mesh in

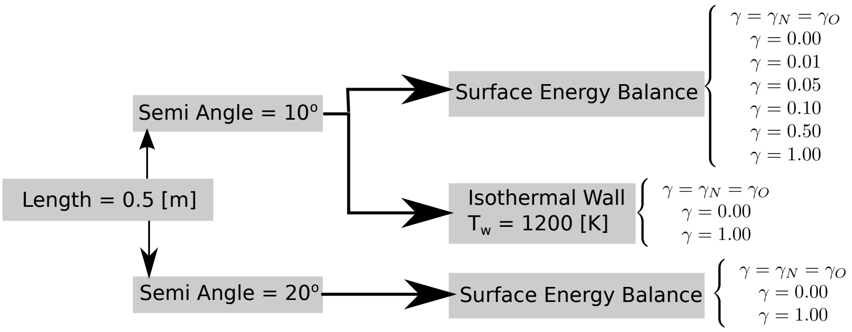

Figure 4.2: Test cases from reference [30] reproduced on this thesis.

figure 4.3 to represent solely the upper part of the cone.

Two other important notes on the computational mesh in figure 4.3 are: **1)** the mesh is denser (i.e has more points) near the cone surface in order to effectively capture the greater gradients expected there and **2)** the profile plots presented and analysed in the following pages concern the last internal cells of the mesh as illustrated by the discrete black points in the figure.

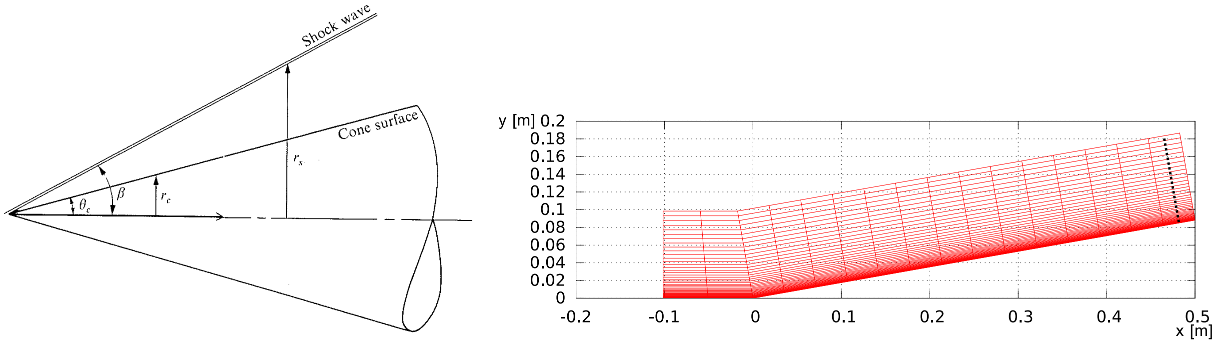

(a) 3D representation of Sharp Cone and corresponding Shock-Wave. Adapted from [1]

(b) Mesh for SPARK simulations. Example for θ = 10°, 16X50 Cells. The discrete black points represent the location of the profiles(temperature and mass fractions) of all the test cases presented next.

Figure 4.3: Cone Geometric Shape and Computational Mesh

V_∞ [m/s]	T_∞ [K]	P_∞ [Pa]	c_{N_2}[-]	c_{O_2} [-]	Species considered
8071	252.6	20.35	0.7371	0.2629	N_2, O_2, N, O, NO

Table 4.1: Upstream conditions for all the simulations over sharp cones. Refer to [30]

4.1.1 Semi-Angle = 10^0, T_w = 1200 [K]

Figure 4.4 compares the temperature profile between the results from reference [30] and the current results using the SPARK code. The profiles are nearly identical except at the shock region between $0.019 < y_{\text{normal}}$ [m] < 0.026. Of greater importance is to note that under Millers', the same temperature profile shown was obtained for both fully-catalytic (γ = 1) and non-catalytic (γ = 0) regimes. By other words, the temperature profile is independent on the mass fractions boundary condition for this particular case. The same conclusion was drawn from the SPARK simulations. This is convenient as it allows one to focus the comparison on the mass fractions alone. For example, if the temperature varied greatly

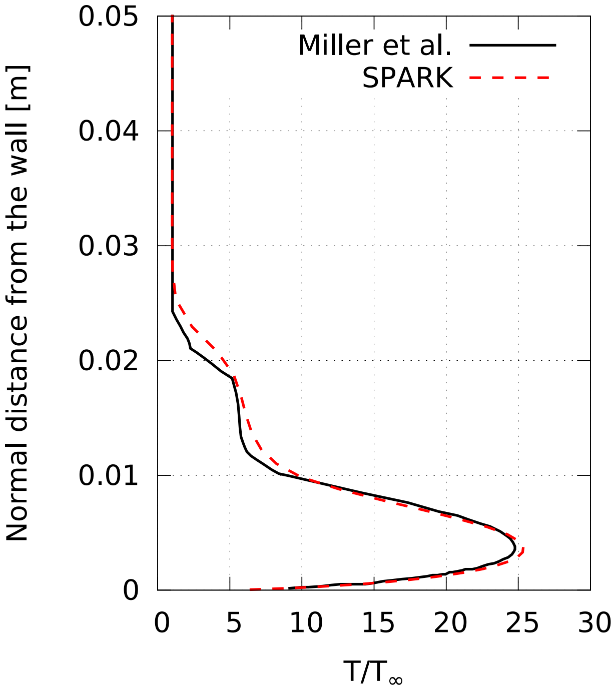

Figure 4.4: Temperature Profile normal to cone surface at $x = 0.5[m]$.($\theta = 10^o$, Isothermal Wall, $T_\text{w} = 1200[K]$)

with the catalytic efficiency and mass fractions, a disagreement between SPARK and Miller's results could come from the implementation of catalycity, the SPARK code itself or from both. Figure 4.5 allows the comparison of the mass fractions of O and NO between the SPARK runs and the computational results obtained by Miller et al. [30]. On both, the results are qualitatively and quantitatively similar.

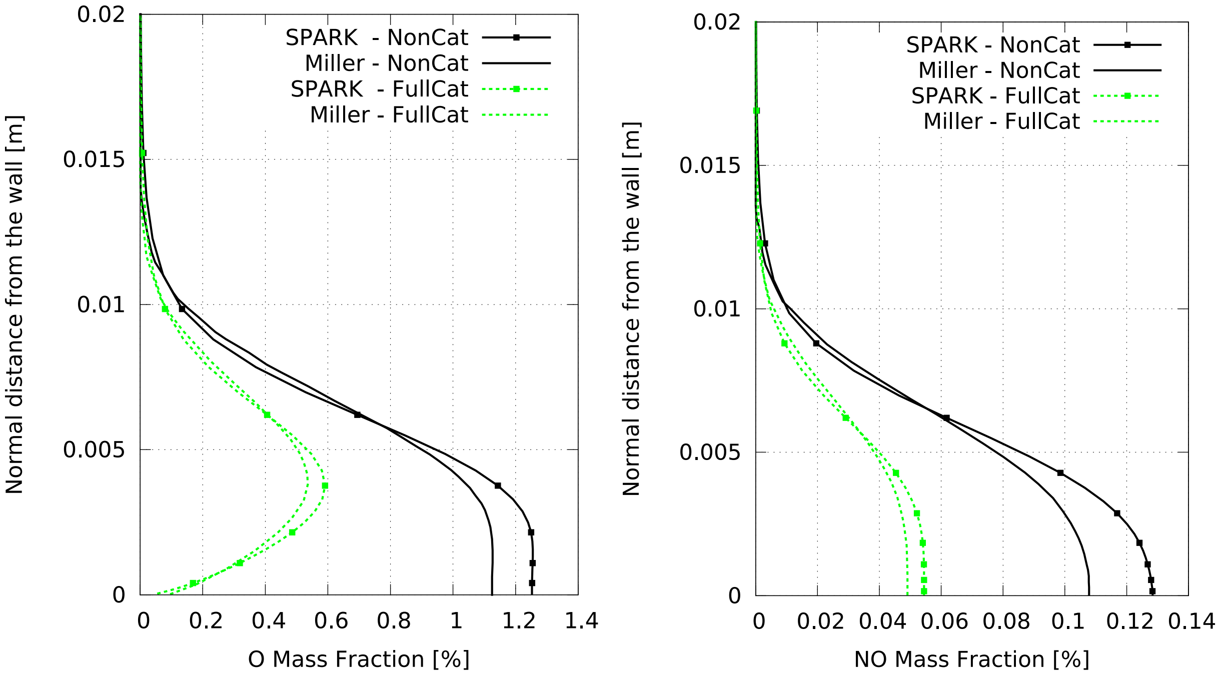

(a) O Mass Fractions

(b) NO Mass Fractions

Figure 4.5: Mass fraction comparison (Miller et al. vs. SPARK) of profiles normal to cone surface at $x = 0.5[m]$.($\theta = 10^o$, Isothermal Wall, $T_\text{w} = 1200[K]$)

SPARK tends to overestimate the mass fractions along the entire boundary layer. The error is greatest for Non catalytic conditions at the wall for both c_{O} and c_{NO}, where it reaches differences of 10% and 18% respectively. This mismatch albeit small might be explained by:

- A different enthalpy computation procedure
- Results for non catalytic condition

Firstly, although there was an effort to emulate the conditions under which Miller et al. conducted their simulations, as for example, using the same reaction kinetics and the same technique to compute the diffusion coefficients, there are certain aspects in which the codes differ. The one that may mostly effect the mass fractions is the procedure used to calculate the enthalpy which is taken into account on the energy equation of the NS set, equation (2.4). Miller et al. [30, p. 3] used a table lookup procedure using the data from Blottner, 1971 [34] to compute the specific enthalpy of all the species involved, while SPARK computes the enthalpy of each species directly from analytical expressions. The discrepancy between the two approaches is evidenced on figure 4.6. For the maximum temperature on the profile of figure 4.4, around 7000 K ($\sim$ 27$\times$252.6 K) , the enthalpy differences are about 70%$\sim$80% for N_2 and O_2, and 13%$\sim$20% for N and O. Because there is low dissociation, the discrepancy on the molecular species (N_2 and O_2) has a greater effect.

Secondly, these errors are found for the Non-Catalytic case. However, for this particular case of isothermal wall, when $\gamma = 0$, the catalytic implementation effectively defaults to the native SPARK capabilities. That is, SPARK is in practice running its standard non catalytic condition, which reinforces the conclusion that the discrepancies are due to the gas-phase portion of the code and not this works' implementation.

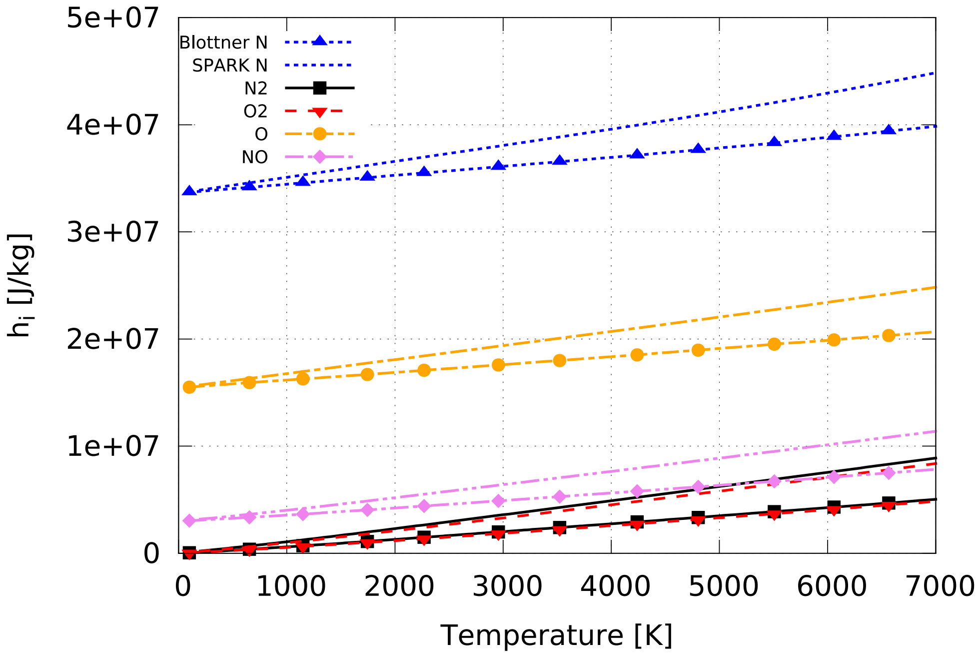

Figure 4.6: Comparison of the specific enthalpy as a function of temperature for the species shown, as determined from the data from Blottner [34] (which is used by Miller et al.) and SPARK.

4.1.2 Semi-Angle = 10^0, SEB

For the radiative equilibrium boundary condition, figure 4.7 shows the temperature profiles to be very similar. There is only a subtle under-prediction of the maximum temperature by SPARK at around y_{normal} = 0.005 m. Again, for both codes, it is verified that the catalytic boundary condition has little to no influence on the temperature profile. For this reason only a single profile is represented, valid for an arbitrary γ. This is surprising since the Surface Energy Balance (SEB) boundary condition directly couples the mass fractions and temperature at the wall, through equation (2.31).

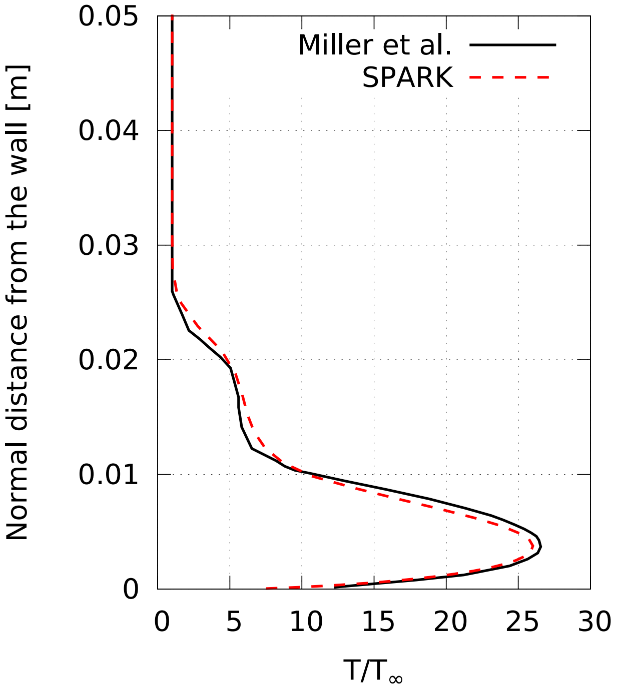

Figure 4.7: Temperature Profile normal to cone surface at $x = 0.5[m].(\theta = 10^o, SEB)$

This case is the only for which Miller et al. [30] present results for finite rate catalycity (i.e $\gamma' s$ other than 0 or 1). The mass profiles of figures 4.8 and 4.9 show a good qualitative agreement but higher quantitative differences than the previous case.

On the qualitative side, by analysing sub-figures a) and b) independently, both the non catalytic and fully catalytic conditions constitute the upper and lower limits for the mass fractions respectively, with the intermediate catalycity efficiencies having, at every constant y_{normal} station, a value greater than the immediately higher catalytic γ value, which means there are no cross overs between the profiles of each different γ. Moreover, the O mass fraction slopes at the wall of figure 4.8 are positive which through equation (2.22) means that there is only destruction and never production of O at the wall. This is physically consistent with the catalytic model implemented that allows the forward reaction $O+O \longrightarrow O_2$ but never its inverse which produces O. Similarly, the slopes of mass fraction for O_2 (profiles for O_2 not shown), $\frac{\partial c_{O_2}}{\partial n}$, are negative since O_2 can be created at the wall, but never destroyed.

On the quantitative side, the discrepancies are more apparent than for the isothermal case. There are now differences up to 100% at the wall for c_{O} when γ = 0.1 and 85% at the wall for c_{NO} when γ = 0.01. Again, some explanation of the discrepancies is possible. The discussion about enthalpy for the isothermal case remains valid, and is in fact more pertinent due to the direct inclusion of the species enthalpy (h_i) on the SEB boundary condition, equation (2.31).

$$\left(k\frac{\partial T}{\partial n}\right)_{\mathrm{w}} + \left(\sum_{i=1}^{N_s} h_i \rho D_i \frac{\partial c_i}{\partial n}\right)_{\mathrm{w}} = \epsilon\sigma T_{\mathrm{w}}^4 \qquad \text{(2.31 revisited)}$$

Additional differences in the results can be explained via[1]:

- Different C_p computation procedures
- Low levels of dissociation which increase the effect of discrepancies

Because the heat capacity, C_p, enters the expression for the diffusion coefficients through equation (2.15) and because these coefficients are inputs in the SEB, equation (2.31), a small difference on the C_p value may have a great impact on the flow field composition near the wall. Miller et al. used a look-up procedure from the data of Blottner [34] to evaluate the specific heat of the species. The differences to the values of C_p used by SPARK are present on figure 4.10, reaching 10% for $c_{p_{O_2}}$ at 7000 K. Furthermore, Miller et al. [30] assume the Lewis to be Le = 0.4 while SPARK uses a default value of 1.2. The Lewis number as a linear influence on the diffusion:

$$D_i = \frac{Lek}{\rho C_p} \qquad \text{(2.15 revisited)}$$

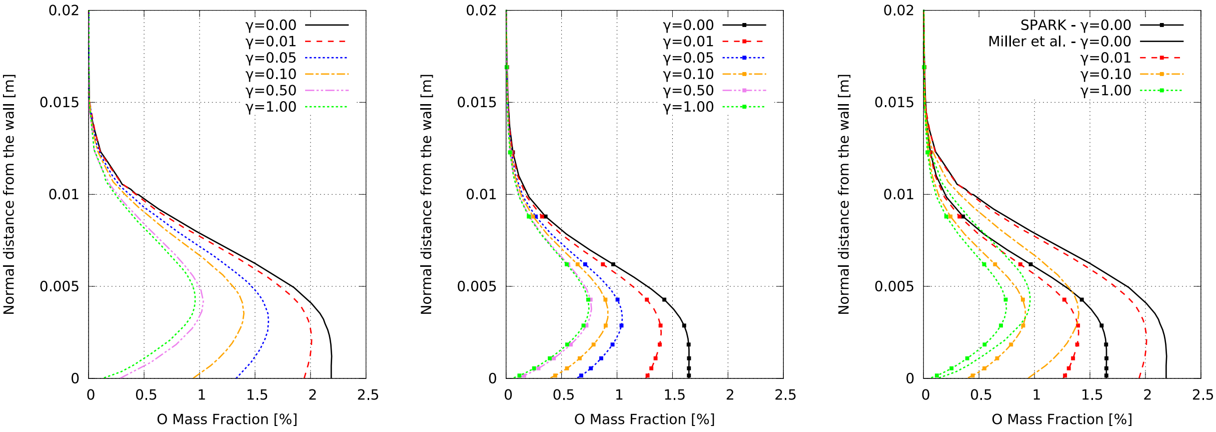

(a) Results by Miller et al. [30] (b) Current results under SPARK (c) Comparison

Figure 4.8: O mass fraction profiles normal to cone surface at $x = 0.5[m]$.($\theta = 10^o, SEB$)

At around 2% for O and 0.4% for NO the mass fraction values are very low. Accordingly, the percentual differences indicated between the SPARK results and the results from Miller et al., 85%$\sim$100%, correspond to very small, $<$1%, absolute differences. For such a small extent of dissociation, the mass fractions' results are sensitive to changes and more disposed to potentiate discrepancies. For example, a slight discrepancy on the temperature profile may, through the corresponding change in the kinetic rates, have a disproportionate effect on the mass fractions. The next case, for the 20° semi-angle, with

---

[1] This next topics are also valid for the discussion of the results of the isothermal case.

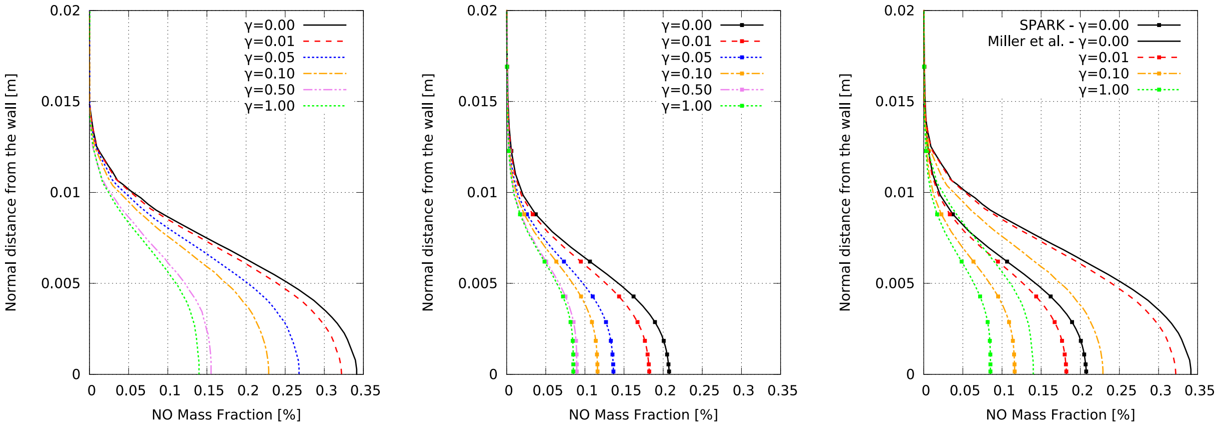

(a) Results by Miller et al. [30] (b) Current results under SPARK (c) Comparison

Figure 4.9: NO mass fraction profiles normal to cone surface at $x = 0.5[m]$.$(\theta = 10^o, SEB)$

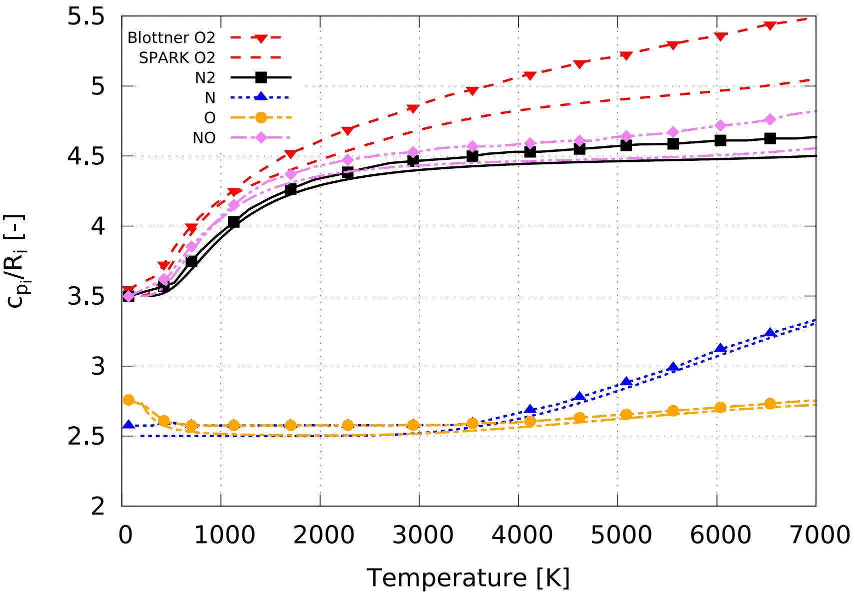

Figure 4.10: Comparison of the specific heat c_{p_i}, non-dimensionalized by the individual gas constant R_i, as a function of temperature for the species shown, as determined by the data from Blottner [34] (which is used by Miller et al.) and SPARK.

far more dissociation, might be useful for this argument. In the meantime, it is possible to verify the sensibility at these low levels of dissociation, of the mass fractions to the kinetic rates by referring to figure B.1 of the Appendix. This figure shows the current simulation but with a different kinetic scheme, namely from Park, 2001 [35]. The differences surpass 200%. Although one may argue that a small difference in temperature on the same kinetic scheme has a much lower effect than having different schemes altogether, these results undoubtedly show the sensitivity of the mass fractions to the kinetic rates, for such low dissociation degree.

4.1.3 Semi-Angle = 20^0, SEB

According with the theory of inviscid non-reactive flow over sharp cones [5] , everything else being constant, an increase on the cone aperture angle will result on a stronger shock. Hence, the temperature after the shock will be greater than for the previous case. Higher temperatures will in turn promote greater dissociation.

The temperature profiles are presented in figure 4.11, and follow the trends of the other cases. There is a good agreement with Miller's work. The differences are greater at around 0.02 $< y_{\text{normal}}$ [m] $<$ 0.03 which models the shock discontinuity. These disagreements are expected since the shock is a strong discontinuity highly dependent on discretization scheme used. The result is a slight change on shock position which carries little consequence to our catalytic considerations. More important would be the slight underestimation of the temperature occurring at y_{normal} = 0.01 m.

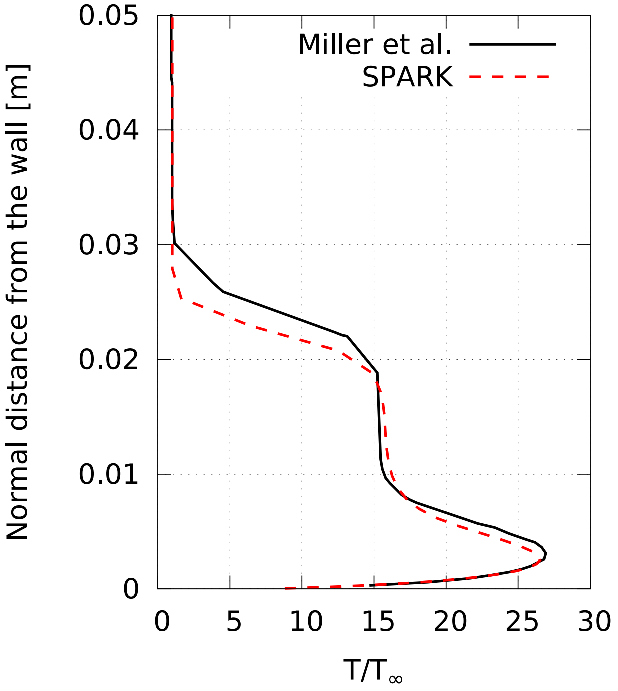

Figure 4.11: Temperature Profile normal to cone surface at $x = 0.5[m]$.($\theta = 20^o, SEB$)

Figure 4.12 shows that the increase in temperature did indeed for allow more dissociation, increasing it ten fold. For the mass fraction results, there is a good qualitative and quantitative agreement. There is a maximum difference of 20% for the NO mass fraction and 10% for O at the wall, both for the non-catalytic case. The differences have decreased, which supports the argument that the differences for the θ = 10° case were due to sensitivity at low dissociation.

For this test case, Miller et al. used a mesh size at the wall of $h_{\text{Miller et al.}}$ = 5 $\times$ 10^{-6} m, while in SPARK the height of the first cell for this and all other test cases was h_{SPARK} = 5 $\times$ 10^{-5} m (see the illustration on figure 4.13). All the attempts to use a smaller height were unsuccessful, as the simulations would either develop stability issues and crash, or take non-practicable amounts of time to converge. Obviously, a mesh has to be fine enough to capture the phenomenon of the flow, and at the wall, the presence of the boundary layer is characterized by large gradients, which require a very small cell height. However, below a certain height there is no crucial importance of decreasing it further. This being said, because the SPARK simulations can capture all the aspects of the flow, since they follow the profiles of Miller et al., it is unreasonable to conclude the mesh was the source of relevant errors.

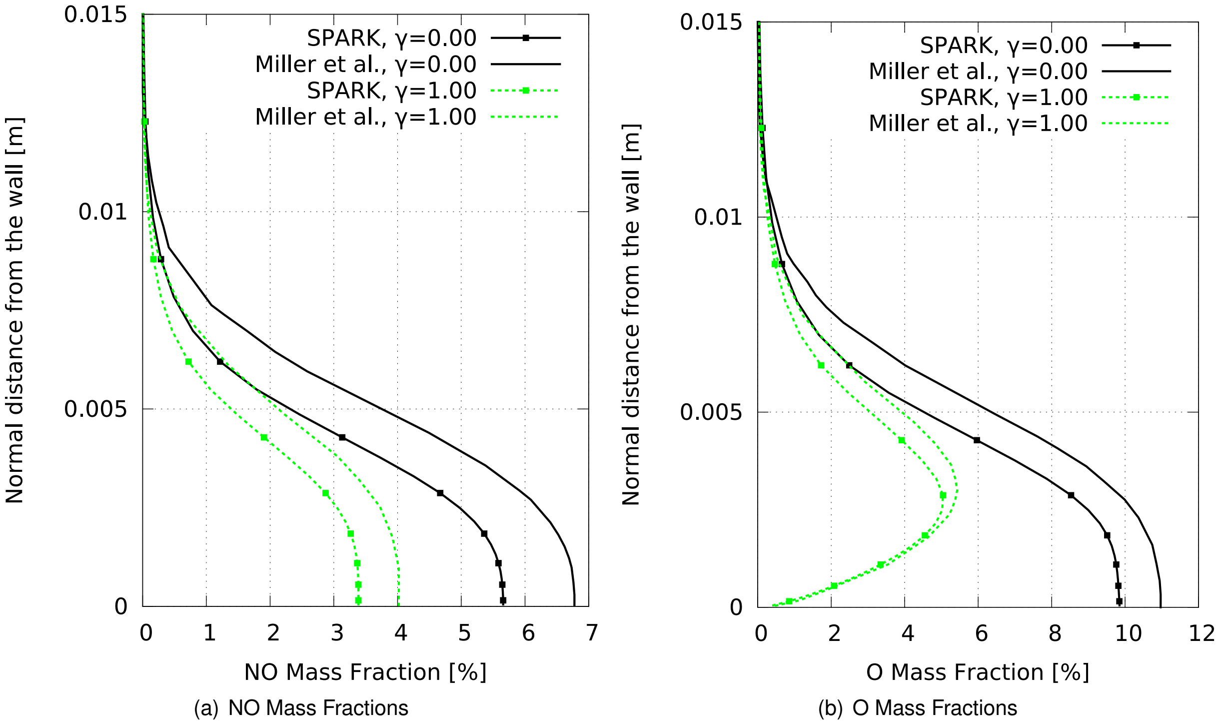

(a) NO Mass Fractions (b) O Mass Fractions

Figure 4.12: Mass fraction comparison (Miller et al. vs. SPARK) of profiles normal to cone surface at $x = 0.5[m]$.$(\theta = 20^o, SEB)$

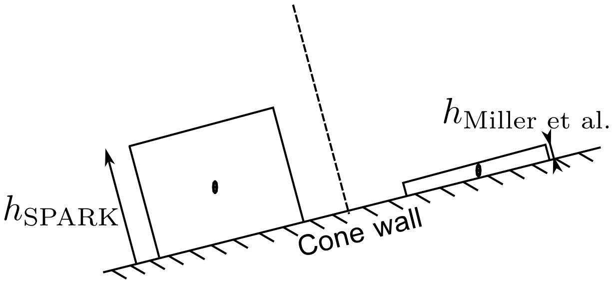

Figure 4.13: Illustration of the difference in the height of the first cell at the cone surface between the mesh used Miller et al., and the mesh of the SPARK simulations.

4.1.4 Mesh convergence study and computational cost

For all the 3 test cases above, the mesh used consisted in 16×50 cell elements uniformly spaced along the cone surface, and with a Robert's stretching transformation [36, pp. 335-336] along the direction normal to the cone surface, so as to refine the mesh on the boundary layer. Mesh convergence studies were conducted, which confirmed this mesh was sufficient. The results were relegated to the appendix, namely figure B.2. They show that an increase to 36×75 cells, yields a very similar temperature profile with the exception of the shock region at around $0.02 < y_{\text{normal}}$ [m] < 0.025. The shock is resolved more sharply but the boundary layer presents negligible differences. This was verified for all the 3 cases. Furthermore, the mass fractions profiles (not shown on the appendix) show very small changes.

All the simulations on this thesis were carried out using a computer at IPFN with a Intel(R) Xeon(R) CPU X5460 @ 3.16GHz. The time required for each simulation is presented on table 4.2.

	Isothermal Wall	SEB, 10^0	SEB, 20^0
16×50 cells	3 hrs	3 hrs	7 hrs
36×75 cells	10 hrs	10.5 hrs	24 hrs

Table 4.2: Computational cost of the main simulations carried out for sharp cones.

4.2 Electre Probe

Electre is a standardized spherical-conical blunt body representing a re-entry capsule. It has been used in ground experiments for obtaining wind tunnel data for comparison with flight and numerical results. It has become a reference model to study non-equilibrium hypersonic flow over blunt bodies [32], [37] and [38]. In this section, SPARK results are compared with computational results and experimental data from Barbato et al., 1994 [25], Muylaert et al., 1998 [32] and Viviani et al., 2009 [38] as shown on roadmap 4.14. The experimental data comes from ground facilities namely the HEG tube and the F4 hot shot.

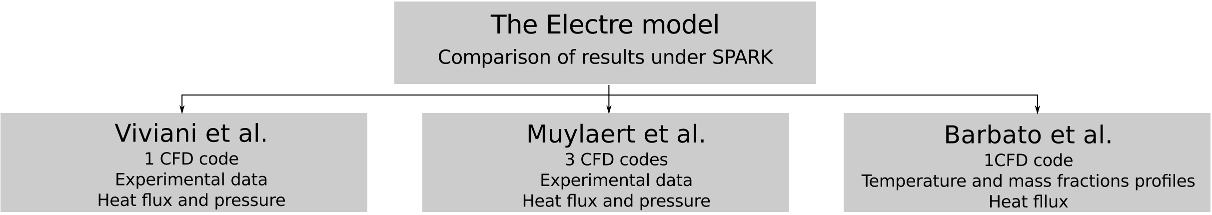

Figure 4.14: RoadMap for the Electre test cases.

Electre is completely defined by 3 parameters: a length of 0.4 m, a semi-aperture cone angle of $4.6°$ and a nose radius of 0.035 m. Figure 4.15 shows the actual probe along with a computational mesh used for SPARK simulations. On the left figure, the instrumentation allows for the measurement of the desired parameters such as heat flux and pressure. On the right figure, notice the higher density of cells close to the surface needed for good resolution of the flow features. The upstream conditions for the simulations are summarized on table 4.3.

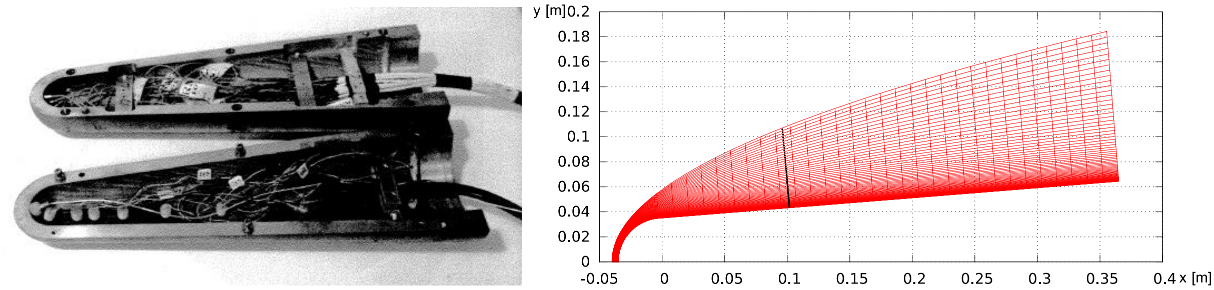

(a) Photograph of the Electre Model with Instrumentation, from [37]

(b) Mesh for SPARK simulations. Example for 100X65 Cells. The discrete black points normal to the surface at x = 0.1 m represent the location of the profiles(temperature and mass fractions) of some results presented next.

Figure 4.15: Electre Probe's model and Computational Mesh

	T_∞ [K]	ρ_∞ [kg m^{-3}]	P_∞ [Pa]	V_∞[m/s]	c_{N_2} [-]	c_{O_2} [-]	c_N [-]	c_O [-]	c_{NO} [-]	T_{wall} [K]
Viviani et al.	790	16.40E-4	430	5953	0.7544	0.0367	0	0.1817	0.0272	300
Muylaert et al.	795	5.450E-4	-	4930	0.7729	0.2376	0	0	0	300
Barbato et al.	$\frac{T_\infty=766.38}{T_{V_\infty}=3930}$	20.17E-4	-	5953	0.7544	0.0367	0	0.1817	0.0272	343/800

Table 4.3: Upstream conditions for the 3 test cases from different authors over the Electre probe.

4.2.1 Viviani et al.

The analysis of figures 4.16 show that SPARK underpredicts the heat flux for both the non catalytic and fully catalytic simulations. Because on the noncatalytic case there is no diffusion, the discrepancy cannot be attributed to the catalytic model implemented. This difference reaches 40% at the nose of Electre and over 42% at $\frac{x}{L}$ = 1.

For the fully catalytic simulations the heat flux increases on both curves but the errors rise to 90% at the nose and roughly 50% at the back, evidencing an additional error introduced due to the catalytic model implemented on SPARK. Only the break-up of the total heat flux onto its constituent terms (i.e., convective(translational) and diffusive fluxes) would allow proving this. Furthermore, the experimental data shows that SPARK predicts relatively well the heat flux on the spherical portion of Electre but not along its slope. Despite to this, the results have a very good qualitative agreement as they appear to just being shifted from one to another.

On the other hand the SPARK simulations were ran with thermal equilibrium while Viviani at al. assumed a two-temperature model. Also different was the procedure to compute the diffusion coefficient of all species D_i. However, it is believed the results would not have suffered any noticeable difference had the models been the same.

It is relevant to analyse the pressure coefficient on the surface. There is a perfect match with the computational results of Viviani et al. and the experimental data. The fact that the pressure matches perfectly but not the heat flux is not contradictory because the fluid flow pressure is a variable which is predominantly governed by the momentum equation and only slightly affected by thermodynamics [1, p. 607]. The result thus verifies the "correctness" of SPARK on this regard.

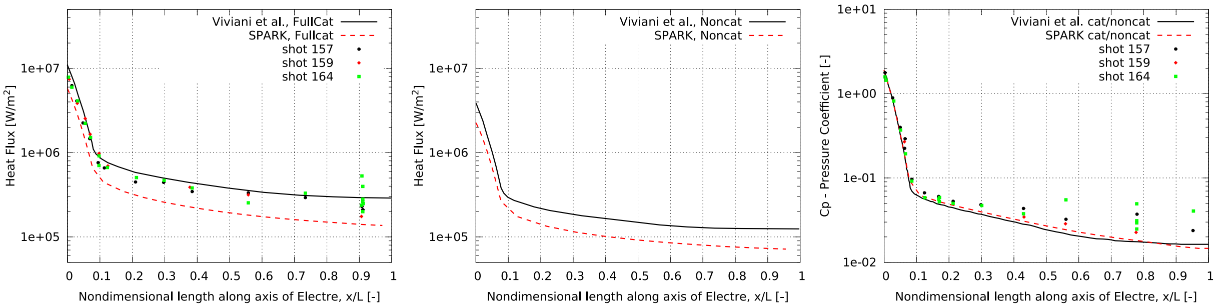

(a) Total Heat Flux onto Electre - Fully Catalytic

(b) Total Heat Flux onto Electre - Non Catalytic

(c) Pressure coefficient on the surface of Electre. $C_p = \frac{p-p_\infty}{\frac{1}{2}\rho_\infty V_\infty^2}$

Figure 4.16: Comparison between available results from Viviani et al. [38] and corresponding SPARK simulations. Heat flux and pressure coefficient as a function of the nondimensionalized length along the axis of Electre. The "shots" correspond to experimental data.

4.2.2 Muylaert et al.

In this case Muylaert et al. [32] presents results from 3 different CFD codes. Some of the features employed by each of these codes are different; they use different chemical schemes, different methods to compute the diffusion coefficient D_i and even the overall CFD Navier-Stokes (NS) scheme is not the same. It will suffice to say that the one closest to SPARK in these simulations is CIRA.

Despite this diversity, all the 3 codes agree to a large extent for the full catalytic simulation, figure 4.17, while SPARK underpredicts those curves along the entire surface. At x = 0.4 m the difference to the CIRA curve is about 50%. For the non-catalytic case there is less agreement between CIRA and ESTEC but still SPARK shows a heat flux clearly lower than these two. The difference to the CIRA heat flux is again roughly 50% at x = 0.4 m. In either case the SPARK results are closest to the CIRA curves which conforms with both codes sharing most of their features (i.e., they share the NS scheme, the chemical scheme and more).

From figure (c), the agreement of the pressure coefficient is even more pronounced as the curves are almost indistinguishable from each other and the experimental results. Obviously the previous comment applies here.

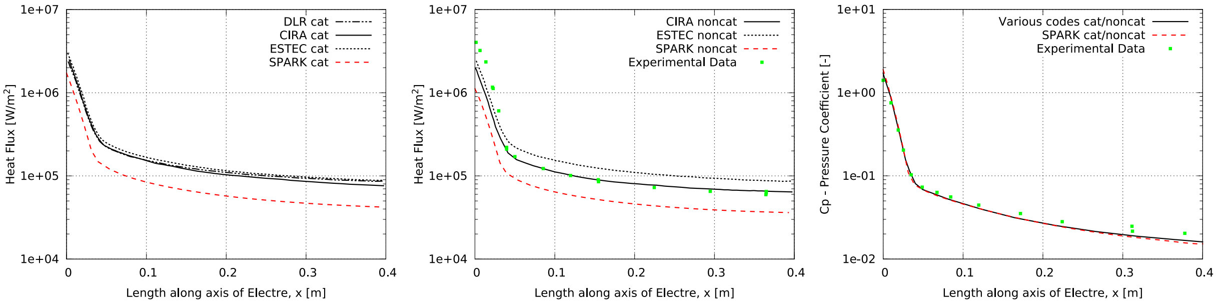

(a) Total Heat Flux onto Electre - Fully Catalytic

(b) Total Heat Flux onto Electre - Non Catalytic

(c) Pressure coefficient on the surface of Electre. $C_p = \frac{p-p_\infty}{\frac{1}{2}\rho_\infty V_\infty^2}$

Figure 4.17: Comparison between available results from Muylaert et al. [32] and corresponding SPARK simulations. Heat flux and pressure coefficient as a function of the length along the axis of Electre. DLR, CIRA and ESTEC are independent CFD codes.

4.2.3 Barbato et al.

Two different cases concerning two wall temperatures, namely T_w = 343 K and T_w = 800 K are reproduced after Barbato et al., 1994 [25]. The upstream conditions are on table 4.3.

There was an effort to run the SPARK simulations on the same grounds as the results that are being reproduced. The same chemical set (Blottner [34]) and chemical vibrational coupling model are used. There was no reference to the evaluation of thermodynamic properties or the diffusion coefficient model. However, the approach followed by Barbato et al. to model catalycity is the equilibrium wall approximation which is different from the implementation on SPARK. The importance of this is addressed when relevant.

Case: $T_\mathrm{w} = 343K$

For the simulation with T_w = 343 K as boundary condition, the compared results are the temperature profile and the mass fraction profiles of all species along the normal to the Electre wall at x = 0.1 m.

The discrete black points on figure 4.15 illustrate the location of these profiles. For all profiles the Barbato et al. figures (in digital format) from which the results were extracted had low quality. Hence it is possible that some curves are presented with some corruption. Furthermore, it was not possible to obtain temperature and mass fraction points on the absolute proximity of the wall, also because of this poor digital quality.

From a broad perspective, by inspecting figures 4.18 and 4.19 we may immediately find that there is a good qualitative agreement and a decent quantitative agreement between the current SPARK and Barbato et al. results. For temperature, SPARK captures the same ”S” like shape near the wall but overpredicts that local maximum by 8%. The profile seems to be shifted to the right. The low quality of the figures from which this data was extracted might have introduced this error. Furthermore, in contrast with the temperature profiles normal to the sharp-cones (as analysed previously on section 4.1) the current temperature along the normal of Electre depends on the catalycity (i.e., on γ) of the surface, as shown on figure B.4 of the appendix. For γ = 0.01 the ”S” shape fades due to the decrease of the local maximum near the wall. This shows that the curves on (a) have already embedded on them the effects of wall catalycity.

The discrepancies for $y_{\text{normal}} > 2\,\text{cm}$ are considered not to be born out of the catalytic model.

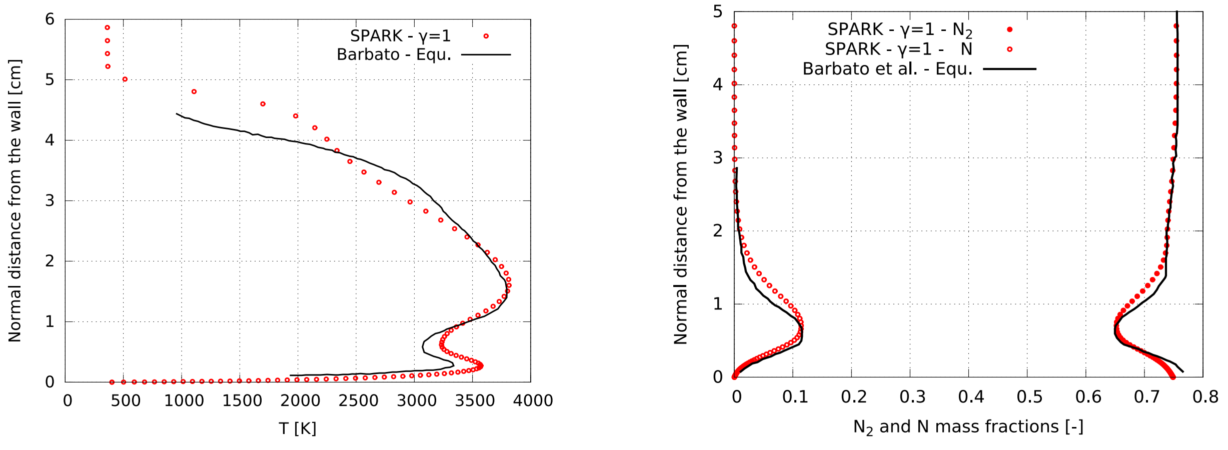

(a) Temperature Profile

(b) Mass Fraction of species N_2 and N.

Figure 4.18: Temperature and N_2 and N mass fractions along the normal to Electre's wall at x = $0.1\,\text{m}$ for $T_{\text{w}} = 343K$. Comparison of current results under SPARK with Barbato et al. [25]. Equ. on the legend stands for equilibrium wall boundary condition.

For the mass fraction results, the agreement is very good with the exception of NO. Notice however that there are no data points for the profiles under Barbato et al. at the immediate vicinity at the wall because of the low quality of the digital figures from which the data was extracted. A comparison near the wall, would be most relevant, as the slope of the mass fraction there determines the heat into Electre. Still the slopes seem to be identical for N_2, N, O_2 and O.

The discrepancies are the greatest for NO, specially near the wall where the two curves have opposite trends. The explanation is guaranteed to come from the equilibrium wall boundary condition employed by Barbato et al.

As discussed on section 2.5.1, the equilibrium wall model consists in simply setting the composition at the wall to the equilibrium composition that would exist at the temperature and pressure of that point on the wall:

$$c_{i,\mathrm{w}} = c_{i,\mathrm{w}}(p_{\mathrm{w}}, T_{\mathrm{w}})$$

In practice it works quite well for air environments and provides very similar results compared with the full catalytic (implemented in SPARK) approach [39, p. 132]; so similar indeed that the terms *equilibrium wall* and *fully catalytic* are often used interchangeably [27, p. 181]. Thus using the results of Barbato et al. for the verification of SPARK's implementation is a valid approach.

Despite this, the NO profiles don't match near the wall because in SPARK there is no NO production or consumption ($\dot{\omega}_{\mathrm{NO,w}} = 0$). Thus the slope of NO mass fraction on the wall is always zero[2], $\dot{\omega}_{\mathrm{NO,w}} = 0 \Rightarrow \left(\frac{\partial c_{\mathrm{NO}}}{\partial n}\right)_{\mathrm{w}} = 0$. The surface can be regarded as being indifferent to NO allowing the value $c_{\mathrm{NO,w}}$ to be decided by the gas flow. In contrast the equilibrium wall condition used by Barbato et al. explicitly sets $c_{\mathrm{NO,w}} = c_{\mathrm{NO}}(p_{\mathrm{w}}, T_{\mathrm{w}})$ which requires the c_{NO} profile to accommodate to the equilibrium value dictated by the wall temperature and local pressure. In this case the value is lower than would otherwise be if the surface didn't interfere in the composition of NO directly, as happened for the fully catalytic case in SPARK.

The intention of the previous discussion was to demonstrate that the differences on the NO profiles were expected and not the evidence of an incorrect implementation of catalycity in SPARK.

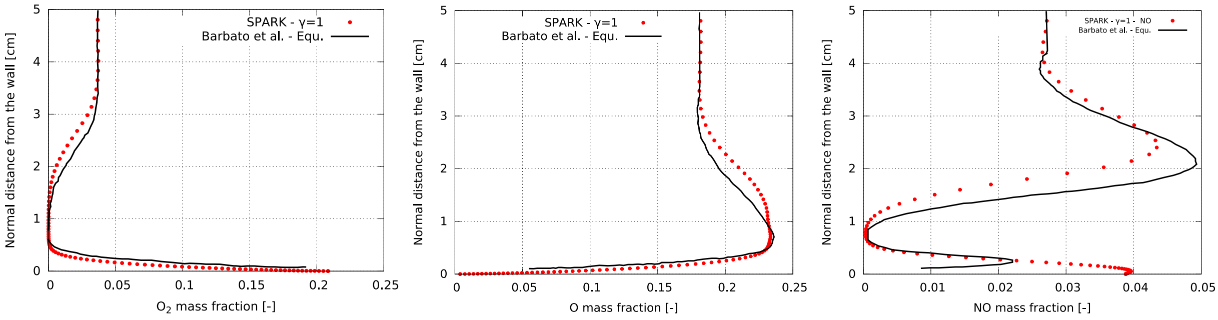

(a) Mass fraction of O_2 (b) Mass fraction of O (c) Mass fraction of NO

Figure 4.19: Mass fractions of species O_2, O and NO along the normal to Electre's wall at x = 0.1 m for $T_{\mathrm{w}} = 343K$. Comparison of current results under SPARK with Barbato et al. [25]. Equ. on the legend stands for equilibrium wall boundary condition.

Case: $T_{\mathrm{w}} = 800K$

For the second simulation where $T_{\mathrm{w}} = 800$ K, the various forms of heat flux along the Electre surface are compared on the 5 graphs of figure 4.20. Overall, the agreement of the results is equivalent to the previous cases for Viviani et al. and Muyalert et al. on figures 4.16 and 4.17 respectively. Unlike those cases however, the various contributions of the heat flux are presently discriminated for the full-catalycity simulation.

The non-catalytic simulation (only the total heat flux is shown) for which no heat through diffusion occurs, already exhibits a disagreement, but both curves are well within the same order of magnitude. SPARK

---

[2] This is not clear from figure 4.19 but it becomes evident when zooming in near the wall.

again seems to underpredict Barbato's results. In the nose the heat flux is 40% lower and at x = 0.4 m 48% lower.

As expected the heat flux increases, on both curves, for the full catalytic simulation. This is almost entirely due to the emergence of gradients of the mass fractions of the various species, which trough diffusion contribute with heat by an amount similar to the heat flux coming from temperature gradients (i.e., translational flux). Furthermore, vibrational heat flux is one order of magnitude lower than the other modes, not because of the gradient of vibrational temperature, but due to the very low conductive coefficient for vibration k_{vib}, about 1 order of magnitude lower than k_{trans} for this temperatures [40].

There is a greater mismatch for the diffusive fluxes in figure (e) than for the translation heat fluxes at (c). The translational heat flux under SPARK is 25% lower at the nose and 31% lower at x = 0.4 m while the difference for the diffusion fluxes is also of 25% at the nose but exceeds 50% at x = 0.4 m. This difference between the curves increases along the surface of Electre and may in part be explained by Barbato et al. using the equilibrium wall and not the full catalytic conditions. As seen for T_w = 343 K, the profiles of c_NO are opposite in direction near the wall. SPARK results have zero slope and thus there is no diffusion heat flux from NO. In contrast there is a positive gradient of NO molecules at the wall for the curve under Barbato et al. which results in an additional term of heat flux:

$$q_{\text{diff}_\text{NO}} = \left(h_\text{NO} \rho D_\text{NO} \frac{\partial c_\text{NO}}{\partial n} \right)_\text{w} \tag{4.1}$$

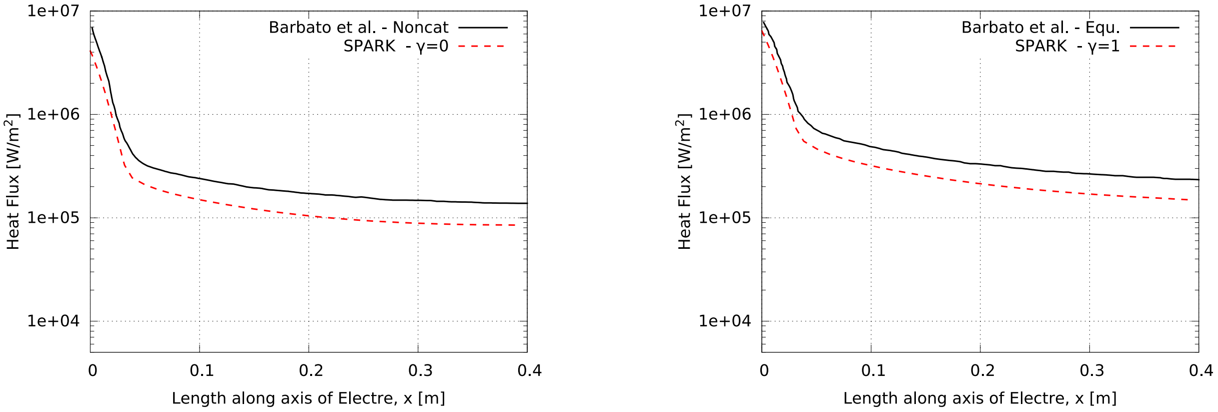

(a) Non catalytic - Total heat flux

(b) Full catalytic - Total heat flux

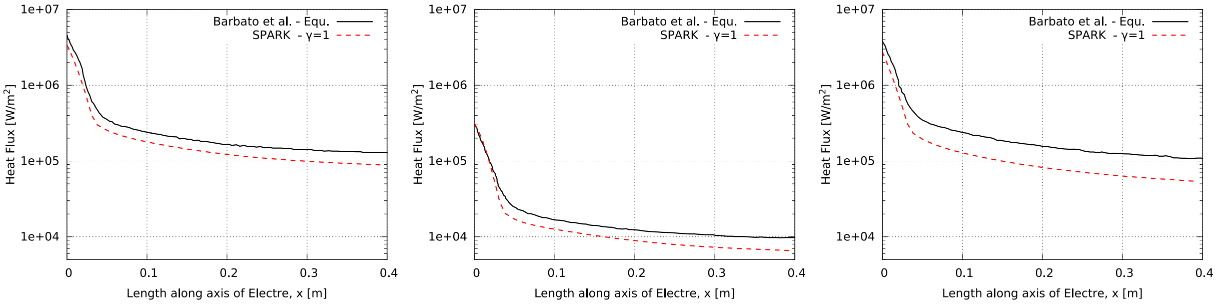

(c) Full catalytic - Translational flux

(d) Full catalytic - Vibrational flux

(e) Full catalytic - Diffusive flux

Figure 4.20: Comparison between available results from Barbato et al. [25] and corresponding SPARK simulations for T_w = 800 K. Heat flux as a function of the length along the axis of Electre.

4.2.4 Mesh, convergence study and computational cost

While not particularly relevant for the study of catalycity, it remains important to comment some aspects of the CFD simulations.

Because the mesh represents the discretized space where the Navier-Stokes(NS) equations are solved, it must be big enough to capture the shock wave, otherwise we would be setting a non-physical simulation whereby the space dimensions where the NS equations are being solved is incompatible with the dimensions of the phenomenon which it produces.

Because the position and shape of the shock-wave are not known a priori but only after the simulation has ran its course, the mesh dimensions could be overestimated to ensure the inclusion of the shock-wave as in figure 4.21 by the red solid line. Although that would be effective it would not be efficient because would inevitably result in higher computational cost due to more cells being needed to cover the area before the shock, or less accuracy by using the same cells to cover a greater area.

The workaround consisted in using the results of Billig [41], who presents correlations for the shape of shock waves around blunt-bodies. These correlations were based on experimental data, but have a very good agreement with numerical calculations [42], at least for non-reactive flows. Billig presents equation (4.2), giving the shape as a function of the bodies' dimensions and the incoming Mach Number M_∞. For Electre the dimensions were the nose radius (R = 0.035 m) and the semi aperture cone angle (θ = 4.6°). Also, on correlation (4.2) variables x and y represent the coordinates of the shock-wave, and the rest of the nomenclature is illustrated on figure 4.21.

$$\begin{cases} x = R + \delta - R_c \cot^2\theta \left[\left(1 + \dfrac{y^2 \tan^2\theta}{R_c^2} \right)^{1/2} - 1 \right] \\ \text{Where } \delta,\ R_c = \text{f}(M_\infty, \text{R}) \end{cases} \tag{4.2}$$

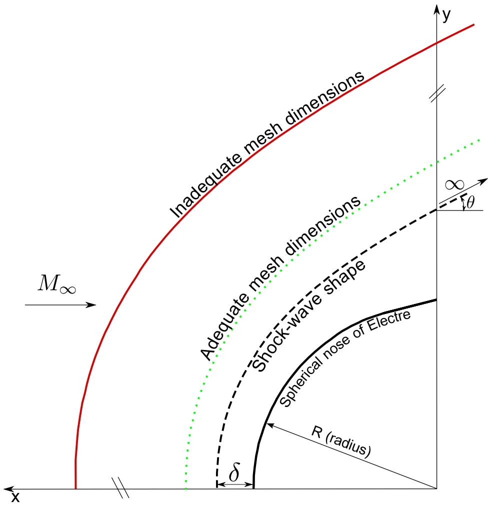

Figure 4.21: Illustration of the formation of a shock wave in front of Electre, and the outer limits of two computational meshes that follow the shock's shape.

Hence the mesh for Electre used in SPARK allows for a very judicious use of computational power. Revisiting the computational mesh of figure 4.15, Billig's model allows finding out how short can the mesh dimensions be at the nose (y = 0 m) and how lengthy, in terms of normal distance from the surface, it needs to be at the "rear". Lastly, similar to the cone case, the cells height grows with the distance from the wall of the probe via the Robert's stretching [36, pp. 335-336].

The convergence studies performed to access the independence of the results from the mesh are present on figure B.3 of the appendix. The corresponding computational times are given on table 4.4:

	50X35 cells	70X50 cells	90X65 cells	100X65 cells
Viviani et al.	19 hrs	44 hrs		
Muylaert et al.	27 hrs	45 hrs	92 hrs	
Barbato et al.	24 hrs			120 hrs

Table 4.4: Computational cost of the main simulations carried out for the Electre probe.

4.3 Temperature varying SRE, $\gamma = \gamma(T)$

The objective of the present section is to verify the implementation of the temperature dependent recombination coefficients, $\gamma = \gamma(T)$. In contrast with the other V&V sections considered above, SPARK results will not be compared with other codes. From the 2 studies found on SRE catalicity using the same models, Godart et al., 1996 [43] does not present the free-stream conditions which prevents the reproduction of results and Barbato et al., 1994 [25] runs the simulations for an isothermal case of T_{wall} = 1500 K, which caps the purpose of temperature dependent recombination coefficient models.

Consequently, the models from Scott, Zoby et al. and Stewart et al. presented on section 2.5.1 were tested for the sharp cone, SEB, semi-angle = 20° case, where the free-stream conditions remained the same[3]. A SEB condition was chosen so as to allow for the wall temperature to vary along the surface; on contrary for an isothermal wall, the models would result on a fixed γ along the surface evaluated at the given temperature. The particular case of semi-angle = 20° was preferred because the greater dissociation levels allows richer results.

A code-to-code comparison is desirable, but not indispensable as there are other procedures used to verify the code "correctness" [44, ch. 5]; in this case, without benchmark solutions, the discussion will be centred around the consistency of the results.

The results analysed are the mass fractions on the surface of the cone presented on figure 4.23. The reader is referred to figures B.5 and B.6 of the appendix for a better appreciation of the results that follow. The black dots on figure B.5 illustrate the location where temperature, mass fraction and reaction efficiency are accessed.

Figure 4.23 shows the mass fractions of N, O and NO on the surface of the cone as a function of its axial length. The results for N_2 and O_2 are on the appendix B.3. For each species there are 5 curves: 3 for the models after Scott, 1980 [9] Zoby et al., 1984 [10] and Stewart et al., 1987 [33] and the other 2

---

[3] The mesh used was, however, finer. It had 40 cells, instead of 14, along the surface of the cone, since in this case the interest were plots along the surface of the cone. The mesh can be seen on figure B.5 of the appendix.

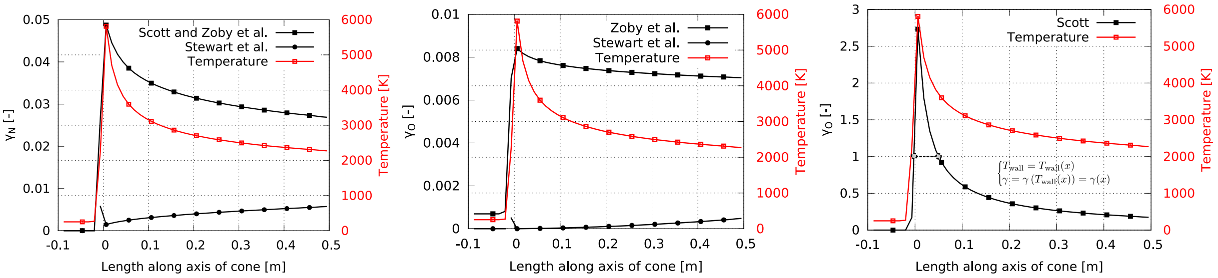

(a) Efficiency (γ_N) for catalytic reaction N + N ⟶ N_2

(b) Efficiency (γ_O) for catalytic reaction O + O ⟶ O_2

(c) Efficiency (γ_O) for catalytic reaction O + O ⟶ O_2

Figure 4.22: Recombination coefficients/reaction efficiency (γ) on the surface of the cone as a function of its axial length for the 3 models implemented in SPARK applied on the same case: Sharp Cone, Semi-angle=20^o, SEB.. The temperature is the same for all plots. Ranges of left hand y-axis are not the same.

reporting the non-catalytic and fully-catalytic conditions for a frame of reference.

The first conclusion is that the curves of the 3 models are always in between the curves for γ = 0 and γ = 1. In particular, the mass fraction of the dissociated species (N, O and NO) are, for each constant x station, always lower and greater than the non-catalytic and fully catalytic curves respectively. This single-handedly supports the correct implementation of the SRE model introduced. Because the catalytic coefficient is the ratio of the incoming atomic species that recombine, catalycity (i.e., the γ) acts as a sink for dissociated species. The higher the γ the less atomic species will be present at the wall with the inverse occurring for low γ. Accordingly, considering non-cataliclity and full catalicity constitute the lower and upper bounds for γ, they also represent the greatest and lowest possible amounts of dissociated species at the wall respectively.

For the analysis of the individual results of N, O and NO, figures 4.22 are useful. They show how, for each model, the recombination coefficients varied along the cone surface. The temperature profile on these figures was mostly independent on the value of catalycity used and only one is plotted.

- Curves for $(c_{\text{N}})_{\text{w}}$

  For the initial portion of the cone surface, Stewart's curve follows the ceiling profile for γ = 0 owing to the very low catalycity verified, $\gamma_{\text{N}} < 0.004$. As the temperature decreases along the surface, the recombination coefficient increases, favouring a depletion of N atoms at the wall that translates on the curve bending away from the γ = 0 and towards the γ = 1 curves. The variation of $\gamma_{\text{N}}(x)$ is the same on the Zoby et al. and Scott models, while the mass fraction of N is different for simulations using either model. This is not inconsistent as the mass fraction values, even at the wall, are not just dependent on the catalycity of γ_{N} but also on the homogeneous reactions from the gas phase.

- Curves for $(c_{\text{O}})_{\text{w}}$

  All curves have a monotonic behaviour except Stewart's, whose O mass fraction initially increases along the surface and then, after reaching a plateau, starts decreasing. The mechanism is again the increase of γ_{N} along the surface. Albeit small, this increase is sufficient given the non-linear effect of the recombination coefficient. There is however always more O than for the Zoby et al. model, which agrees with the magnitude of corresponding coefficients. Owing to the very high recombination coefficient along the cone wall, Scott's model results in much less amount of O, with the profile approaching the fully-catalytic case. In particular, we can notice on the initial portion corresponding to $x < 0.005\,\text{m}$ that the recombination efficiency is extrapolated from the model to be as high as γ_{O} = 2.7. As discussed on the introductory chapters, this is non-physical and SPARK overrides the value to γ_{O} = 1.

- Curves for $(c_{\mathrm{NO}})_{\mathsf{w}}$
  Lastly for NO, all the profiles vary linearly along the cone surface. Remember that there is no production of NO directly from catalycity, i.e the reaction N $+$ O $\longrightarrow$ NO is not modelled. The coefficient on the legend of figures 4.23 refers merely to $\gamma_{\mathrm{N}} = \gamma_{\mathrm{O}} = \gamma$. This means the values for $(c_{\mathrm{NO}})_{\mathsf{w}}$ are an effect of the gas-phase reactions, most likely linked with the homogeneous reaction O_2 $+$ N $\longleftrightarrow$ NO $+$ O. This explains the small amounts of N (for all models), as this species is consumed for the creation of NO. Furthermore, Scott's model results in much less NO, which conforms with the already seen lower quantity of N and O, essential for the creation of NO.

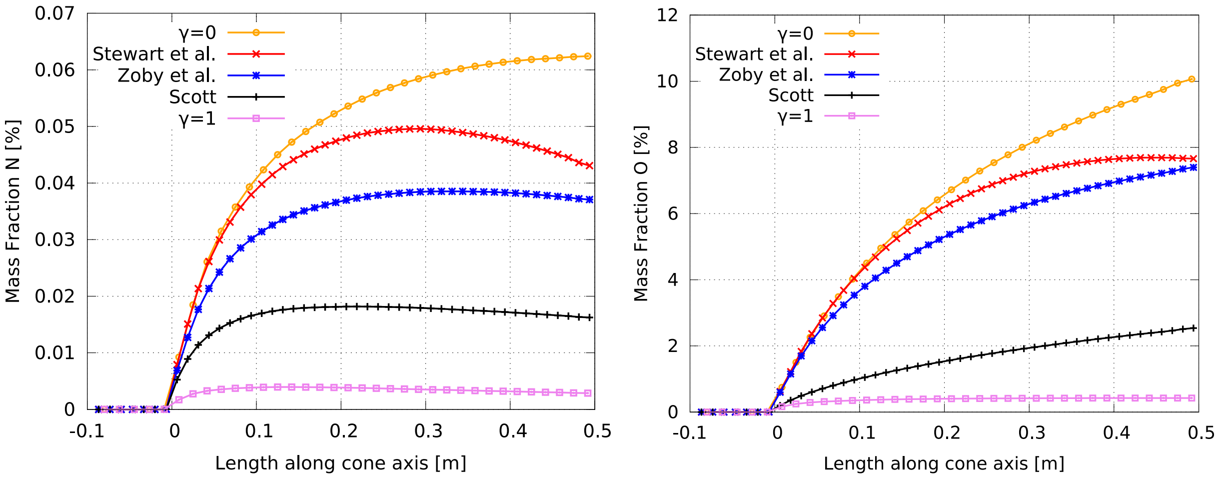

(a) N mass fraction on the surface of the cone, $(c_{\mathrm{N}})_{\mathrm{w}}$ (b) O mass fraction on the surface of the cone, $(c_{\mathrm{O}})_{\mathrm{w}}$

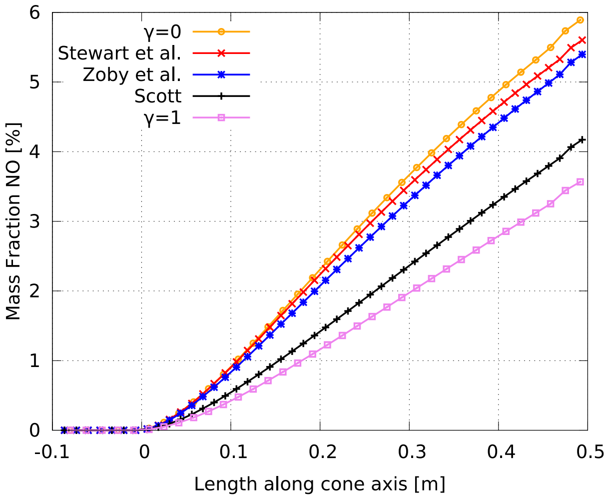

(c) NO mass fraction on the surface of the cone, $(c_{\mathrm{NO}})_{\mathrm{w}}$

Figure 4.23: Mass fraction of the dissociated species N, O and NO on the surface of the cone as a function of its axial length for several models applied on the same case: Sharp Cone, Semi-angle=20^o, SEB. Ranges of y-axis are not the same. $\gamma_{\mathrm{N}} = \gamma_{\mathrm{O}} = \gamma$.

4.4 Self assessment of the implementation

In the present chapter a great number of computational results under SPARK have been compared with other CFD codes and experimental data. The original purpose was to verify the ”correctness” of the implementation of catalycity in SPARK. Is SPARK now able to credibly model re-entry Earth flows where catalycity is expected to play a role?

Overall, it is clear that on the qualitative level the results have a very good agreement. They present the same trends with the same slopes often just shifted. On the quantitative side however the differences to the other results are in some cases only just slightly beyond reasonable doubt.

The author believes a likely explanation can simply be the evaluation of Δn which from chapter 3 corresponds to the distance between the first cell node and the wall:

The metric terms of the transformation

As presented on appendix A, the discretization of the Navier-Stokes (NS) by SPARK includes a transformation of coordinates from the physical plane (x, y) to a computational domain (ξ, η):

$$x = x(\xi, \eta), \qquad y = y(\xi, \eta)$$

Transforming the equations has certain advantages but effectively changes their nature and must now include metric terms as described on the appendix.

The boundary conditions also change because of this transformation. The equations are the same but expressed in different coordinates. For example, on Fick's law of diffusion of (2.20) the gradient can no longer be described in terms of (x, y) because the Navier-Stokes are being solved in another domain.

$$\mathbf{j}_i = -\rho D_i \nabla c_i \qquad \text{(2.20 revisited)}$$

$$\Leftrightarrow \quad \mathbf{j}_i = -\rho D_i \nabla c_i = -\rho D_i \xcancel{\left(\frac{\partial c_i}{\partial x}, \frac{\partial c_i}{\partial y}\right)}$$

Transforming the wall mass balance to the new computational coordinates begins with:

$$j_{i,\text{into the wall}} = -\rho D_i \nabla c_i \cdot \vec{n} = -\rho D_i \left(\frac{\partial c_i}{\partial x}, \frac{\partial c_i}{\partial y}\right) \cdot (n_x, n_y) = -\rho D_i \left(\frac{\partial c_i}{\partial x} n_x + \frac{\partial c_i}{\partial y} n_y\right) \qquad (4.3)$$

Where $\vec{n}$ is a vector normal to the wall and n_x, n_y are its components.

Through the transformation, the derivatives with respect to x and y are converted to ξ, η, via the relations [45, ch. 5]:

$$\begin{aligned} \frac{\partial c_i}{\partial x} &= \frac{1}{J}\left[\frac{\partial c_i}{\partial \xi} y_\eta - \frac{\partial c_i}{\partial \eta} y_\xi\right] \\ \frac{\partial c_i}{\partial y} &= \frac{1}{J}\left[\frac{\partial c_i}{\partial \eta} x_\xi - \frac{\partial c_i}{\partial \xi} x_\eta\right] \end{aligned} \qquad (4.4)$$

Where the ξ_x, ξ_y, η_x and η_y are known as metric terms with the subscripts corresponding to differentiation and J is the Jacobian of the transformation.

Introducing (4.4) into (4.3) the mass flux can be expressed as:

$$j_{i,\text{into the wall}} = -\rho D_i \frac{1}{J}\left[\frac{\partial c_i}{\partial \xi}(y_\eta n_x - x_\eta n_y) + \frac{\partial c_i}{\partial \eta}(x_\xi n_y - y_\xi n_x)\right] \tag{4.5}$$

Now the mass flux is expressed in terms of the computational variables ξ and η.

The next step is to specify the wall normal $\vec{n}$ in terms of the computational variables. Without loss of generality it is assumed that the wall corresponds to a constant ξ line on the computational domain. In that case the wall normal is given by:

$$\begin{aligned} n_x &= \frac{-y_\eta}{\sqrt{x_\eta^2 + y_\eta^2}} \\ n_y &= \frac{x_\eta}{\sqrt{x_\eta^2 + y_\eta^2}} \end{aligned} \tag{4.6}$$

Inserting (4.6) into (4.5) eventually leads to [4]:

$$j_{i,\text{into the wall}} = \left(\rho D_i \frac{\partial c_i}{\partial \xi} \boxed{\frac{1}{J}\left(\frac{y_\eta^2}{\sqrt{x_\eta^2 + y_\eta^2}} + \frac{x_\eta^2}{\sqrt{x_\eta^2 + y_\eta^2}}\right)}\right)_{\text{w}} \tag{4.7}$$

In contrast, the original wall mass balance equation was developed into (2.21):

$$(j_i)_{\text{w, into the wall}} = -(j_i)_{\text{w}} = \left(\rho D_i \frac{\partial c_i}{\partial n}\right)_{\text{w}} \tag{2.21 revisited}$$

The expressions are similar. While n was the coordinate normal to the wall, now ξ is the coordinate normal to the wall. However, the boundary condition must now incorporate the boxed term embodying the effects of the coordinate transformation.

From the point of view of the implementation onto SPARK the discretization originally given by (3.6) has in fact a more complex nature given by (4.8).

$$\left(\frac{\partial c_i}{\partial n}\right)_{\text{w}} = \frac{(c_i)_{\text{i}} - (c_i)_{\text{w}}}{\Delta n} \tag{3.6 revisited}$$

$$\begin{aligned} &\left(\frac{\partial c_i}{\partial \xi}\right)_{\text{w}} = \frac{(c_i)_{\text{i}} - (c_i)_{\text{w}}}{\Delta \xi}\left(\boxed{\frac{1}{J}\left(\frac{y_\eta^2}{\sqrt{x_\eta^2 + y_\eta^2}} + \frac{x_\eta^2}{\sqrt{x_\eta^2 + y_\eta^2}}\right)}\right)_{\text{w}} \Leftrightarrow \\ &\left(\frac{\partial c_i}{\partial \xi}\right)_{\text{w}} = \frac{(c_i)_{\text{i}} - (c_i)_{\text{w}}}{(\Delta \xi)'} \qquad \text{Where: } \left[(\Delta\xi)'\right]^{-1} = \frac{1}{\Delta \xi}\left(\frac{1}{J}\left(\frac{y_\eta^2}{\sqrt{x_\eta^2 + y_\eta^2}} + \frac{x_\eta^2}{\sqrt{x_\eta^2 + y_\eta^2}}\right)\right)_{\text{w}} \end{aligned} \tag{4.8}$$

Where $(\Delta\xi)'$ can be viewed as an effective distance to the wall.

The implementation into SPARK does indeed take the metric terms into consideration, i.e., it evaluates the "effective" Δn through an expression similar to (4.8). The objective with this derivations and this section is then to ask whether or not the term is correctly implemented in SPARK, as the author feels that

---

[4] This is actually a particular case, but which is most useful to illustrate the point. It corresponds to an orthogonal transformation.

a complete understanding of the matter is paramount to increase the confidence on the implementation. This can be accomplished by running certain very simple test cases that evidence this Δn aspect or more importantly by analysing and comparing the theoretical derivations in other aerothermodynamics CFD codes that discretize the Navier-Stokes with a coordinate transformation.

Chapter 5

The Finite Rate Surface Chemistry (FRSC) model

As illustrated on figure 5.1, this chapter has 3 sections. The first section consists in a brief overview of the theoretical formulation of the FRSC model; as commented along the text, this formulation was developed by Marschall and MacLean, 2011 [20] and is used by several codes [11, 21]. The second section is a concise description on how to readily update SPARK from the SRE to the FRSC model. As noted before, this thesis work did not actually include this update and only the strategy to do it is described. Lastly, the third section concerns the stand alone code, which can be regarded as a prerequisite for a future full implementation of the FRSC model in SPARK; the results are matched with the implementation by MacLean et al. [20].

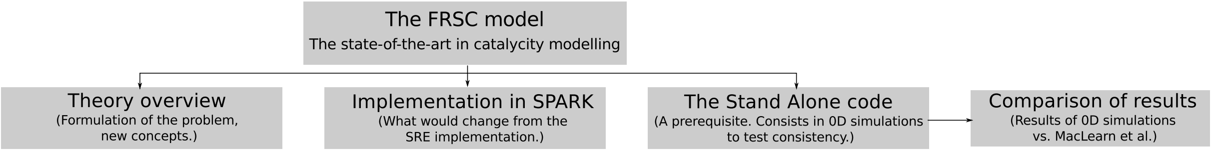

Figure 5.1: Road Map for the chapter.

5.1 Theoretical Overview

The next step towards a state-of-the-art modelling of catalycity is a general finite-rate surface chemistry (FRSC) model. The improvement consists in abandoning the imposed surface efficiency γ, that attempts to macroscopically model catalycity and start taking into account the microscopic processes responsible, on a more basic level, for catalycity thus providing a physically justified model.

In short, a finite-rate surface chemistry model (FRSC) tries to emulate for the heterogeneous reactions the mechanisms and procedures used for homogeneous gas phase reactions. This is done by firstly recognizing pseudo-species specific to a surface that enable fundamental pathways involved and secondly by allowing competing kinetic reactions taking place within this surface relating both the gas phase species and these pseudo-species.

The model consists in 3 environments that coexist at the gas/surface interface: the gas, surface and bulk environment. Each of these is comprised of one or more phases which represent physically distinct regions. Here, for clarity, we will assume just one phase for each environment.

The gas phase comprehends all the original gas species and any eventual species injected in the gas by the ablation of the bulk, i.e. by the consumption of the surface itself.

The surface phase has one or more sets of actives sites which are the central piece of this microscopic description since it is on this sites that the chemical reactions take place. Each of this sets of active sites have a site density Φ_{na}, and are associated with a set of chemical species K_{na} where na is the index of the set. The chemical species existing on these sites are either adsorbed atoms/molecules (e.g., O(s), N(s), CO(s), etc.) or empty sites denoted E(s).

With the bulk phase is possible to model surface participating reactions like sublimation and oxidation that take place during ablation.

In this context, species on the traditional sense (e.g., atomic nitrogen or carbon dioxide) are considered different species if in the gas phase (N and CO), in the surface phase (N(s) or CO(s)) or in the bulk phase (N(b) or CO(b)).

Examples of such surface reactions are:

$$\begin{array}{ll} \text{Adsorption:} & \mathrm{A} + \mathrm{(s)} \rightleftharpoons \mathrm{A(s)} \\ \text{Eley-Rideal (ER):} & \mathrm{B} + \mathrm{A(s)} \rightleftharpoons \mathrm{AB} + \mathrm{(s)} \\ \text{Langmuir-Hinshelwood (LH):} & \mathrm{A(s)} + \mathrm{B(s)} \rightleftharpoons \mathrm{AB} + 2\,\mathrm{(s)} \\ \text{Sublimation:} & \mathrm{(s)} + \mathrm{A(b)} \rightleftharpoons \mathrm{A} + \mathrm{(s)} \end{array} \tag{5.1}$$

All the reactions are written in the form:

$$\sum_{i=1} \nu_{ir}^{'} A_i \longleftrightarrow \sum_{i=1} \nu_{ir}^{''} A_i \tag{5.2}$$

Where A_i is the chemical symbol and $\nu_i^{'}$ and $\nu_i^{''}$ are the stoichiometric coefficients for species i. As the examples above show, each reaction relates surface species with each other and/or with species from the gas or bulk environments.

The production rates for each species i due to reaction r are denoted $\dot{\omega}_{ir}$ and are given by equation (5.3). Unlike homogeneous reactions that take place per unit volume, heterogeneous reactions take place on a surface and thus the production of a species is given per unit area of that surface.

$$\dot{\omega}_{ir} = (\nu_{ir}^{''} - \nu_{ir}^{'}) \left\{ k_{fr} \prod_{i=1} X_i^{\nu_{ir}^{''}} - k_{br} \prod_{i=1} X_i^{\nu_{ir}^{''}} \right\} \quad \left[\frac{\mathrm{mol}}{\mathrm{m^2\,s}}\right] \tag{5.3}$$

On the equation above k_{fr} and k_{br} are the forward and backward reaction rates for reaction r respectability. X_i is the concentration of each species and it can have different meanings and units if on the:

- Gas phase: $X_i = C_i = \chi_i \frac{P}{RT}$, $\mathrm{mol\,m^{-3}}$

- Surface phase: $X_i = \phi_{ns,i}$, mol m^{-2}
- Bulk phase: $X_i = \chi_{nb,i}$, adim

While this is expected, since it wouldn't be reasonable to have the surface species, that by definition exist only on the surface, be defined per unit volume or gas species defined per unit area, it is in contrast with the homogeneous reactions where the concentrations of the species all have the same units, namely $\frac{\text{mol}}{\text{m}^3}$. The units of k_{fr} and k_{br} take this into account and adjust in order to ultimately have $\frac{\text{mol}}{\text{m}^2\,\text{s}}$ for the production terms on equation (5.3).

The forward reaction rates can and are often specified by general Arrhenius type expressions. Other times the rates are specified by the expressions 1 to 4 on table 5.1. The difference is that the parameters of the Arrhenius expressions (A, β, E) are sometimes difficult to relate to the physical and chemical processes that constitutes the surface reaction. This new expressions are able to break down this parameters, namely the A coefficient, into sub-parameters that are more insightful.

Reaction Type	**Rate Formula**	**Specified Parameters**
0: Arrhenius	$k_f = AT^{\beta} exp\left(-\frac{E}{RT}\right)$	A, β, E
1: Adsorption	$k_f = \left[\frac{\overline{v}}{4\Phi_s^{\nu_s}}\right] S_0 T^{\beta} exp\left(-\frac{E_{ad}}{RT}\right)$	S_0, β, E_{ad}
2: Eley-Rideal (ER)	$k_f = \left[\frac{\overline{v}}{4\Phi_s^{\nu_s}}\right] \gamma_0 T^{\beta} exp\left(-\frac{E_{er}}{RT}\right)$	γ_0, β, E_{ad}
3: Langmuir-Hinshelwood (LH)	$k_f = \left[\overline{v}_{2D}\Phi_s^{(1.5-\nu_s)}\sqrt{A_v}\right] C_{lh} T^{\beta} exp\left(-\frac{E_{lh}}{RT}\right)$	C_{lh}, β, E_{lh}
4: Sublimation	$k_f = \left[\frac{\overline{v}}{4\Phi_s^{\nu_s} RT}\right] \gamma_{sub} T^{\beta} exp\left(-\frac{E_{sub}}{RT}\right)$	γ_{sub}, β, E_{sub}

Table 5.1: Forward reaction rates. Table reproduced from [20].

At times, the backward reactions can be neglected. When they need to be taken into account, the backward rates need to be computed. Similar to the case for the homogeneous reactions, the backward rates for surface reactions can be directly given or determined through equilibrium constants. The latter situation requires the concentration-based equilibrium constant K_{cr}:

$$k_{br} = \frac{k_{fr}}{K_{cr}} \tag{5.4}$$

The concentration-based equilibrium constant can either be directly specified or computed through the activity-based equilibrium constant K_{ar}:

$$K_{cr} = K_{ar}\left(\frac{P_{ref}}{RT}\right)^{\nu_{gr}} \tag{5.5}$$

Where $P_{\text{ref}} = 1 \times 10^5$ Pa, and ν_{gr} is a stoichiometric coefficient.

In turn the activity-based equilibrium constant can be calculated from changes in the Gibbs energy of formation at temperature T in going from the reactants to products (see [20] for details):

$$K_{ar} = exp\left[\frac{-\Delta G_r^0(T)}{RT}\right] = exp\left[-\sum_{i=1}^{K}\nu_{ir}\frac{G_i^0(T)}{RT}\right] = exp\left[-\sum_{i=1}^{K}\nu_{ir}\left(\frac{H_i^0(T)}{RT} - \frac{S_i^0(T)}{R}\right)\right] \tag{5.6}$$

This approach requires the thermodynamic functions to be known for all species participating in the specific reaction r. Although data for gas phase and bulk phase species is usually accessible, there is rarely information on surface phase species.

5.2 Implementation of the FRSC model on SPARK

When discussing the implementation of catalycity into SPARK in chapter 3, the first step was to develop the mass boundary condition at the wall, which states that the diffusion of each species into the wall is balanced by the consumption of that species:

$$\begin{aligned}(\mathbf{j}_i)_{\text{w, into the wall}} &= (-\dot{\omega}_{i,\text{w}}) \Leftrightarrow \\ -\left(\rho D_i \frac{\partial c_i}{\partial n}\right)_{\text{w}} &= (\dot{\omega}_{i,\text{w}})\end{aligned} \qquad \text{(2.22 revisited)}$$

Afterwards, under the approach of the simple SRE model, expressions for the production terms were presented:

$$\dot{\omega}_{i,\text{w}} = -\gamma_i c_{i,\text{w}} \rho_{\text{w}} \sqrt{\frac{R_i T_{\text{w}}}{2\pi}} \quad \left[\frac{\text{kg}}{\text{m}^2\,\text{s}}\right] \qquad \text{(2.26 revisited)}$$

For the more advanced FRSC model, the mass balance on equation (2.22) remains unchanged but the production terms $\dot{\omega}_{i,w}$ are not as straightforward as they are given by:

$$\dot{\omega}_{i,\text{w}} = \sum_{r=1} (\nu_{ir}^{''} - \nu_{ir}^{'}) \left\{ k_{fr} \prod_{i=1}^{K} X_i^{\nu_{ir}^{''}} - k_{br} \prod_{i=1}^{K} X_i^{\nu_{ir}^{''}} \right\} \quad \left[\frac{\text{mol}}{\text{m}^2\,\text{s}}\right] \qquad \text{(5.3 revisited)}$$

The time accurate implicit discretization of equation (2.22) with the FRSC production terms is challenging but was developed and implemented into the DPLR code by MacLean et al. [17] making the code the state-of-the-art in the field. In contrast, some other authors [21], [46] follow an explicit approach which is easier. It is easier because it maybe done without altering the original CFD code, although that has downsides as decreasing numerical stability. This approach can be readily implemented onto SPARK: First, after each CFD iteration, the steady-state concentration of surface species is computed by solving $K_s - 1$ equations of the form (5.7) together with equation (5.8).

$$\frac{d\Phi_{ns,i}}{dt} = 0 \qquad (5.7)$$

$$\Phi_s = \sum_i \Phi_{ns,i} \qquad (5.8)$$

Where Φ_s is the total active site density and $\Phi_{ns,i}$ is the concentration of surface species i.

After this step, all the surface species concentrations are known which allow for the evaluation of the production terms of the gas species using equation (5.3). Finally, recovering expression (3.7), the new value of each species mass fraction at the wall is computed allowing for the next CFD iteration to take place.

$$c^n_{i,\mathrm{w}} = c^n_{i,\mathrm{i}} + \dot{\omega}^n_{i,\mathrm{w}} \cdot \left(\frac{\Delta n}{\rho_\mathrm{w} D_{i,\mathrm{w}}} \right)^n \tag{3.7 revisited}$$

5.3 Stand Alone Code

The upgrade provided by the FRSC model affects only the production terms $\dot{w}_{i,\mathrm{w}}$ since the physical principles behind the boundary conditions remain as being the conservation of mass and energy at the flow/surface interface. In this regard, the stand alone code can be viewed as a tool to verify the consistency of the production terms and the steady state surface coverage, equation (5.7), under various settings. The idea is for the code to exist independently of SPARK, decoupling the surface chemistry from the flow phenomena occurring on the nearby gas, such as diffusion, convection, heat transfer and gas phase reactions. In other others, there is no flow, only surface reactions that take a system from a initial condition to a steady-state condition. This takes the form of 0D simulations (differential equations in time).

There are 2 types of simulations. In all of them only surface-kinetics and never homogeneous reactions are allowed to occur:

1. **Fixed Gas Phase Composition**

   Here we admit the gas phase has a given composition that is fixed. The temperature and pressure are also prescribed. The surface phase species concentration on the other hand are free to adjust to such composition, via the allowed surface kinetics, from a initial condition. The problems amounts to solving one equation of type (5.9) for each surface species. It's concentration will progress over time until, if correctly posed, the problem will reach a steady-state solution.

   $$\frac{d[X]_s}{dt} = [\dot{w}]_s \tag{5.9}$$

2. **Constant Volume**

   In this case, we eliminate the restrain of constant gas phase composition and allow it to to vary from an initial condition. As a consequence of the changing gas phase composition and the volume and temperature being constant, the pressure will also evolve. It's final value can be computed by the perfect gas law, equation (5.10), where obviously only the gas phase species matter. In addition to the set (5.9) it is now necessary to solve for the unknowns, time changing concentrations of gas phase species, equations (5.11).

   $$p = \rho RT \qquad \text{Where} \qquad R = \sum_i c_i R_i \tag{5.10}$$

   $$\frac{d[X]_g}{dt} = [\dot{\omega}]_g \tag{5.11}$$

Both types constitute a system of coupled ordinary differential equations (ODE) in time. They are solved using a standardized ODE solver named DVODE. This solver package is the same used by the bulk of SPARK in other contexts.

5.3.1 Equilibrium constants to compute surface reaction rates

One important peculiarity of the formulation developed by MacLean et al. is the computation of the backward rates k_{bi} from the equilibrium constants K_{ci} and K_{ai}. As explained previously, this requires the Gibbs energy of formation of all species involved on the particular reaction, but there is no data on the thermodynamic properties of surface species; for example, on the equilibrium constants K_{ai} of the generic ER and LH reactions, equations (5.13)-(5.14), the terms $G^0_{\mathrm{A(s)}}(T)$ and $G^0_{\mathrm{(s)}}(T)$ are unknown. The workaround consists in specifying both the forward and backward reaction rates for each adsorption reaction. In doing so it is possible to evaluate the activity base equilibrium constant $K_{a,ads}$ and then extract the term $\left(\frac{G^0_{\mathrm{A(s)}}(T)}{RT} - \frac{G^0_{\mathrm{(s)}}(T)}{RT}\right)$ by inverting equation (5.12). This process is illustrated on figure 5.2.

$$K_{a,ads} = exp\left[\frac{G^0_{\mathrm{A}}(T)}{RT} - \left(\frac{G^0_{\mathrm{A(s)}}(T)}{RT} - \frac{G^0_{\mathrm{(s)}}(T)}{RT}\right)\right] \tag{5.12}$$

$$K_{a,ER} = exp\left[-\left(\frac{G^0_{\mathrm{AB}}(T)}{RT} - \frac{G^0_{\mathrm{B}}(T)}{RT}\right) + \left(\frac{G^0_{\mathrm{A(s)}}(T)}{RT} - \frac{G^0_{\mathrm{(s)}}(T)}{RT}\right)\right] \tag{5.13}$$

$$K_{a,LH} = exp\left[-\frac{G^0_{\mathrm{AB}}(T)}{RT} + \left(\frac{G^0_{\mathrm{A(s)}}(T)}{RT} - \frac{G^0_{\mathrm{(s)}}(T)}{RT}\right) + \left(\frac{G^0_{\mathrm{B(s)}}(T)}{RT} - \frac{G^0_{\mathrm{(s)}}(T)}{RT}\right)\right] \tag{5.14}$$

The Gibbs energies for the gas phase species, A and AB, should be readily available from the literature. SPARK obtains the thermodynamic data from the NASA Glenn compilation of thermodynamic properties [47].

This manoeuvre is widely employed by our source paper of MacLean et al. [20]. In essence it consists in shifting the uncertainty from prescribing equilibrium constants directly for the ER and LH reactions or finding the thermodynamic functions of the surface species to the uncertainty of specifying backward rates for adsorption reactions. The advantage is, according with the reference, that the backward rate for adsorption can be derived from simple statistical thermodynamics and kinetic theory.

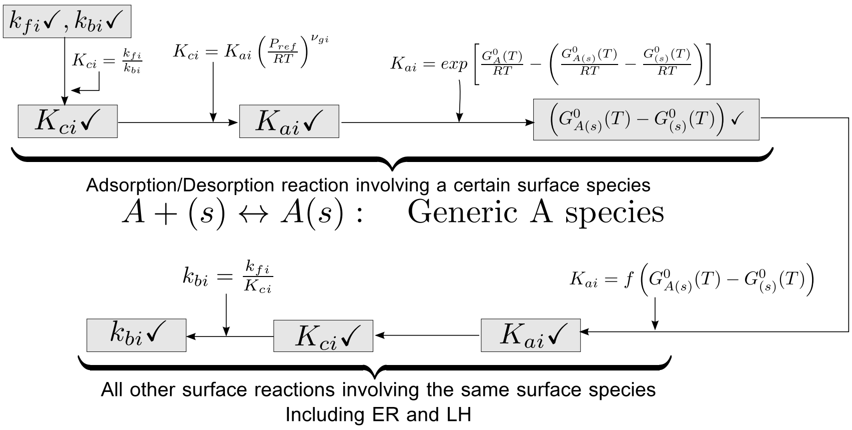

Figure 5.2: Practice to compute thermodynamic variables for surface species.

5.4 Results of the Stand Alone Code

On this section, the current results are matched with MacLean et al. [20]. There are only available for comparison steady-state solutions but on section B.4 of the appendix there are some transient results from the current stand alone code as a reference.

There are 2 cases. On the first the gas phase composition is fixed and only the surface species equations (5.9) are solved for 3 different pressures and a wide spectrum of temperatures. On the second case, the gas phase composition is allowed to vary by adding equations (5.11) and solving them for the same temperature and initial pressure but assuming different sets of surface reactions.

5.4.1 Fixed Gas Phase of Dissociated Oxygen

The first case studied concerned a gas composed of partially dissociated oxygen. The species taken into account were O_2 and O for the gas phase, adsorbed oxygen O(s) and free-sites E(s) for the surface phase and no bulk phase. Only 3 reactions were simulated as to allow for recombination: One adsorption reaction for O atoms to stick to the surface and 2 recombination reactions (1 Eley-Rideal(ER) and 1 Langmuir-Hinshelwood(LH)) to form O_2. The information is summarized in table 5.2.

Phases	**Species**	**Initial Condition**	
Gas	O_2, O	$C_{\mathrm{O_2}}$=0.9, C_{O}=0.1	
Surface	O(s), E(s)	$\Phi_{1,\mathrm{O(s)}}$ = 0, $\Phi_{1,\mathrm{(s)}}$ = 7.5E-6 mol/m^2	
Reaction	**Form**	**Parameters**	
		Forward Reaction	Backward Reaction
Adsorption	R1: O + (s) $\leftrightarrow$ O(s)	S_0 = 0.05 , β = 0 E_{ad} = 0	A_{des} = 1,ν = 1.0E12 s^{-1} β = 0, $E_{des} = 350000$ J mol^{-1}
ER	R2: O + O(s) $\leftrightarrow$ O_2 + (s)	γ_{er} = 0.001 , β = 0, E_{er} = 9000 J mol^{-1}	-
LH	R3: O(s) + O(s) $\leftrightarrow$ O_2 + 2(s)	C_{lh} = 0.1 , β = 0 E_{lh} = 300000 J mol^{-1}	-

Table 5.2: Summary of the data of the problem. Fixed gas phase of dissociated oxygen.

The parameters for the backward reaction of the adsorption reaction concern expression (5.15)

$$k_b = k_{des} = A_{des} T^{\beta} \nu exp\left(-\frac{E_{des}}{RT}\right) \tag{5.15}$$

On both figures 5.3 and 5.4, and for clarity of the presentation, there is only on thick black line representing all MacLean et al. cases for which there also exists results for the current implementation. For both the surface coverage of O-atoms (O(s)) and the loss efficiency of O and O_2 the current results are indistinguishable from those of MacLean at al.

The main cause of an eventual disagreement between the results is not knowing how MacLean et al. computes the Gibbs energy for the gas phase species. However, given the match of the results, either they also use the NASA polynomials [47], or the difference of the methods is insignificant.

Passing now to the physical analysis of the results, the first comment is that every point on both figures,

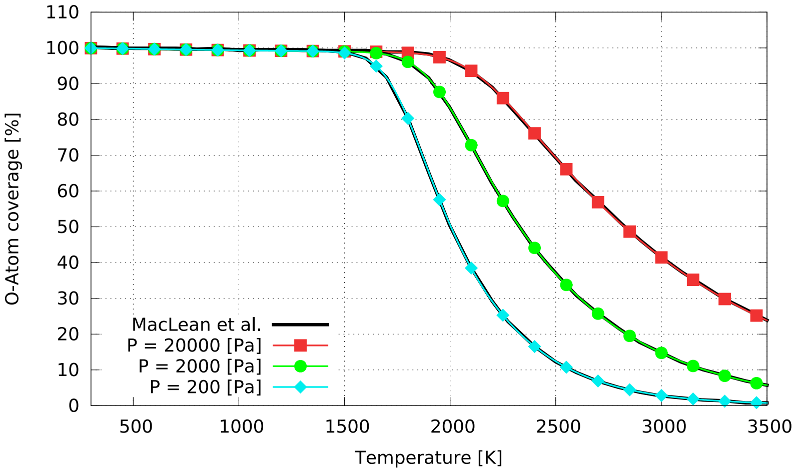

Figure 5.3: Comparison between the current results and results from MacLean et al. [20]. Percentage of sites containing O(s) as a function of temperature for 200, 2000 and 20000 Pa. Case: 10% O - 90% O_2.

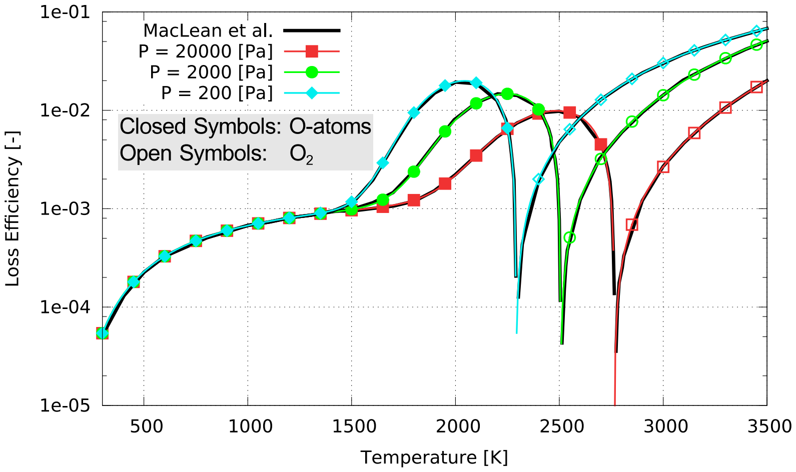

Figure 5.4: Comparison between the current results and results from MacLean et al. [20]. Loss efficiency as a function of temperature for 200, 2000 and 20000 Pa. Case: 10% O - 90% O_2.

despite representing a steady-state solution, doesn't constitute a thermodynamic equilibrium state. This is because, in general, the fixed gas phase composition (90 % O_2 - 10% O) is not compatible with the steady-state achieved by the surface species and should actually be changing in order to conciliate with the steady-state. By other words, the results contradict the assumptions. To see this we first develop the production term for the O specie:

$$\frac{dC_\mathrm{O}}{dt} = \dot{\omega}_\mathrm{O} = -k_{f1}C_\mathrm{O}\Phi_{(\mathrm{s})} + k_{b1}\Phi_{\mathrm{O(s)}} - k_{f2}C_\mathrm{O}\Phi_{\mathrm{O(s)}} + k_{b2}C_{\mathrm{O}_2}\Phi_{1,(\mathrm{s})} \tag{5.16}$$

We then take a random point from figure 5.3, say (P = 20 000 Pa, T = 3000 K) where there is a 40% coverage of O-atoms. As the total distribution of sites, empty or with O, is $\Phi_\mathrm{s} = 7.5 \times 10^{-6}\ \frac{\mathrm{mol}}{\mathrm{m}^2}$, then we have $\Phi_{1,\mathrm{O(s)}} = 3 \times 10^{-6}\ \frac{\mathrm{mol}}{\mathrm{m}^2}$ and $\Phi_{1,(\mathrm{s})} = 4.5 \times 10^{-6}\ \frac{\mathrm{mol}}{\mathrm{m}^2}$. With this, and assuming the said constant composition for the gas phase of $C_\mathrm{O} = 0.1\frac{P}{RT} = 0.008\ \frac{\mathrm{mol}}{\mathrm{m}^3}$ and $C_{\mathrm{O}_2} = 0.9\frac{P}{RT} = 0.0721\ \frac{\mathrm{mol}}{\mathrm{m}^3}$, we get $\frac{dC_\mathrm{O}}{dt} = 1.354\ \frac{\mathrm{mol}}{\mathrm{m}^3}$ when it should equal zero, thus showing a changing gas phase composition.

This could also have been showed by simply noting that, on figure 5.4, there is an active loss of O_2 molecules for the same state (P = 2000 Pa, T = 3000 K).

This apparent inconsistency stems from just solving the equations (5.9) for the surface species and ignoring the equations (5.11) for the gas phase species. Given the above analysis, this case is representative of an actual CFD simulation where the gas flow near the catalytic wall is such that it is instantly providing/absorving the necessary/excess O and O_2 so that in practice the gas phase composition remains the same.

5.4.2 Silica Sublimation

This second study concerns silica sublimation, a typical compound of many TPS as reported on the introduction 1. In contrast with the previous case, the gas phase composition is not fixed but allowed to vary with the surface species and thus the steady-state reached is an equilibrium solution.

Initially the system is composed of Argon at 10 000 Pa in the gas phase and bulk Silica on the bulk phase. The temperature is fixed at 2500 K but the pressure varies according with this fixed temperature, the fixed volume, and the composition.

The details of the problem are on table 5.3. There are 5 reactions: Sublimation allows for the bulk silica to vaporize into the gas phase with mediation by the surface sites (s1). The participation of surface sites (s1) is an artifice to describe the reaction on the same grounds as catalytic reactions. Furthermore, there is adsorption of oxygen atoms onto to the surface and 3 ER reactions concerning the absorbed O(s1) species and species O, SiO and Si from the gas phase.

Notice that the appearance of gas species other than Argon depends directly on the catalytic reactions. For example, without the first ER reaction O_2 could never be created. Following the description of MacLean et al. [20, pp. 26-29] table 5.4 presents the equilibrium compositions when considering subsets of the 5 reactions.

Phases	**Species**	**Initial Condition**	
Gas	O_2, O, Ar, SiO_2, SiO, Si	Only Argon	
Surface	E(s1), E(s2), O(s2)	$\Phi_{1,\mathrm{E(s1)}} = \Phi_{1,\mathrm{E(s2)}} = 3.75 \times 10^{-6}\,\mathrm{mol\,m^{-2}}$	
Bulk	Bulk silica - SiO_2(b1)	$\chi_{\mathrm{SiO_2(b1)}}$=cte=1	
Reaction	**Form**	**Parameters**	
		Forward Reaction	Backward Reaction
Sublimation	RC1: (s1) + SiO_2(b1) $\leftrightarrow$ SiO_2 + (s1)	γ_{sub}=3.5E13, β=0 $E_{sub} = 565352$	-
Adsorption	RC2: O + (s2) $\leftrightarrow$ O(s2)	-	
ER	RC3: O + O(s2) $\leftrightarrow$ O_2 + (s2)	-	
	RC4: SiO + O(s2) $\leftrightarrow$ SiO_2 + (s2)	-	
	RC5: Si + O(s2) $\leftrightarrow$ SiO + (s2)	-	

Table 5.3: Summary of the data of the problem. Silica Sublimation. The parameters for the adsorption and all 3 ER reactions are the same as the parameters for the adsorption and ER reactions present on table 5.2 respectively.

The first subset consists in just sublimation of silica, i.e reaction RC1. Naturally only SiO_2 is present at steady-state as no mechanism can form the other species. This simple case is equivalent to equating equation (5.17) to zero, where the backward rate k_{b1} is computed using the equilibrium constant K_{c1}. Because the active sites (s1) appear as reactants and products, there is no need to know the Gibbs energy of formation of that species as shown on equations (5.18).

$$\frac{dC_{\mathrm{SiO_2}}}{dt} = k_{f1}\chi_{\mathrm{SiO_2(b1)}}\Phi_{\mathrm{(s1)}} - k_{b1}C_{\mathrm{SiO_2}}\Phi_{\mathrm{O(s)}} \tag{5.17}$$

$$\begin{aligned} K_{a1} &= exp\left[-\left(\frac{G^0_{\mathrm{SiO_2}}(T)}{RT}+\frac{G^0_{\mathrm{(s1)}}(T)}{RT}-\frac{G^0_{\mathrm{(s1)}}(T)}{RT}-\frac{G^0_{\mathrm{SiO_2(b1)}}(T)}{RT}\right)\right] \Leftrightarrow \\ K_{a1} &= exp\left[\frac{G^0_{\mathrm{SiO_2(b1)}}(T)}{RT}-\frac{G^0_{\mathrm{SiO_2}}(T)}{RT}\right] \end{aligned} \tag{5.18}$$

On the second set RC2 and RC4 are added. The backward mechanism of reaction RC4 dissociates the previously sublimated silica into SiO and ensures the adsorption of O atoms on the surface, while reaction RC2 promotes the desorption of this surface specie O(s2) for the creation of O.

On the third subset RC3 is added allowing the formation of O_2, with the set being completed by the inclusion of reaction RC5 which allocates a trace amount of Si.

For all the entries in table 5.4 there is a great match between MacLean et al. and the current results, with the difference no higher than 0.5%.

Notice further that the active sites (s1) and (s2) are conserved. The sum of the concentration of surface species O(s2) and E(s2) always equals the concentration of active (s2) sites, $3.75 \times 10^{-6}\ \frac{\mathrm{mol}}{\mathrm{m}^2}$.

Species	O_2	O	SiO_2	SiO	Si	E(s1)	E(s2)	O(s2)	Pressure [Pa]
Initial	0	0	0	0	0	3.75E-6	3.75E-6	0	10000
RC1	0	0	2.9841E-3	0	0	3.75E-6	3.75E-6	0	0
RC1 (MacLean)	0	0	2.9970E-3	0	0	3.75E-6	3.75E-6	0	10062
RC124	0	8.6193E-3	2.9881E-3	8.6206E-3	0	3.75E-6	2.4401E-6	1.3099E-6	0
RC124 (MacLean)	0	8.6199E-3	2.9970E-3	8.6212E-3	0	3.75E-6	2.4401E-6	1.3099E-6	10421
RC1234	1.0065E-2	3.1867E-3	0	2.3317E-2	0	3.75E-6	3.129E-6	6.2102E-7	0
RC1234 (MacLean)	1.0066E-2	3.1868E-3	2.9970E-3	2.3319E-2	0	3.75E-6	3.129E-6	6.2098E-7	10822
RC12345	1.0065E-2	3.1867E-3	2.9882E-3	2.3317E-2	3.8531E-9	3.75E-6	3.129E-6	6.2102E-7	0
RC12345 (MacLean)	1.0066E-2	3.1868E-3	2.9970E-3	2.3319E-2	3.8645E-9	3.75E-6	3.129E-6	6.2098E-7	10822

Table 5.4: Concentration of gas ($\mathrm{mol\,m^{-3}}$) and surface ($\mathrm{mol\,m^{-2}}$) species in steady-state(equilibrium) enabled by different sets of catalytic reactions at constant volume and constant temperature T = $2500\,\mathrm{K}$. Comparison between current results and results from MacLean et al. [20]. Silica sublimation case.

Chapter 6

Conclusions

6.1 Achievements

Before the current work, SPARK did not have the capability to account for catalycity in re-entry simulations. It neglected the phenomenon by assuming the wall of a re-entry vehicle is indifferent to surface reactions. This limited the application of SPARK to simulations where catalycity was not expected to play a significant role. When catalycity is relevant, it primarily affects the heat flux into the vehicle and the gas composition near the surface.

The current work implemented catalycity in SPARK for Earth re-entry following a phenomenological approach. Through it, two catalytic reactions are accounted for: N_2 and O_2 recombination. Modelling them consists in recognizing a parameter, the reaction efficiency γ, that quantifies the ratio of the incoming N and O atoms that achieve recombination. The reaction efficiency γ is introduced by the user, which can also select pre-defined models. By choosing $\gamma = 1$ the model defaults to the worst case scenario in terms of the quantity of heat flux entering the vehicle and thus equips SPARK the ability to define an upper bound on heat flux for a particular re-entry simulation. The account of surface reactions at the surface also required a mass and energy balance at the wall which was not done before in SPARK. From the energy balance point of view two alternatives were implemented. One for constant wall temperature T_w, and the other for radiative equilibrium where it is assume that all the incoming energy flux due to temperature gradients and catalycity is re-radiated by the surface. To verify and validate the implementation a battery of simulations were ran and the results compared with several other computational codes and experimental data. Given the results, doubts remain on whether the implementation was successful. Further analysis is needed.

Another achievement was the formulation of a more advanced approach named FRSC model. Due to the added complexity this alternative required the previous development of a stand-alone code in which the surface catalycity is detached from the Navier-Stokes (NS) equations. This stand-alone code serves as the antechamber for a posterior full implementation in SPARK. The results were compared with other codes.

6.2 Future Work

The order of things to be done can be categorized in two areas. Firstly it should be concluded whether or not the current implementation is completely correct and if not so, correct it. After this there a number of improvements possible for the SRE approach: the recombination of nitrogen oxide ($\mathrm{N} + \mathrm{O} \longrightarrow \mathrm{NO}$) could be implemented, the SEB boundary condition could be updated to allow conduction to the wall or conduction could be modelled in the solid and coupled to the SEB condition. Reactions for CO_2 recombination can be introduced to allow simulating a Mars re-entry. However all this sub steps would ultimately be limited by the simplicity of the SRE model. Thus, the second step is to improve the modelling of catalycity with the FRSC model which is more versatile:

- **1^{st}: Guarantee the correct implementation so far**
  Following the discussion on section 4.4, this would require analysing the theoretical implementation of boundary conditions in other aerothermodynamics CFD codes that discretize the NS equations on the same way as SPARK. The LAURA and DPLR are examples of such codes. In parallel simple simulations over simple geometries as flat plates would be useful because one could focus on the effects of the metric terms originating from the transformation.
- **2^{nd}: Incorporate the finite-rate chemistry model (FRSC)**
  Following the discussion on section 5.2 this can be promptly achieved by and explicit approach. To this aid, the stand-alone code serves as foundation. This is not the most competent approach albeit in practice it works quite well. So the next step, after the explicit approach has been achieved, is to implicitize the FRSC model. In the end SPARK would be equipped with a state-of-the-art catalycity module capable of predicting ablation and pyrolysis.

Bibliography

[1] J. D. Anderson Jr. *Hypersonic And High-Temperature Gas Dynamics*. AIAA, 2^{nd} edition, 2006.

[2] W. G. Vincenti and C. H. Kruger. *Introduction to Physical Gas Dynamics*. Krieger Publishing Company, Reprint of the 1967 ed. published by Wiley, New York.

[3] P. A. Gnoffo. Planetary-entry gas dynamics. *Annual Review of Fluid Mechanics*, 31:459–494, 1999.

[4] W. L. Hankey. *Re-entry Aerodynamics*. AIAA Educational Series, 1988.

[5] J. D. Anderson Jr. *Modern Compressible Flow with Historical Perspective*. McGraw-Hill, Inc, 2^{nd} edition, 1990.

[6] D. Bianchi. *Modeling of ablation phenomena in space applications*. PhD thesis, Università degli Studi di Roma ”La Sapienza”, Dipartimento di Meccanica e Aeronautica, 2006/2007.

[7] B. Laub and E. Venkatapathy. Thermal protection system technology and facility needs for demanding future planetary missions. In Workshop on *Planetary Probe Atmospheric Entry and Descent Trajectory Analysis and Science, Lisbon, Portugal*, October 2003.

[8] S. M. Jonhson. Approach to tps development for hypersonic applications at nasa ames research center. Proceedings 5^{th} European Workshop on Thermal Protection Systems and Hot Structures, Noordwijk, The Netherlands, 2006.

[9] C. D. Scott. Catalytic recombination of nitrogen and oxygen on high-temperature reusable surface insulation. In *AIAA 15^{th} Thermophysics Conference, July 14-16, 1980/Snowmass, Colorado*, number AIAA-80-1477.

[10] E. Zoby, R. Gupta, and A. Simmonds. Temperature-dependent reaction-rate expression for oxygen recombination at shuttle entry conditions. In *AIAA 22^{nd} Aerospace Sciences Meeting, January 9-12, 1984/Reno, Nevada*, number AIAA-84-0224.

[11] A. Abhilasha. *Numerical Modeling of Surface Chemistry Processes for Hypersonic Entry Environments*. PhD thesis, The University of Michigan, 2013.

[12] H. Molavi, A. Hakkaki-Fard, I. Pourshaban, I. Mahbubi Fard, and R. K. Rahmanis. Estimation of temperature-dependent thermophysical properties of noncharring ablators. *Journal of Thermophysics and Heat Transfer*, 23(1), January-March 2009.

[13] R. Beck. Ablative thermal protection systems fundamentals. In International Planetary Probe Workshop 10, San Jose, California, June 15-16, 2013.

[14] J. H. Grinstead, D. A. Stewart, and C. A. Smith. High enthalpy test methodologies for thermal protection systems development at nasa ames research center. *AIAA 2005-3326*.

[15] A. Martin, L. C. Scalabrin, and I. D. Boyd. High performance modeling of atmospheric re-entry vehicles. *Journal of Physics: Conference Series 341*, (012002), 2012.

[16] M. J. Wright, G. V. Candler, and D. Bose. Data-parallel line relaxation method for the navier-stokes equations. *AIAA Journal*, 36(9), September 1998.

[17] M. MacLean, J. Marschall, and D. M. Driver. Finite-rate surface chemistry model, ii: Coupling to viscous navier-stokes code. *AIAA 2011-3784*.

[18] R. A. Thompson and P. A. Gnoffo. Implementation of a blowing boundary condition in the laura code. *AIAA 2008-1243*.

[19] F. S. Milos and D. J. Rasky. Review of numerical procedures for computational surface thermochemistry. *Journal of Thermophysics and Heat Transfer*, 8(1), January-March 1994.

[20] J. Marschall and M. MacLean. Finite-rate surface chemistry model, i: Formulation and reaction system examples. *AIAA 2011-3783*.

[21] H. Alkandry, E. D. Farbar, and I. D. Boyd. Evaluation of finite-rate surface chemistry models for simulation of the stardust reentry capsule. *AIAA 2012-2874*.

[22] J. D. Anderson. *Fundamentals of Aerodynamics*. McGraw-Hill, 4^{th} edition, 2007. International Edition.

[23] B. Lopez. *Simulation Des Écoulements De Plasma Hypersonique Hors Équilibre Thermochimique*. PhD thesis, Université D' Orléans, 2010.

[24] R. N. Gupta, J. M. Yos, R. A. Thompson, and K.-P. Lee. A review of reaction rates and thermodynamic and transport properties for an 11-species air model for chemical and thermal nonequilibrium calculations to 30 000 k. Technical Report RP-1232, NASA Langley Research Center, August 1990.

[25] M. Barbato, D. Giordano, and C. Bruno. Comparison between finite rate and other catalytic boundary conditions for hypersonic flows. *AIAA 94-2074*, 1994. 6^{th} AIAA/ASME Joint Thermophysics and Heat Transfer Conference, June 20-23, 1994/Colorado Springs, CO.

[26] L. M. F. M. Walpot. *Development and Application of a Hypersonic Flow Solver*. PhD thesis, Technische Universiteit Delft, 2002.

[27] C. D. Scott. Wall catalytic recombination and boundary conditions in nonequilibrium hypersonic flows - with applications. In *Advances in Hypersonics*, volume 8/9, chapter Modeling Hypersonic Flows, pages 176–250. Birkhäuser Boston, 1992.

[28] J. Marschall. Laboratory determination of thermal protection system materials surface catalytic properties. In *TRO-EN-AVT-142, Paper 11*.

[29] C. D. Scott. Wall boundary equations with slip and catalysis for multicomponent nonequilibrium gas flows. NASA TM X-58111, December 1973.

[30] J. H. Miller, J. C. Tannehill, G. Wadawadigi, T. A. Edwards, and S. L. Lawrence. Computation of hypersonic flows with finite-catalytic walls. In 25^{th} *AIAA Fluid Dynamics Conference, June 20-23/1994 Colorado Springs, CO*, number AIAA 94-2354.

[31] O. Chazot. An integrated experimental and computational study of heating due to surface catalysis under hypersonic conditions. Technical Report EOARD Grant 11-3066, Institut Von Karman De Dynamique Des Fluids, August 2012.

[32] J. Muylaert, L. Walpot, M. Spel, P. Sagnier, K. Hannemann, and H. Olivier. A review of european code validation studies in high enthalpy flow. *American Institute of Aeronautics and Astronautics, Inc.*, (98-2769), 1998.

[33] P. Kolodziej and D. A. Stewart. Nitrogen recombination on high-temperature reusable surface insulation and the analysis of its effect on surface catalysis. In *AIAA* 22^{nd} *Thermophysics Conference, June 8-10, 1987/Honolulu, Hawaii*, number AIAA-87-1637.

[34] F. G. Blottner, M. Jonhson, and M. Ellis. Chemically reacting viscous flow program for multi-component gas mixtures. Technical report, Sandia Laboratories, Albuquerque, New Mexico, December 1971. Report SC-RR-70-754.

[35] C. Park, R. Jaffe, and H. Partridge. Chemical kinetics parameters of hyperbolic earth entry. *Journal of Thermophysics and Heat Transfer*, 15(1), 2001.

[36] J. C. Tannehill, D. A. Anderson, and R. H. Pletcher. *Computational Fluid Mechanics and Heat Transfer*. 2^{nd} edition, 1997.

[37] B. Rousset and P. Adam. Electre experiments in t5. Technical report, Graduate Aeronautical Laboratories California Institute of Technology, Pasadena, California, September 1993.

[38] A. Viviani and G. Pezzella. Nonequilibrium aerothermodynamics for a capsule reentry vehicle. In *Engineering Applications of Computational Fluid Mechanics*, volume 3, pages 543–561. 2009.

[39] E. H. Hirschel. *Basics of Aerothermodynamics*. Springer, second, revised edition edition, 2015.

[40] D. Loureiro. High-temperature modeling of transport properties in hypersonic flows. Master's thesis, Instituto Superior Técnico, November 2015.

[41] F. S. Billig. Shock-wave shapes around spherical- and cylindrical-nosed bodies. *Journal of Spacecraft and Rockets*, 4(6):822–833, June 1967.

[42] J. D. Anderson, L. M. Albacete, and A. E. Winkelmann. Comment on shock-wave shapes around spherical- and cylindrical-nosed bodies. *Journal of Spacecraft and Rockets*, 5(10):1247–1248, October 1968.

[43] C. Godart, M. V. Salvetti, and J. A. Désidéri. Numerical comparison of wall catalysis models for hypersonic reactive air flows. 3^{rd} Workshop on Modelling of Chemical Reactions Systems, July 24-26, 1996, Heidelberg, Germany.

[44] W. L. Oberkampf and C. J. Roy. *Verification and Validation in Scientific Computing*. Cambridge University Presss, New York, 2010.

[45] J. D. Anderson. *Computational Fluid Dynamics The Basics with Applications*. McGraw-Hill, 1995.

[46] C. Sorensen, P. Valentini, and T. E. Schwartzentruber. Uncertainty analysis of reaction rates in a finite-rate surface-catalysis model. *Journal of Thermophysics and Heat Transfer*, 26(3):407–416, 2012.

[47] B. J. McBride, M. J. Zehe, and S. Gordon. Nasa glenn coefficients for calculating thermodynamic properties of individual species. Technical Report NASA/TP - 2002-211556, Glenn Research Center, Cleveland, Ohio, September 2002.

[48] J. H. Ferziger and M. Perić. *Computational Methods for Fluid Dynamics*. Springer, 3^{rd} edition, 2002.

Appendix A

Discretization of the Navier-Stokes equations

The purpose of the following derivations is to give a general but accurate overview of the process trough which SPARK discretizes and solves the Navier-Stokes equations. For a complete study the reader should consult the work of Lopez, 2010 [23] that serves the foundation of SPARK and that of Walpot, 2002 [26] whose hypersonic code is similar to SPARK.

A.1 Transformation of Variables

It is convenient to cast the Navier-Stokes (NS) equations in vectorial form. For a 2-dimension flow the NS equations (2.1 - 2.4) are written as:

$$\vec{Q}_t + \vec{E}_x + \vec{F}_y = \vec{\Omega}, \tag{A.1}$$

where the subscripts correspond to differentiation and $\vec{Q}$ and $\vec{\Omega}$ are the vectores of the conservative variables and the source terms, respectively:

$$\begin{aligned} \vec{Q} &= (\rho_i, \rho u, \rho v, \rho E)^T \\ \vec{\Omega} &= (\dot{\omega}_i, 0, 0, 0)^T \end{aligned} \tag{A.2}$$

Also, the flux vectors $\vec{E}$ and $\vec{F}$ in the x-, and y- direction are given by:

$$\vec{E} = \begin{bmatrix} \rho_i u - \rho_i D_i c_{i_x} \\ \rho u u - \sigma_{xx} \\ \rho v u - \sigma x y \\ (e - \sigma x x) u - \sigma x y v - q_{T_x} - q_{d_x} \end{bmatrix} \qquad \vec{F} \ = \begin{bmatrix} \rho_i v - \rho_i D_i c_{i_y} \\ \rho u v - \sigma_{yx} \\ \rho v v - \sigma y y \\ (e - \sigma y y) v - \sigma y x u - q_{T_y} - q_{d_y} \end{bmatrix} \tag{A.3}$$

The discretization could take place using equation A.1, but what is often done, as in the case of SPARK, is to transform equation A.1 from the physical domain of (x, y) to a computational domain of coordinates (ξ, η) by:

$$x = x(\xi, \eta), \qquad y = y(\xi, \eta) \tag{A.4}$$

The resulting Navier-Stokes equations are:

$$\hat{Q}_t + \hat{E}_\xi + \hat{F}_\eta = \hat{\Omega}, \tag{A.5}$$

Where $\hat{Q}$, $\hat{E}$, $\hat{F}$ and $\hat{\Omega}$ are related to the previous vectorial quantities:

$$\begin{aligned} \hat{Q} &= J\vec{Q} \\ \hat{E} &= \left(\vec{E}\xi_x + \vec{F}\xi_y\right) \\ \hat{F} &= \left(\vec{E}\eta_x + \vec{F}\eta_y\right) \\ \hat{\Omega} &= J\vec{\Omega} \end{aligned} \tag{A.6}$$

Where J is the jacobian of the transformation, and ξ_x, ξ_y, η_x and η_y are known as metric terms. Amongst other advantages, this transformation is useful when the physical domain has a complex configuration. The objective is thus to solve the equations in a ”effortless” domain, the computational domain, although in the process the equivalent system of equations changes from equations A.1 to equations A.5, this last one including the information of the transformation through the metric terms and the Jacobian.

The reader should note that no discretization as yet taken place. All the above derivation is analytical.

A.2 Finite-Volume Discretization

The next step begins by the volume integration of the transformed NS equations, which constitutes the foundation of the finite volume method:

$$\iiint_V \frac{\partial \hat{Q}}{\partial t}\, dV + \iiint_V \left(\frac{\partial \hat{E}}{\partial \xi} + \frac{\partial \hat{E}}{\partial \eta}\right) dV = \iiint_V \vec{\Omega}\, dV \tag{A.7}$$

Applying the Gauss theorem on the second term of the l.h.s, and noticing the integration and differentiation operators in the first term of the l.h.s are permutable:

$$\frac{\partial}{\partial t}\iiint_V \hat{Q}\, dV + \iint_S \left(\hat{E}\,\vec{e}_\xi + \hat{F}\,\vec{e}_\eta\right) dS = \iiint_V \vec{\Omega}\, dV \tag{A.8}$$

Where $\vec{e} = (\vec{e_\xi},\, \vec{e_\eta})$ is a unit vector in the computational space $\xi - \eta$ normal to the surface dS and oriented to the exterior of dV.

In the above equations, dV is an arbitrary control volume. Applying the above formula, at once, to an entire domain governed by the NS, would not be particularly helpful. The objective with the finite volume technique is to discretize the domain in several volume cells (finite volumes) and then apply to each one equation A.8. Using the nomenclature of figure A.1 we apply it to one such finite cell:

$$\frac{\partial}{\partial t}\iiint_V \hat{Q}\, d\xi\, d\eta + \left(\iint_{S_{i+\frac{1}{2},j}} \hat{E}\, d\eta - \iint_{S_{i-\frac{1}{2},j}} \hat{E}\, d\eta\right) + \left(\iint_{S_{i,j+\frac{1}{2}}} \hat{F}\, d\xi - \iint_{S_{i,j+\frac{1}{2}}} \hat{F}\, d\xi\right) = \iiint_V \vec{\hat{\Omega}}\, d\xi\, d\eta \tag{A.9}$$

Up until now, every derivation was exact and no discretization formally took place. Now, because the integrands in the volume and surface integrals are not known, i.e it is not know how $\hat{Q}$ and $\hat{\Omega}$ vary within the volume and is not know how $\hat{E}$ and $\hat{F}$ vary across the boundaries S, approximations must be introduced [48, ch. 4]. To that end, $\hat{Q}$ and $\hat{\Omega}$ are assumed constant over each volume $V_{i,j}$ whose value is located at the cell centres. Similarly, the flux vectors $\hat{E}$ and $\hat{F}$ are assumed to be constant over the cell faces $S_{i,j}$. The integrals can then be evaluated, leading to:

$$\frac{\partial \hat{Q}_{i,j}}{\partial t} + \frac{\hat{E}_{i+\frac{1}{2},j} - \hat{E}_{i-\frac{1}{2},j}}{\Delta\xi} + \frac{\hat{F}_{i,j+\frac{1}{2}} - \hat{F}_{i,j-\frac{1}{2}}}{\Delta\eta} = \hat{\Omega}_{i,j} \tag{A.10}$$

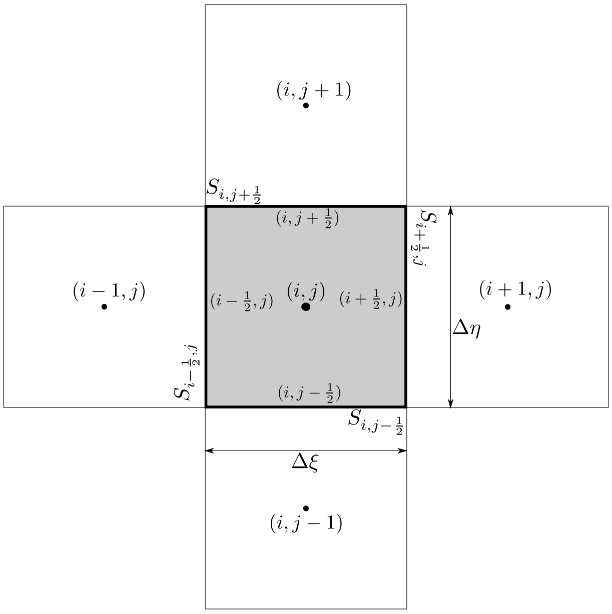

Figure A.1: A typical control volume cell and its neighbours along with the surface frontiers S and the remaining notation used.

A.2.1 Explicit Time Integration

The discretization in space has been partially done above and will be completed on the next section. In the meantime, it is required to discretize the time dependence on the first term of equation A.10, resulting in the equations being solved for a finite number of intervals $[t_n, t_{n+1}]$.

There are two types of time discretization: implicit and explicit . SPARK has both approaches available, but the catalytic capabilities implemented assumed a explicit discretization. An explicit approach is by definition one where equation A.10 for each volume cell (i, j) contains a single unknown term in time $t_{n+1} = t_n + \Delta t$, while others are known terms in the current time step t_n [45, ch. 4]. With the above definition, the time derivative is first discretized by a first-order approximation which then leads to equation A.12.

$$\frac{\partial \hat{Q}}{\partial t} = \frac{\hat{Q}^{n+1}_{i,j} - \hat{Q}^{n}_{i,j}}{\Delta t} \tag{A.11}$$

$$\begin{aligned} \frac{\hat{Q}^{n+1}_{i,j} - \hat{Q}^{n}_{i,j}}{\Delta t} &= \hat{\Omega}^{n}_{i,j} - \left(\frac{\hat{E}^{n}_{i+\frac{1}{2},j} - \hat{E}^{n}_{i-\frac{1}{2},j}}{\Delta \xi} + \frac{\hat{F}^{n}_{i,j+\frac{1}{2}} - \hat{F}^{n}_{i,j-\frac{1}{2}}}{\Delta \eta} \right) \Leftrightarrow \\ \hat{Q}^{n+1}_{i,j} &= \hat{Q}^{n}_{i,j} + \Delta t \left[\hat{\Omega}^{n}_{i,j} - \left(\frac{\hat{E}^{n}_{i+\frac{1}{2},j} - \hat{E}^{n}_{i-\frac{1}{2},j}}{\Delta \xi} + \frac{\hat{F}^{n}_{i,j+\frac{1}{2}} - \hat{F}^{n}_{i,j-\frac{1}{2}}}{\Delta \eta} \right) \right] \end{aligned} \tag{A.12}$$

A.2.2 Spacial Discretization of the Fluxes

From equation A.10 and figure A.1 it can be noticed that the fluxes $\hat{E}$ and $\hat{F}$ are evaluated at the cell faces (e.g $\hat{E}^{n}_{i+\frac{1}{2},j}$ on face $S_{i+\frac{1}{2},j}$) but in the finite volume method all the information is stored on the cell centres. Therefore the last step consists in expressing the cell faced values of the fluxes in terms of the cell centres. The methodology followed by SPARK is lengthy . Here just the diffusive fluxes will be covered. Again the reader is referred to references [23] and [26].

If ϕ represents any given variable inside the fluxes $\hat{E}$ and $\hat{F}$ then:

$$\phi_{i+\frac{1}{2},j} = \frac{1}{2}\left(\phi_{i,j} + \phi_{i+1,j}\right) \tag{A.13}$$

$$\left(\frac{\partial \phi}{\partial \xi}\right)_{i+\frac{1}{2},j} = \frac{1}{\Delta \xi}\left(\phi_{i+1,j} - \phi_{i,j}\right) \tag{A.14}$$

Notice that this procedure effectively couples the equations for all the finite volume cells.

Appendix B

Other Computational Results

B.1 Sharp Cones

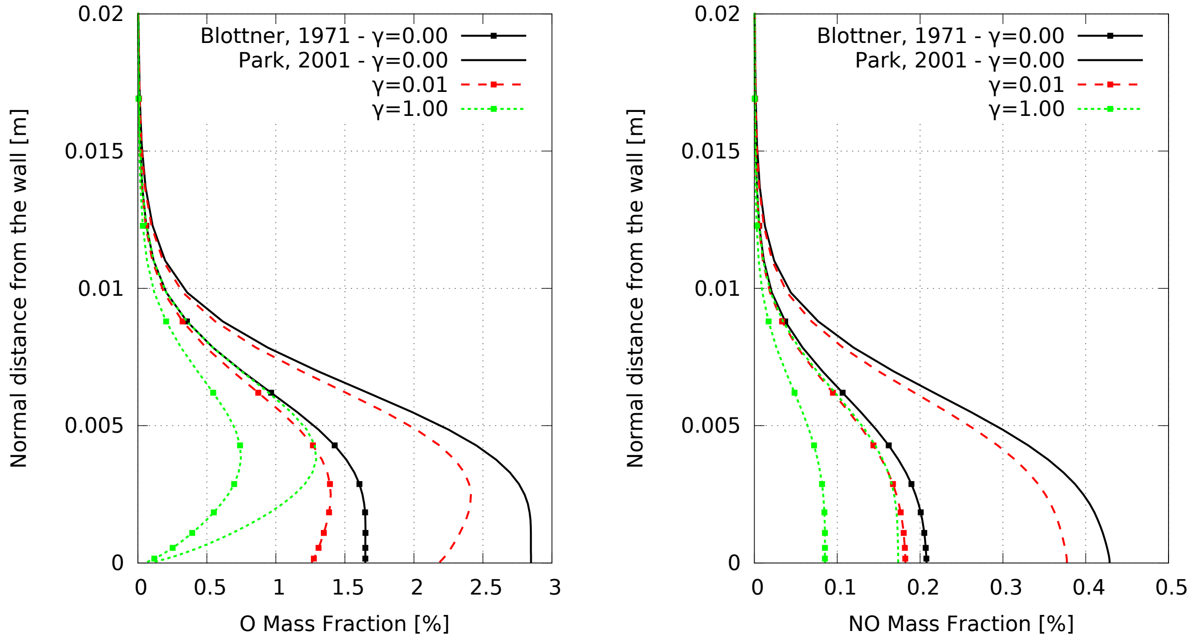

(a) O Mass Fraction

(b) NO Mass Fraction

Figure B.1: SPARK results for mass fraction of profiles normal to cone surface at $x = 0.5\,\mathrm{m}$.($\theta = 10^\circ$, SEB) using kinetics from Park, 2001 [35] vs. Blottner, 1971 [34].

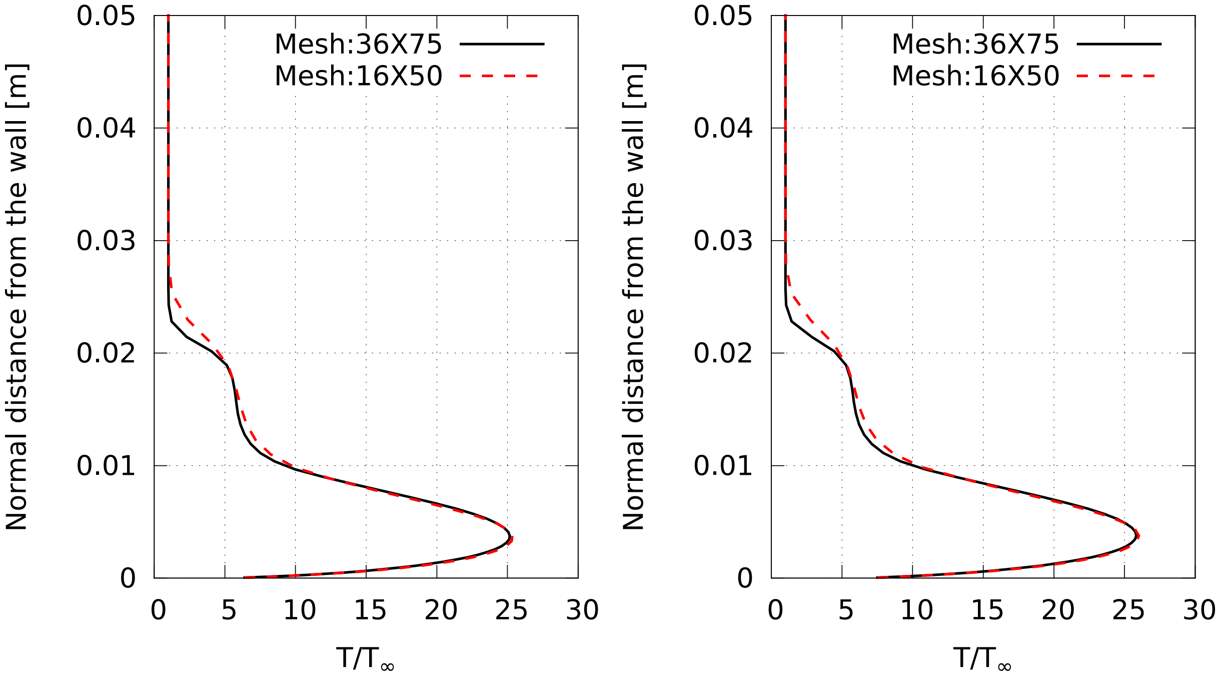

(a) Isothermal wall, $T_{\rm w}$=1200 K, Semi-Angle = 10^0.

(b) SEB, Semi-Angle = 10^0.

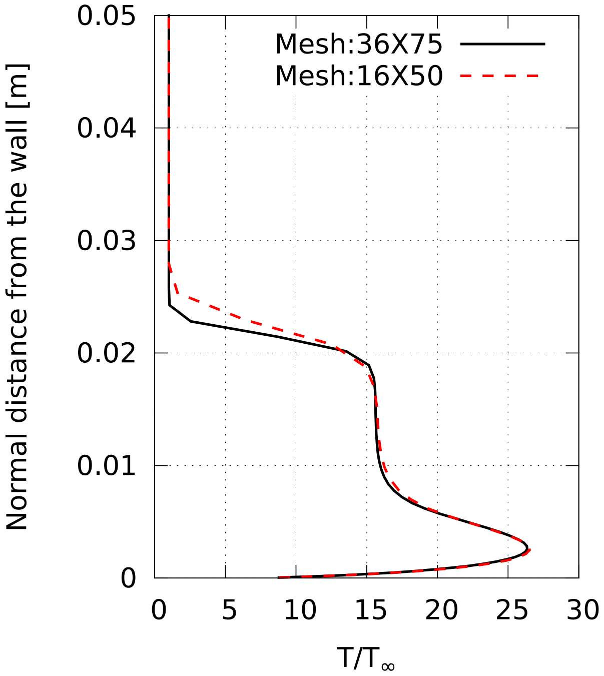

(c) SEB, Semi-Angle = 20^0.

Figure B.2: SPARK mesh convergence study for the 3 test cases of sharp cones reproduced by SPARK. The variable examined is the temperature profile normal to the cone surface at x=0.5[m].

B.2 Electre Probe

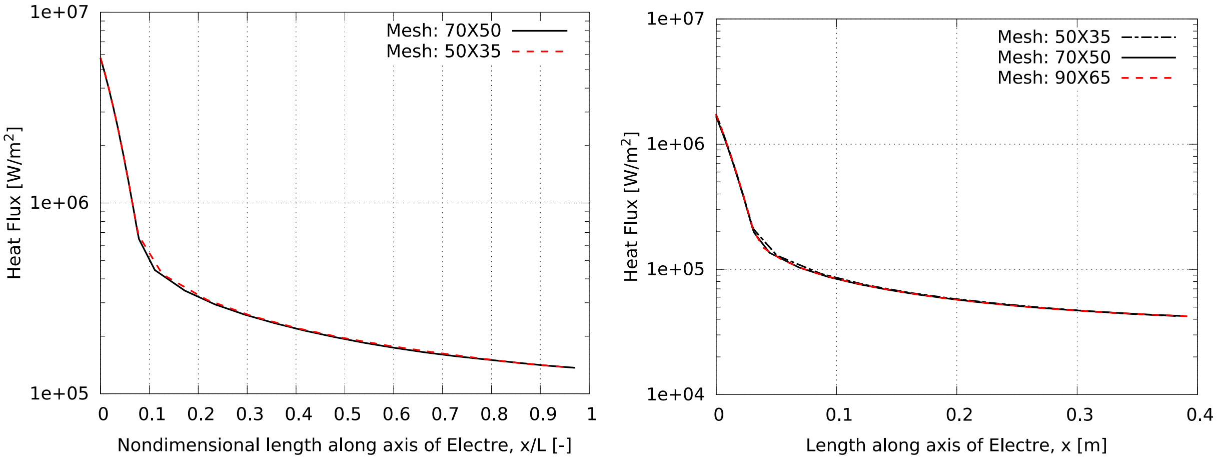

(a) Test case corresponding to Vivani et al., [38]

(b) Test case corresponding to Muylaert et al., [32]

Figure B.3: SPARK mesh convergence study for the scenarios concerning the Electre probe. The quantity examined is the heat flux into Electre.

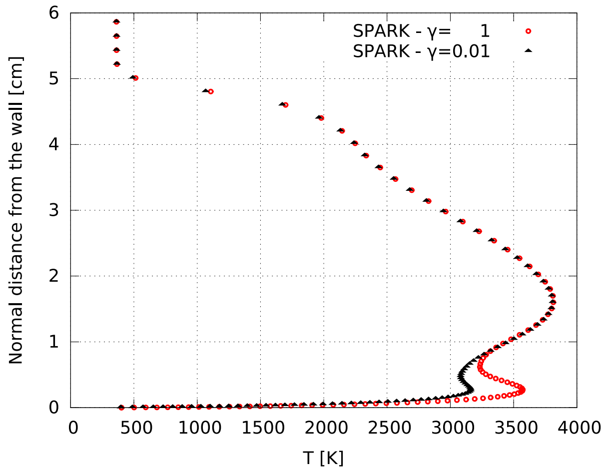

(a) Temperature profile normal to surface of Electre at x = 0.1 m

Figure B.4: Temperature along the normal to Electre's wall at x = 0.1 m for T_w = 343 K. Comparison of current results under SPARK for two catalytic recombination coefficients γ = 1 and γ = 0.01 to examine their effect on temperature. Upstream conditions correspond to Barbato et al.

B.3 Temperature varying SRE, $\gamma = \gamma(T)$

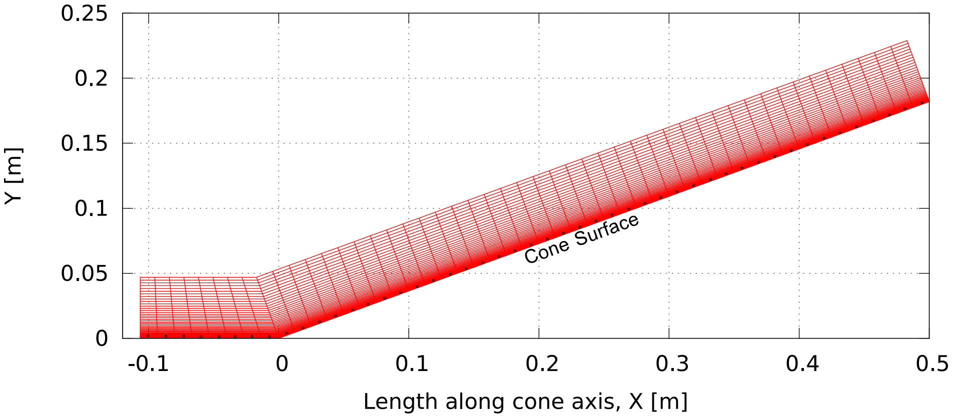

Figure B.5: Mesh used on the simulations for verification of the temperature dependent recombination efficiency models implemented on SPARK. Details: θ = 20°, 40X50 cells. The discrete black points represent the location of the profiles(temperature and mass fractions). The cone starts at x=0.

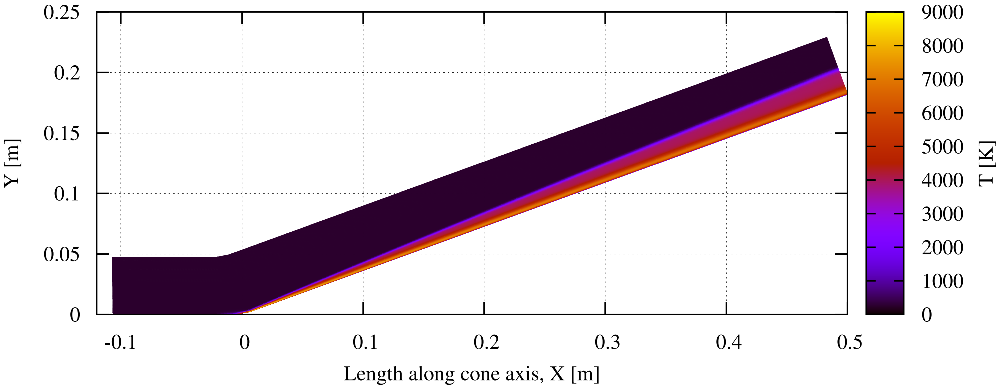

Figure B.6: 2-dimensional plot of temperature for SPARK simulation case: Sharp Cone, Semi-angle = 20°, SEB. Catalytic model not relevant as temperature was grossly insensitive to it.

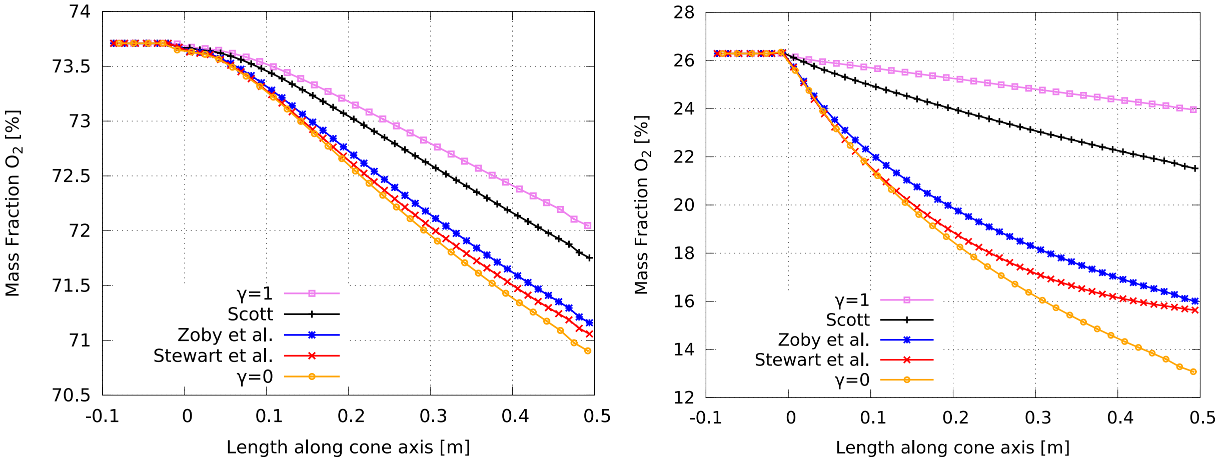

(a) N_2 mass fraction on the surface of the cone, $(c_{N_2})_w$ (b) O_2 mass fraction on the surface of the cone, $(c_{O_2})_w$

Figure B.7: Mass fraction of species N_2 and O_2 on the surface of the cone as a function of its axial length for several models applied on the same case: Sharp Cone, Semi-angle = 20°, SEB. Ranges of y-axis are not the same. $\gamma_N = \gamma_O = \gamma$.

B.4 FRSC - Finite Rate Surface Chemistry

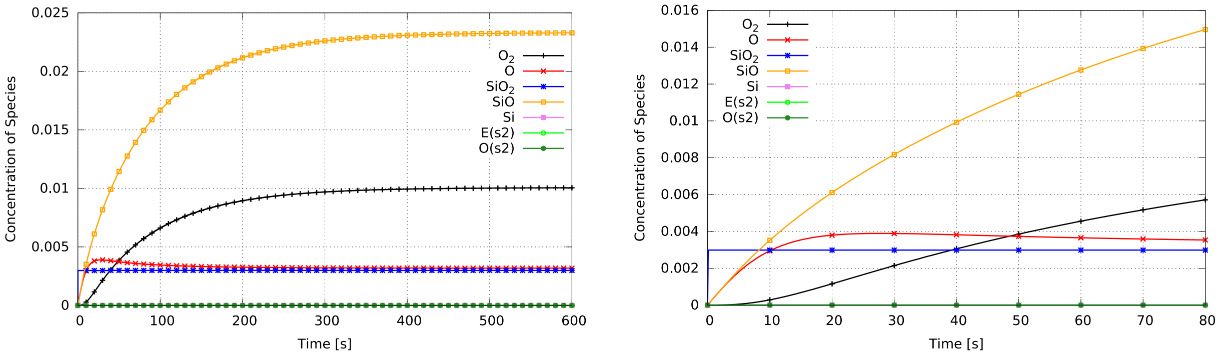

(a) First range of time.

(b) Second range of time.

Figure B.8: Transient evolution of the species concentrations (mol m^{-3} or mol m^{-2}) from an initial condition consisting of only bulk silica, argon and free sites. The temperature is 2500 K and the initial pressure is 10000 Pa. All surface reactions included. Silica sublimation case.